Graduate Theses and Dissertations

Graduate College

2011

The theoretical study of passive and active optical devices via planewave based transfer (scattering) matrix method and other approaches

Zhuo Ye
Iowa State University

The theoretical study of passive and active optical devices via planewave based transfer

(scattering) matrix method and other approaches

by

Zhuo Ye

A dissertation submitted to the graduate faculty

In partial fulfillment of the requirements for the degree of

DOCTOR OF PHILOSOPHY

Major: Condensed Matter Physics

Program of Study Committee:
Kai-Ming Ho, Major Professor
Kristen P. Constant
Jörg Schmalian
Joseph Shinar
Kerry Whisnant

Iowa State University

Ames, Iowa

2011

Table of Contents

Acknowledgement

It has been more than 6 years since I left my homeland, China, to pursue my PhD's degree in Department of Physics & Astronomy at Iowa State University. Along this very long journey I was lucky to have met mentors and friends who have provided knowledge, guidance, wisdom, and friendship. I would like to thank them, who without their help and support the completion of this thesis could never have been possible.

First and foremost, I need to thank my advisor and my committee. Dr. Kai-Ming Ho has been providing guidance and mentoring since I began my journey into the physics profession. I began my collegiate journey in electrical engineering. But I applied for PhD program of physics since I could not resist the beauty and fun of it. It was Dr. Ho who persuaded the recruitment committee to admit me. I owed him thanks even before I came to ISU. During my PhD study, he always gave me invaluable supports and enormous advices. I have learned a lot not only from his genius in physics but also his attitude of doing research. I also owe many thanks to my committee Dr. Kristen Constant, Dr. Jörg Schmalian, Dr. Joseph Shinar and Dr. Kerry Whisnant. I am so grateful to them for their sage advice throughout this process.

Many thanks should go to friends and buddies, Xinhua Hu, Ming Li, Yongxin Yao, Chun Xu, Ping Kuang, Guiping Zhang, and Junhua Zhang. They have also made this journey possible and enjoyable. I should also thank Jae-Huang Lee for his guidance in experiments and Wen-Cai Lu for discussions on QUAMBOs.

My sincere gratitude is extended to my family. The completion of this thesis could never have been possible without the spiritual supports of my grandparents, parents and husband. Their encouragements have made this long and lonely journey full of hope. I would like to especially thank my parents and parents-in-law for helping me take care of my baby daughter.

Abstract

In this thesis, we theoretically study the electromagnetic wave propagation in several passive and active optical components and devices including 2-D photonic crystals, straight and curved waveguides, organic light emitting diodes (OLEDs), and etc. Several optical designs are also presented like organic photovoltaic (OPV) cells and solar concentrators.

The first part of the thesis focuses on theoretical investigation. First, the plane-wave-based transfer (scattering) matrix method (TMM) is briefly described with a short review of photonic crystals and other numerical methods to study them (Chapter 1 and 2). Next TMM, the numerical method itself is investigated in details and developed in advance to deal with more complex optical systems. In chapter 3, TMM is extended in curvilinear coordinates to study curved nanoribbon waveguides. The problem of a curved structure is transformed into an equivalent one of a straight structure with spatially dependent tensors of dielectric constant and magnetic permeability. In chapter 4, a new set of localized basis orbitals are introduced to locally represent electromagnetic field in photonic crystals as alternative to planewave basis.

The second part of the thesis focuses on the design of optical devices. First, two examples of TMM applications are given. The first example is the design of metal grating structures as replacements of ITO to enhance the optical absorption in OPV cells (chapter 6). The second one is the design of the same structure as above to enhance the light extraction of OLEDs (chapter 7). Next, two design examples by ray tracing method are given, including applying a microlens array to enhance the light extraction of OLEDs (chapter 5) and an all-angle wide-wavelength design of solar concentrator (chapter 8).

In summary, this dissertation has extended TMM which makes it capable of treating complex optical systems. Several optical designs by TMM and ray tracing method are also given as a full complement of this work.

Chapter 1. Introduction

1.1 Photonic crystal and its properties

The concept of photonic crystals (PCs) was first introduced by Eli Yablonovitch[1] and Sajeev John[2] in 1987, under the inspiration of crystals. The periodic dielectric nanostructures of PCs affect photon motion in the similar way as the periodic potential in a crystal affects electron motion.

PCs have photonic band gaps just like crystals have band gaps. Photons of which the wavelengths are in the photonic band gap are prohibited to propagate in PCs. A diamond structure with three dimensional (3-D) band gaps was theoretically predicted by Kai-Ming Ho[3] and coworkers in 1990, and a 3-D PC in microwave regime was fabricated by Yablonovitch and coworkers in 1991. Photonic band gap is the most important property of PCs, and gives rise to many applications such as control of spontaneous emission[4], high-reflecting omni-directional mirrors[5], low-loss-waveguiding[6] and etc.

1.2 Numerical approaches

Several numerical methods have been applied to study the light propagation in PCs. Most of these methods are developed not only for PCs, but also for other microscopic optical devices. In the following we introduce some widely used numerical methods:

1.2.1 Plane wave expansion method (PWE)

PWE[3] is a frequency-domain method to solve the Maxwell's equations for a periodic

structure by formulating an eigenvalue problem out of the equation. It is popular as a method of solving for the band structure of PCs. It can be combined with transfer matrix method (TMM) to solve a wide range of problems like the transmittance, reflectance, absorption, mode profiles and emission for passive or active photonic devices. It can also be used for a non-periodic structure like a single waveguide through a supercell technique.

1.2.2   Finite difference time domain method (FDTD)

FDTD[7] is a popular computational electrodynamics modeling technique in time domain. The time-dependent Maxwell's equations are discretized using central-difference approximations to the space and time partial derivatives. The electric and magnetic fields are calculated everywhere in the computational domain as they evolve in time. FDTD is considered easy to understand and easy to implement in software. However, it often requires a big memory to solve a 3-D structure.

1.2.3   Localized function approach

Numerical methods using localized functions such as optical Wannier functions[8] and tight-binding approaches[9] are used to study PCs. These methods, both adopted from the electronic theory of solids, provide an alternative basis to plane waves to efficiently study the localized state of light in PCs. They are often more efficient than PWE in terms of computing speed, but the construction of the characteristic localized functions are not so easy to understand and to implement as plane waves.

1.2.4   Ray tracing method

Ray tracing is a method for calculating the optical path through a system with regions of

varying propagation velocity, absorption characteristics, and reflecting surfaces. In a ray tracing program, a big number of rays are "tracked" as they travel through the medium. Ray tracing method is valid as long as the light waves propagate through and around objects whose dimensions are much greater than the light's wavelength. It can not deal with interference and diffraction, so it cannot be used to study nanostructures where coherent optical phenomena dominate. However, it is powerful in designing imaging and lighting systems and is widely used in industry.

References:

1. E. Yablonovitch, "Inhibited spontaneous emission in solid-state physics and electronics", *Phys. Rev. Lett.* 58, 2059 (1987).

2. S. John, "Strong localization of photons in certain disordered dielectric superlattices", *Phys. Rev. Lett.* 58, 2486 (1987).

3. K. M. Ho, C. T. Chan, C. M. Soukoulis, "Existence of a photonic gap in periodic dielectric structures", *Phys. Rev. Lett.* 65, 3152 (1990).

4. P. Lodahl, A. F. van Driel, I. S. Nikolaev, A. Irman, K. Overgaag, D. Vanmaekelbergh, W. L. Vos, "Controlling the dynamics of spontaneous emission from quantum dots by photonic crystals", *Nature* 430, 654 (2004).

5. D. Lusk, F. Placido, "Omnidirectional mirror coating design for infrared applications", *Thin Solid Films* 492, 226 (2005).

6. J. C. Knight, "Photonic crystal fibres", *Nature* 424, 847 (2003).

7. A. Taflove, "Application of the finite-difference time-domain method to sinusoidal steady state electromagnetic penetration problems", *IEEE Trans. Electroman. Compat.* 22, 191 (1980).

8. D. M. Whittaker, M. P. Croucher, "Maximally localized Wannier functions for

photonic lattices", *Phys. Rev. B* 67, 085204 (2003).

9. M. Bayindir, B. Temelkuran, E. Ozbay, "Tight-binding description of the coupled defect modes in three-dimensional photonic crystals", *Phys. Rev. Lett.* 84, 2140 (2000).

Chapter 2. The plane-wave-based transfer (scattering) matrix method − A short review

We will apply the plane-wave-based transfer matrix method (TMM) in design and simulation in Chapter 4 and 5. In Chapter 6 TMM will be extended to curvilinear coordinates to deal with curved waveguide. This chapter is like a literature review part, in which we describe briefly how to derive the transfer and scattering matrix from Maxwell's equations. Most of the content has been published by Dr. Zhi-Yuan Li as a series of journal papers[1-6]. An efficient parallel simulation software based on TMM has been developed for 3-D photonic crystal by Dr. Ming Li, under cooperation with Canon Inc. The TMM software package has already been used in actual device design at Canon and commercialized by Iowa State University Research Foundation.

2.1   Maxwell's equations

The most general form of Maxwell's equations

$$
\begin{aligned}
\nabla \times \vec{E} &= -\frac{1}{c}\frac{\partial \vec{B}}{\partial t}, \\
\nabla \times \vec{H} &= \frac{1}{c}\frac{\partial \vec{D}}{\partial t} + \frac{4\pi}{c}\vec{J}, \\
\nabla \bullet \vec{D} &= 4\pi\rho, \\
\nabla \bullet \vec{B} &= 0,
\end{aligned}
\tag{2.1}
$$

can be written in

$$\nabla \times \vec{E}(\vec{r}) = ik_0\vec{H}(\vec{r}),$$
$$\nabla \times \vec{H}(\vec{r}) = -ik_0\varepsilon(\vec{r})\vec{E}(\vec{r}),$$
$$\nabla \bullet \left[\varepsilon(\vec{r})\vec{E}(\vec{r}) \right] = 0, \tag{2.2}$$
$$\nabla \bullet \vec{H}(\vec{r}) = 0,$$

where $k_0 = \omega/c$, and we have assumed a time harmonic dependence, $\vec{E}(\vec{r},t) = \vec{E}(\vec{r})e^{-i\omega t}$, $\vec{H}(\vec{r},t) = \vec{H}(\vec{r})e^{-i\omega t}$ and no free charges or currents. The last two equations in Eqs. (2.2) are automatically satisfied given the first two equations. So the first two equations are only to be considered. They are vector differential equations, and there are altogether 6 equations with respect to the (x, y, z) component of $\vec{E}(\vec{r})$ and $\vec{H}(\vec{r})$. If optical waves are assumed to be propagating along z axis, and E_z, H_z can be expressed in terms of E_x, E_y, H_x, H_y, Maxwell's equations can be written in terms of differential equations relating to the transverse components of fields:

$$\frac{\partial}{\partial z}E_x = \frac{1}{-ik_0}\frac{\partial}{\partial x}\left[\frac{1}{\varepsilon(\vec{r})}\left(\frac{\partial H_y}{\partial x} - \frac{\partial H_x}{\partial y}\right)\right] + ik_0 H_y,$$

$$\frac{\partial}{\partial z}E_y = \frac{1}{-ik_0}\frac{\partial}{\partial y}\left[\frac{1}{\varepsilon(\vec{r})}\left(\frac{\partial H_y}{\partial x} - \frac{\partial H_x}{\partial y}\right)\right] - ik_0 H_x,$$

$$\frac{\partial}{\partial z}H_x = \frac{1}{ik_0}\frac{\partial}{\partial x}\left(\frac{\partial E_y}{\partial x} - \frac{\partial E_x}{\partial y}\right) - ik_0\varepsilon(\vec{r})E_y, \tag{2.3}$$

$$\frac{\partial}{\partial z}H_y = \frac{1}{ik_0}\frac{\partial}{\partial y}\left(\frac{\partial E_y}{\partial x} - \frac{\partial E_x}{\partial y}\right) + ik_0\varepsilon(\vec{r})E_x.$$

2.2 Fourier space expression

We consider a 3-D device shown in Fig. 2-1. Suppose electromagnetic (EM) wave is

propagating along z axis towards the device, and the device is periodic in (x, y) plane. It can be periodic along both x and y, or, periodic along one direction and uniform along the other direction, or uniform along both directions. We slice the 3-D structure in such a way that in each layer, it is uniform along z. In other words, the refractive index is a function dependent only on the transverse coordinates (x, y) in each layer (see Fig. 2-1).
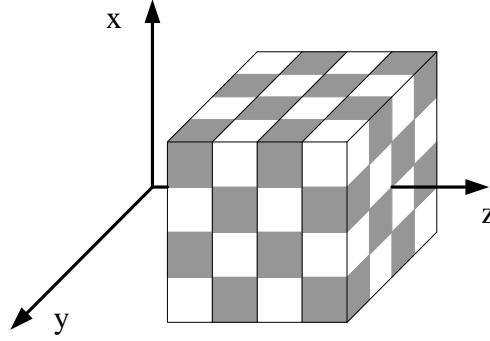
FIGURE 2-1. Schematic of a 3-D structure which is periodic along x and y directions.

From Bloch theorem[7], the EM fields at an arbitrary point $\vec{r}$ can be written into the superposition of Bragg waves (or plane waves) when a plane wave is incident from the left side with a wave vector $k_0 = (k_{0x}, k_{0y}, k_{0z})$:

$$
\begin{aligned}
E_x(\vec{r}) &= \sum_{ij} E_{ij,x}(z)e^{i(k_{ij,x}x + k_{ij,y}y)}, \\
E_y(\vec{r}) &= \sum_{ij} E_{ij,y}(z)e^{i(k_{ij,x}x + k_{ij,y}y)}, \\
H_x(\vec{r}) &= \sum_{ij} H_{ij,x}(z)e^{i(k_{ij,x}x + k_{ij,y}y)}, \\
H_y(\vec{r}) &= \sum_{ij} H_{ij,y}(z)e^{i(k_{ij,x}x + k_{ij,y}y)},
\end{aligned}
\tag{2.4}
$$

where the Bragg wave vector $k_{ij} = (k_{ij,x}, k_{ij,y}) = (k_{0x}, k_{0y}) + i\vec{b}_1 + j\vec{b}_2$, $\vec{b}_1$ and $\vec{b}_2$ are the reciprocal lattice constant, $E_{ij,x}, E_{ij,y}, H_{ij,x}, H_{ij,y}$ are unknown expansion coefficients of the transverse electric and magnetic fields. At the same time, since $\varepsilon(\vec{r})$ is also periodic in (x, y) plane, it can be also expanded on plane wave basis:

$$\frac{1}{\varepsilon(\vec{r})} = \sum_{ij} \varepsilon_{ij}^{-1}(z) e^{i(k_{ij,x}x + k_{ij,y}y)},$$

$$\varepsilon(\vec{r}) = \sum_{ij} \varepsilon_{ij}(z) e^{i(k_{ij,x}x + k_{ij,y}y)}, \tag{2.5}$$

where $\varepsilon_{ij}^{-1}(z)$ and $\varepsilon_{ij}(z)$ is the Fourier expansion coefficients of $1/\varepsilon(\vec{r})$ and $\varepsilon(\vec{r})$ respectively in a specific layer. Substituting Eqs. (2.4) and (2.5) into Eq. (2.3), we can transform the partial differential equations to Eq. (2.6):

$$\frac{\partial E_{ij,x}}{\partial z} = -\frac{ik_{ij,x}}{k_0} \sum_{mn} \varepsilon_{i-m,j-n}^{-1} (H_{mn,y}k_{mn,x} - H_{mn,x}k_{mn,y}) + ik_0 H_{ij,y},$$

$$\frac{\partial E_{ij,y}}{\partial z} = -\frac{ik_{ij,y}}{k_0} \sum_{mn} \varepsilon_{i-m,j-n}^{-1} (H_{mn,y}k_{mn,x} - H_{mn,x}k_{mn,y}) - ik_0 H_{ij,x},$$

$$\frac{\partial H_{ij,x}}{\partial z} = \frac{ik_{ij,x}}{k_0} \sum_{mn} \delta_{im,jn} (E_{mn,y}k_{mn,x} - E_{mn,x}k_{mn,y}) - ik_0 \varepsilon_{i-m,j-n} E_{ij,y}, \tag{2.6}$$

$$\frac{\partial H_{ij,y}}{\partial z} = \frac{ik_{ij,x}}{k_0} \sum_{mn} \delta_{im,jn} (E_{mn,y}k_{mn,x} - E_{mn,x}k_{mn,y}) + ik_0 \varepsilon_{i-m,j-n} E_{ij,x}.$$

We define two column vectors $E = (..., E_{ij,x}, E_{ij,y}, ...)^T$, $H = (..., H_{ij,x}, H_{ij,y}, ...)^T$ to represent the unknown coefficients of $E_{ij,x}, E_{ij,y}, H_{ij,x}, H_{ij,y}$. Then Eq. (2.6) can be written in a concise form Eq. (2.7):

$$\frac{\partial}{\partial z}E = T_1 H, \quad \frac{\partial}{\partial z}H = T_2 E,$$

$$T_1^{ij,mn} = \frac{i}{k_0}\begin{pmatrix} k_{ij,x}\varepsilon_{i-m,j-n}^{-1}k_{mn,y} & -k_{ij,x}\varepsilon_{i-m,j-n}^{-1}k_{mn,x} + k_0^2\delta_{im,jn} \\ k_{ij,y}\varepsilon_{i-m,j-n}^{-1}k_{mn,y} - k_0^2\delta_{im,jn} & k_{ij,y}\varepsilon_{i-m,j-n}^{-1}k_{mn,x} \end{pmatrix}, \tag{2.7}$$

$$T_2^{ij,mn} = \frac{i}{k_0}\begin{pmatrix} -k_{ij,x}\delta_{im,jn}k_{mn,y} & k_{ij,x}\delta_{im,jn}k_{mn,x} - k_0^2\varepsilon_{i-m,j-n} \\ -k_{ij,y}\delta_{im,jn}k_{mn,y} + k_0^2\varepsilon_{i-m,j-n} & k_{ij,y}\delta_{im,jn}k_{mn,x} \end{pmatrix}.$$

From Eq. (2.7) we finally obtain an eigenproblem for the electric field in a specific layer,

$$\frac{\partial^2}{\partial z^2}E = (T_1 T_2)E = PE = -QE. \tag{2.8}$$

Suppose we truncate the number of plane waves to be N_0 in the expansion, then T_1, T_2, P, Q are all $(2N_0)\times(2N_0)$ matrices. We can find the eigenvalue and eigenvector of Q. With the eigenvalue β^2 calculated [Eq. (2.9)], Eq. (2.8) can be expressed by Eq. (2.10) with each element of the unknown coefficients in vector E a function of z.

$$QE = \beta^2 E. \tag{2.9}$$

$$\frac{\partial^2}{\partial z^2}E + \beta^2 E = 0. \tag{2.10}$$

Solutions of Eq. (2.9) will give $2N_0$ eigenvalues $\beta_i^2, i = 1, 2, ..., 2N_0$. A $(2N_0)\times(2N_0)$ matrix S_a, whose jth column is the eigenvector corresponding to the eigenvalue β_i^2, can also be obtained simultaneously. The eigenmode corresponding to β_i^2 is

$$E_i(z) = E_i^+(z) + E_i^-(z) = E_i^+ e^{i\beta_i z} + E_i^- e^{-i\beta_i z}, \tag{2.11}$$

where E_i^+, E_i^- are both variables to be determined. We further define column vector $\beta = (..., \beta_i, ...)^T$, $E^+ = (..., E_i^+(z), ...)^T$, $E^- = (..., E_i^-(z), ...)^T$. The electric field column vector E is now expressed in the superposition of all eigenmodes,

$$E = S_a(E^+ + E^-) = (S_a, S_a)\begin{pmatrix} E^+ \\ E^- \end{pmatrix}. \tag{2.12}$$

The corresponding magnetic field column vectors are obtained from Eq. (2.7),

$$\begin{aligned} H &= T_1^{-1} \frac{\partial}{\partial z} E = T_1^{-1} S_a \frac{\partial}{\partial z} (E^+ + E^-) \\ &= iT_1^{-1} S_a \beta (E^+ - E^-) = (T_a, -T_a)\begin{pmatrix} E^+ \\ E^- \end{pmatrix}, \\ &\text{where } T_a = iT_1^{-1} S_a \beta. \end{aligned} \tag{2.13}$$

We combine Eqs. (2.12) and (2.13), and write down the electric and magnetic fields at an arbitrary point into a concise form:

$$\begin{pmatrix} E(z) \\ H(z) \end{pmatrix} = \begin{pmatrix} S_a & S_a \\ T_a & -T_a \end{pmatrix} \begin{pmatrix} E^+ \\ E^- \end{pmatrix}. \tag{2.14}$$

Inside a slice, the macroscopic medium is homogeneous along z axis, and E^+, E^- are sets of eigenmodes of this slice propagating along $+z$ and $-z$ separately. So we have

$$\begin{pmatrix} E^+(z+h) \\ E^-(z+h) \end{pmatrix} = \begin{pmatrix} e^{i\beta h} & 0 \\ 0 & e^{-i\beta h} \end{pmatrix} \begin{pmatrix} E^+(z) \\ E^-(z) \end{pmatrix}. \tag{2.15}$$

2.3   Transfer matrix to connect slices

In previous section, we have solved the eigenmodes of a single slice which is uniform along z axis, and expressed the electric and magnetic fields in terms of these eigenmodes. Next we will connect a series of 2-D slices into a whole 3-D structure.
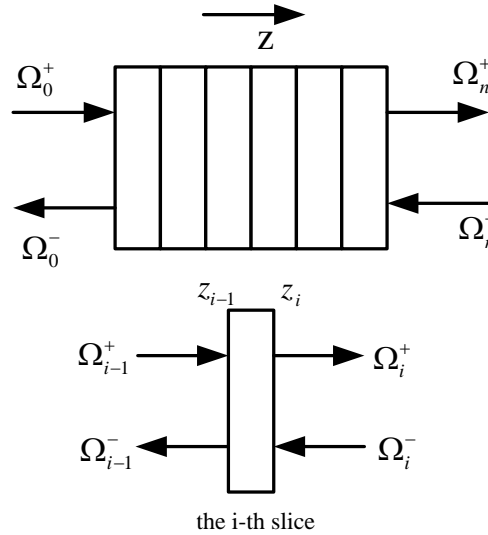
FIGURE 2-2. Schematic of TMM for a single slice and a series of slices.

The scheme of TMM is illustrated in Fig. 2-2. For each 2-D slice, it is assumed that there are two infinitely thin air films (or any homogeneous medium) around it. These air films are used as a "glue" to connect all slices. The artificial air films will have no impact on the problem since it is extremely thin. The purpose of them is to allow the boundary condition (tangential EM field is continuous across an interface) be applied in a convenient way.

Fist consider the left surface of a single slice i $(i = 1, 2, ..., n)$. To the left of surface $(z \leq z_{i-1})$ is the air film, and the electric and magnetic fields can be expressed in a way similar to Eq. (2.14),

$$\begin{pmatrix} E(z) \\ H(z) \end{pmatrix} = \begin{pmatrix} S_0 & S_0 \\ T_0 & -T_0 \end{pmatrix} \begin{pmatrix} \Omega_{i-1}^+ \\ \Omega_{i-1}^- \end{pmatrix}, \tag{2.16}$$

where S_0, T_0 are corresponding S_a, T_a in air, and $\Omega_{i-1}^+, \Omega_{i-1}^-$ are the coefficients of eigenmodes in air (i.e. plane waves). To the right of surface $(z \geq z_{i-1})$ is the i th slice, the electric and magnetic fields can be expressed as,

$$\begin{pmatrix} E(z) \\ H(z) \end{pmatrix} = \begin{pmatrix} S_i & S_i \\ T_i & -T_i \end{pmatrix} \begin{pmatrix} E_i^+ \\ E_i^- \end{pmatrix}, \tag{2.17}$$

where S_i, T_i are corresponding S_a, T_a in slice i. From the continuity of EM fields at the interface $z = z_{i-1}$, we have

$$\begin{pmatrix} S_0 & S_0 \\ T_0 & -T_0 \end{pmatrix} \begin{pmatrix} \Omega_{i-1}^+ \\ \Omega_{i-1}^- \end{pmatrix} = \begin{pmatrix} S_i & S_i \\ T_i & -T_i \end{pmatrix} \begin{pmatrix} E_i^+(z_{i-1}) \\ E_i^-(z_{i-1}) \end{pmatrix}. \tag{2.18}$$

Similarly, at the right interface $z = z_i$, we have

$$\begin{pmatrix} S_0 & S_0 \\ T_0 & -T_0 \end{pmatrix} \begin{pmatrix} \Omega_i^+ \\ \Omega_i^- \end{pmatrix} = \begin{pmatrix} S_i & S_i \\ T_i & -T_i \end{pmatrix} \begin{pmatrix} E_i^+(z_i) \\ E_i^-(z_i) \end{pmatrix}. \tag{2.19}$$

Inside the slice, from Eq. (2,15) we have,

$$\begin{pmatrix} E_i^+(z_i) \\ E_i^-(z_i) \end{pmatrix} = \begin{pmatrix} e^{i\beta h} & 0 \\ 0 & e^{-i\beta h} \end{pmatrix} \begin{pmatrix} E_i^+(z_{i-1}) \\ E_i^-(z_{i-1}) \end{pmatrix}, \text{ with } z_i = z_{i-1} + h. \tag{2.20}$$

Combining Eqs. (2.18)-(2.20), we get the transfer matrix T_i for slice i,

$$\begin{pmatrix} \Omega_i^+ \\ \Omega_i^- \end{pmatrix} = T_i \begin{pmatrix} \Omega_{i-1}^+ \\ \Omega_{i-1}^- \end{pmatrix},$$

$$T_i = \begin{pmatrix} a_{11} & a_{12} \\ a_{21} & a_{22} \end{pmatrix}^{-1} \begin{pmatrix} e^{i\beta h} & 0 \\ 0 & e^{-i\beta h} \end{pmatrix} \begin{pmatrix} a_{11} & a_{12} \\ a_{21} & a_{22} \end{pmatrix},$$

$$a_{11} = \frac{1}{2}\left(S_i^{-1}S_0 + T_i^{-1}T_0\right), a_{22} = a_{11}, \tag{2.21}$$

$$a_{12} = \frac{1}{2}\left(S_i^{-1}S_0 - T_i^{-1}T_0\right), a_{21} = a_{12}.$$

After we connect the right surface to the left surface for slice i by T_i, we can get the overall transfer matrix T for the whole structure by connecting all n slices together: $T = T_n T_{n-1} \cdots T_1$. However, the transfer matrix T proved to be numerically unstable when the structure is thick, due to the fact that the evanescent wave components in the planewave expansion will increase exponentially if entire T_i matrices are multiplied.

One solution to the numerical unstability of transfer matrix method is to adopt the scattering matrix S, the components of which can be directly calculated from T matrix. The overall S matrix can be computed by connecting S_i for each slice through an iteration algorithm. The expression of S matrix is given by,

$$\begin{pmatrix} \Omega_i^+ \\ \Omega_{i-1}^- \end{pmatrix} = S_i \begin{pmatrix} \Omega_{i-1}^+ \\ \Omega_i^- \end{pmatrix},$$

$$T_i = \begin{pmatrix} p_1 t_1 + p_2 t_2 & p_1 t_2 + p_2 t_1 \\ p_1 t_2 + p_2 t_1 & p_1 t_1 + p_2 t_2 \end{pmatrix},$$

$$p_1 = \left[a_{11} - e^{i\beta h} a_{12} a_{11}^{-1} e^{i\beta h} a_{12} \right]^{-1},$$

$$p_2 = a_{11}^{-1} e^{i\beta h} a_{12},$$

$$t_1 = a_{11}^{-1} e^{i\beta h} a_{12} \left[a_{11} - e^{i\beta h} a_{12} a_{11}^{-1} e^{i\beta h} a_{12} \right]^{-1},$$

$$t_2 = -a_{12}.$$

(2.22)

Finally a numerical stable scattering matrix S can be obtained for the whole 3-D structure. S matrix is only decided by the dielectric distribution of the 3-D structure (assume it is not magnetic). For different applications, such as computation of spectrum, photonic band structure, or mode profile, desired initial condition and boundary condition are applied to the S matrix.

2.4   An example: Spectrum calculation

From Eq. (2.22), we have such a relation Eq. (2.23) which connects the field column vector at the left and right side of the 3-D structure shown in Fig. 2-2. When an EM wave expressed in Ω_0^+ is incident from the left, Ω_n^- is set to be zero since there are no backward waves to the right side of the 3-D structure. The transmitted field E^t and reflected field E^r can be calculated as follows,

$$\begin{pmatrix} \Omega_n^+ \\ \Omega_0^- \end{pmatrix} = S \begin{pmatrix} \Omega_0^+ \\ \Omega_n^- \end{pmatrix} = \begin{pmatrix} S_{11} & S_{12} \\ S_{21} & S_{22} \end{pmatrix} \begin{pmatrix} \Omega_0^+ \\ \Omega_n^- \end{pmatrix},$$

$$E^t = \Omega_n^+ = S_{11} \Omega_0^+, \quad E^r = \Omega_0^- = S_{21} \Omega_0^+, \quad with \ \Omega_n^- = 0.$$

(2.23)

After we get the transmitted field E^t and reflected field E^r, the transmittance $\mathbf{T}$ or reflectance rate $\mathbf{R}$, defined as the ratio of energy flux of transmitted wave or reflected wave to the energy flux of incident wave respectively, can be calculated in Eq. (2.24), with the summation of i, j for propagating modes $k_{ij,x}^2 + k_{ij,y}^2 \leq k_0^2$. The absorptance $\mathbf{A}$, defined as the ratio of the energy absorbed by the whole 3-D structure to the incident energy, can be calculated from $\mathbf{T}$ and $\mathbf{R}$.

$$\mathbf{T} = \sum_{ij} \frac{\left|E_{ij}^t\right|^2 \left|\beta_{ij}\right|}{\left|E_0\right|^2 \left|k_{0z}\right|},$$

$$\mathbf{R} = \sum_{ij} \frac{\left|E_{ij}^r\right|^2 \left|\beta_{ij}\right|}{\left|E_0\right|^2 \left|k_{0z}\right|}, \qquad (2.24)$$

$$\mathbf{A} = 1 - \mathbf{T} - \mathbf{R}.$$

2.5   Summary

In this chapter of introduction of TMM, we reviewed the core knowledge of this numerical tool. We gave a numerical example for spectrum calculation of transmittance, reflectance, and absorptance. Beyond that, TMM has a lot of applications like computation of photonic band structure and field mode profiles. It can deal with active devices as well as passive ones. It can be extended to curvilinear coordinates to deal with curved structures. Some of these topics will be discussed in this thesis later on. Although the core algorithms have been well developed for TMM, some parts of it are still under development, and we are looking forwards to new strategies and applications of it.

References:

1. Z. Li and L. Lin, "Photonic band structures solved by a plane-wave-based transfer matrix method", *Phys. Rev. E* 67, 046607 (2003).

2. L. Lin, Z. Li and K. Ho, "Lattice symmetry applied in transfer-matrix methods for photonic crystals", *J. Appl. Phys.* 94, 811 (2003).

3. Z. Y. Li and K. M. Ho, "Application of structural symmetries in the plane-wave-based transfer-matrix method for three-dimensional photonic crystal waveguides", *Phys. Rev. B* 68, 245117 (2003).

4. Z. Y. Li and K. M. Ho, "Light propagation in semi-infinite photonic crystals and related waveguide structures", *Phys. Rev. B* 68, 155101 (2003).

5. Z. Y. Li and K. M. Ho, "Analytic modal solution to light propagation through layer-by-layer metallic photonic crystals", *Phys. Rev. B* 67, 165104 (2003).

6. Z. Y. Li and K. M. Ho, "Bloch mode reflection and lasing threshold in semiconductor nanowire laser arrays", *Phys. Rev. B* 71, 045315 (2005).

7. J. D. Joannopoulos, *Photonic crystal: Molding the flow of light*, Princeton University Press (1995).

Chapter 3. TMM extension to curvilinear coordinate system
to study guided modes in curved nanoribbon waveguides

The planewave based transfer (scattering) matrix method is developed in curvilinear coordinates to study the guided modes in curved nanoribbon waveguides. The problem of a curved structure is transformed into an equivalent one of a straight structure with spatially dependent tensors of dielectric constant and magnetic permeability. We investigate the coupling between the eigenmodes of the straight part and those of the curved part when the waveguide is bent. We show that curved sections can result in strong oscillations in the transmission spectrum similar to the recent experimental results of Lawet al. [*Science* 305, 1269 (2004)].

3.1   Introduction

Semiconductor nanowires and nanoribbons are emerging as important building blocks for nanoscale opto-electronics. Much attention has been drawn towards their optoelectronic applications such as waveguides[1], lasers[2], optical switches and sensors[3]. Among those applications nano waveguides are especially important as links between optoelectronic elements.

Nanoscale ribbon-shaped crystals of binary oxides exhibit extreme mechanical flexibility[1] and can be synthesized into various shapes of nanoribbon waveguides used in a nanoscale optical circuit. The simplest shape of straight waveguide has been widely studied either analytically or numerically. However, it is much more complicated to study a waveguide and its eigenmode properties when it is bended into various shapes. The guided modes in a bended waveguide present different propagation properties from a straight one.

An example is in a recent work by M.Law et al.[1]. They found strong regular oscillations in the output spectrum when light is traveling in a curved nanoribbon waveguide. The largest amplitude of oscillations is about 50% of the maximum output intensity. The period of the oscillations is about 20 nm. These strong oscillations can not be explained by traditional coupling theory. In this chapter we will present a model in curvilinear coordinates to simulate the curved nanoribbon waveguide.

3.2   Transform of TMM into curvilinear coordinates

In previous chapter, the planewave based transfer matrix method (TMM)[4,5] is mainly used in Euclidian coordinate system (x, y, z). For TMM, any applicable structures are all straight along the propagation direction (z axis). Although non-orthogonal lattice is allowed in the xy plane, it is not possible to deal with any structure that has any curvature along z axis. To study the properties of curved waveguides, we need to develop the TMM algorithm in curvilinear coordinate system (x', y', s) following a previous work on curvilinear coordinate system[6].

The relation between the Euclidian coordinates (x, y, z) and the curvilinear coordinates (x', y', s) is illustrated in Fig. 3-1. For Euclidian coordinates, each of $\hat{x}, \hat{y}, \hat{z}$ is perpendicular to the other two. The light is propagating straightly along z axis. For curvilinear coordinates (x', y', s), each of $\hat{x}', \hat{y}', \hat{s}$ is also perpendicular to the other two. s is the propagation direction and $\hat{x}'$ is always pointing to the center of the curvature of radius R. The relation between the Euclidian coordinates and curvilinear coordinates can be expressed by Eq. (3.1).
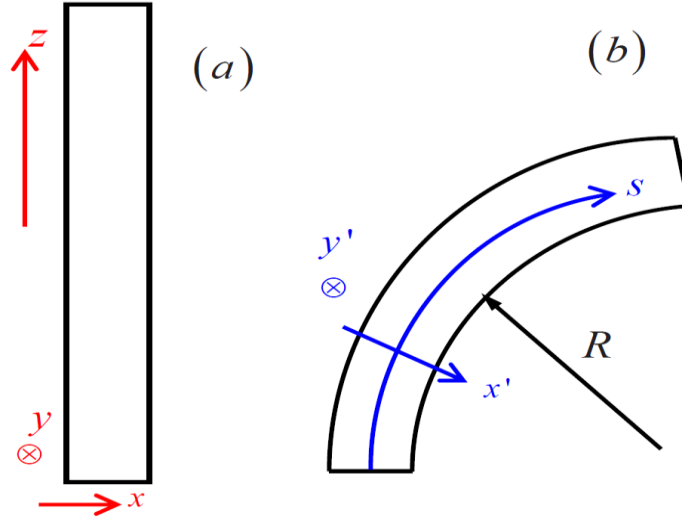
FIGURE 3-1. Coordinate system (a) Euclidian (b) curvilinear

$$x = x'\cos\frac{s}{R} + R\left(1 - \cos\frac{s}{R}\right),$$

$$y = y',$$

$$z = -x'\sin\frac{s}{R} + R\sin\frac{s}{R}.$$

(3.1)

Let (x^1, x^2, x^3) be the coordinates of Euclidian system and (q^1, q^2, q^3) be the coordinates of curvilinear system. The curvilinear coordinate system can be characterized by its covariant basis vector $\vec{a}_i$ and metric tensor $\tilde{g}_{ij}$ which are defined by

$$\vec{a}_i = \left(\frac{\partial x^1}{\partial q^i}, \frac{\partial x^2}{\partial q^i}, \frac{\partial x^3}{\partial q^i}\right),$$

(3.2)

and

$$\tilde{g}_{ij} = \sum_{k=1,2,3} \frac{\partial x^k}{\partial q^i} \frac{\partial x^k}{\partial q^i}$$

(3.3)

From Eq. (3.1), $\vec{a}_i$ and $\tilde{g}_{ij}$ can be calculated for the curvilinear coordinate system shown in Fig. 3-1(b) as

$$
\begin{aligned}
\vec{a}_{x'} &= \left(\cos\frac{s}{R}, 0, -\sin\frac{s}{R} \right), \\
\vec{a}_{y'} &= (0,1,0), \\
\vec{a}_s &= \left(-\frac{x'}{R}\sin\frac{s}{R} + \sin\frac{s}{R}, 0, -\frac{x'}{R}\cos\frac{s}{R} + \cos\frac{s}{R} \right).
\end{aligned}
\tag{3.4}
$$

and

$$
\tilde{g}_{ij} = \begin{pmatrix} 1 & 0 & 0 \\ 0 & 1 & 0 \\ 0 & 0 & \left(1-\dfrac{x'}{R}\right)^2 \end{pmatrix}.
\tag{3.5}
$$

A well known form of Maxwell's equations in general curvilinear coordinates can be written in the absence of free electric currents as[6]

$$
\begin{aligned}
\varepsilon(q^1, q^2, q^3)\frac{\partial \dfrac{E^i}{\sqrt{g_{ii}}}}{\partial ct} &= \frac{1}{\sqrt{g}} e^{ijk} \frac{\partial \dfrac{H_k}{\sqrt{g^{kk}}}}{\partial q^j}, \\
-\mu(q^1, q^2, q^3)\frac{\partial \dfrac{H^i}{\sqrt{g_{ii}}}}{\partial ct} &= \frac{1}{\sqrt{g}} e^{ijk} \frac{\partial \dfrac{E_k}{\sqrt{g^{kk}}}}{\partial q^j}.
\end{aligned}
\tag{3.6}
$$

Substituting Eqs. (3.4) and (3.5) into Eq. (3.6), we can get Maxwell's equations in terms of differential equations relating to the transverse components of electromagnetic field in our curvilinear coordinates:

$$\frac{\partial}{\partial s}E_{x'} = \frac{1}{-ik_0}\frac{\partial}{\partial x'}\left[\frac{1}{\varepsilon_3}\left(\frac{\partial H_{y'}}{\partial x'} - \frac{\partial H_{x'}}{\partial y'}\right)\right] + ik_0\mu_2 H_{y'},$$

$$\frac{\partial}{\partial s}E_{y'} = \frac{1}{-ik_0}\frac{\partial}{\partial y'}\left[\frac{1}{\varepsilon_3}\left(\frac{\partial H_{y'}}{\partial x'} - \frac{\partial H_{x'}}{\partial y'}\right)\right] - ik_0\mu_1 H_{x'},$$

$$\frac{\partial}{\partial s}H_{x'} = \frac{1}{ik_0}\frac{\partial}{\partial x'}\left[\frac{1}{\mu_3}\left(\frac{\partial E_{y'}}{\partial x'} - \frac{\partial E_{x'}}{\partial y'}\right)\right] - ik_0\varepsilon_2 E_{y'},$$

$$\frac{\partial}{\partial s}H_{y'} = \frac{1}{ik_0}\frac{\partial}{\partial y'}\left[\frac{1}{\mu_3}\left(\frac{\partial E_{y'}}{\partial x'} - \frac{\partial E_{x'}}{\partial y'}\right)\right] + ik_0\varepsilon_1 E_{x'},$$

(3.7)

where

$$\varepsilon_1 = \varepsilon_2 = \varepsilon\alpha,$$
$$\mu_1 = \mu_2 = \mu\alpha,$$
$$\varepsilon_3 = \varepsilon/\alpha,$$
$$\mu_3 = \mu/\alpha,$$
$$\alpha = \left(1 - \frac{x'}{R}\right).$$

(3.8)

By comparing Eq. (3.7) with Eq. (2.3), we note that the curved structure in Fig. 3-1(b) can be viewed as a straight one in Fig. 3-1(a) with effective $\tilde{\varepsilon}$ and $\tilde{\mu}$ tensors depending on the transverse coordinate x':

$$\tilde{\varepsilon} = \begin{bmatrix} \varepsilon_1 & 0 & 0 \\ 0 & \varepsilon_2 & 0 \\ 0 & 0 & \varepsilon_3 \end{bmatrix}, \quad \tilde{\mu} = \begin{bmatrix} \mu_1 & 0 & 0 \\ 0 & \mu_2 & 0 \\ 0 & 0 & \mu_3 \end{bmatrix}.$$

(3.9)

For a straight structure of $R \to \infty\,(\alpha = 1)$, the above formulas reduce to Eq. (1.?). By transforming curvilinear coordinates into Euclidian coordinates, the problem of a curved structure is transformed into an equivalent one of a straight structure with spatially dependent tensors of dielectric constant and magnetic permeability as shown in Fig. 3-2:
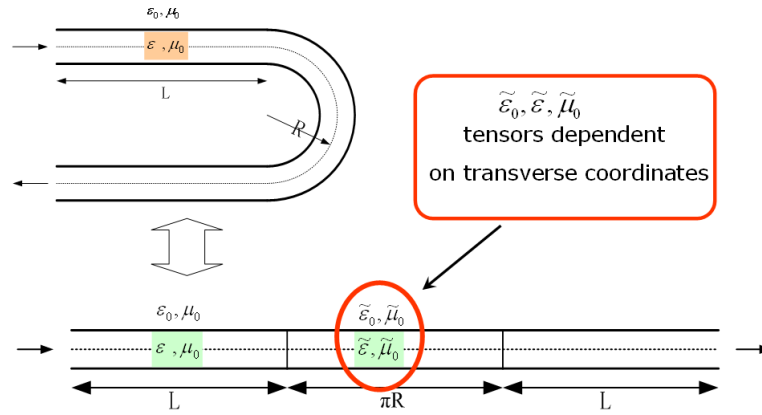
FIGURE 3-2. Transform a curved section into a straight one.

We note that equations (3.8) and (3.9) have almost the same form as in Sacks' uniaxial perfectly matched layer (UPML), i.e., no reflection occurs at a plane interface between two media with the same (ε, μ) but different α in Eqs. (3.8) and (3.9)[7]. The difference lies in that α of UPML is a complex constant which can give absorption at boundaries. Here α is a real number and varies with transverse coordinate x'. This indicates that the curved part of the waveguide is perfectly matched with the straight part in the s direction, but not in the x' and y' directions. When light travels from straight part to curved part, the reflection will be very little if the bend is not so sharp. In the straight waveguide the dispersive curves are nearly parallel lines, while in the curved one some of them intersect others, i.e., the group velocities are different for these modes.

3.3   Curved waveguide simulation

The simulation results presented in this section have been published in Ref. 10. When the curved waveguide is effectively considered as a straight one with $\left(\tilde{\varepsilon}(x'), \tilde{\mu}(x')\right)$ given by

Eqs. (3.8) and (3.9), we can apply the well-developed plane wave TMM (Refs. 4,5) to calculate the dispersion relations and eigenmode profiles in the curved waveguide in the same way as in a straight waveguide[8]. In the following, we consider a nanoribbon with a cross section of $360\,nm\,(x') \times 250\,nm\,(y')$ on a substrate, where the refractive indices $n_0 = 1.0,\ n_1 = 2.1,\ n_2 = 1.5$ (see Fig. 3-3, these parameters are close to the ones in Ref. 1).
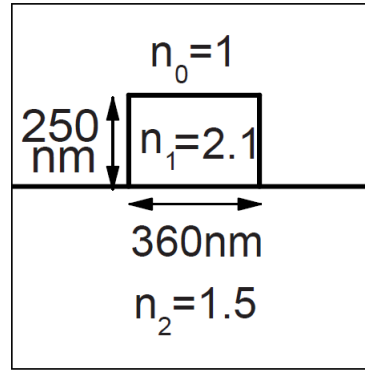
FIGURE 3-3. Geometry illustration of nanoribbon waveguide.

Figures 3-4(a) and 4(b) show respectively the dispersion relations for a straight waveguide and a curved one with $R = 2\,\mu m$; the insets give the $|E_x|$ $(|E_y|)$ distribution of the first (second) eigenmode with E_x (E_y) polarization at $600\,nm$. 19×19 plane waves for dispersive relation, 41×41 plane waves for the mode profile are used. The guided modes move downwards for a bent waveguide and the modal field shifts outwards from the center of curvature $(-x'$ direction$)$[9]. The first and fourth modes are E_x polarized, and the second and third modes are E_y polarized. Modes after the fifth mode are not as highly polarized as the first four modes.
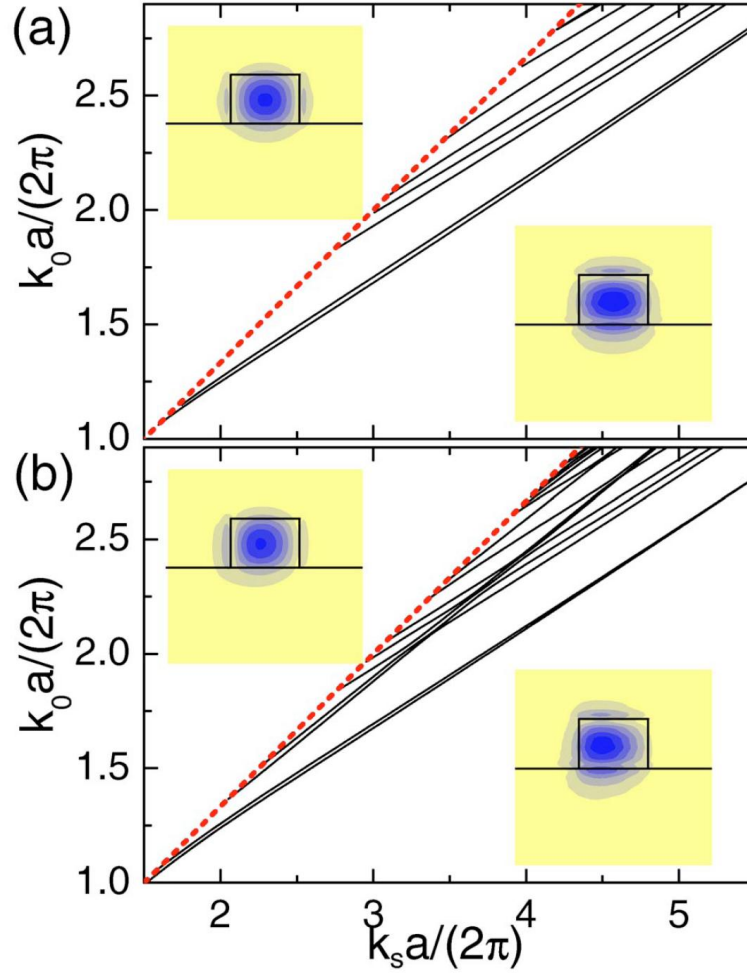
FIGURE 3-4. Dispersions of guided modes for (a) a straight waveguide and (b) a curved waveguide with $R = 2 \, \mu m$. The dashed line is the light line in substrate: $k_s = n_2 k_0$ $(k_0 = 2\pi / \lambda)$. The left (right) insets are $\left| E_x \right|$ $(\left| E_y \right|)$ distribution of the first (second) mode at $\lambda = 600 \, nm$.

We consider the transmission coefficients for a curved waveguide joint between two straight waveguides. The transmission and reflection coefficients can be computed following the steps in Refs. 8. Here we only present the self-transmission coefficients of guided eigenmode i $(i = 1, 2, ...)$, which are defined as the ratio of the transmission energy flux particular mode

i and the incident energy flux (only mode i incident). The reason for doing this is that in propagation along the straight waveguide, we expect that some guided modes are much more sensitive to waveguide imperfections (such as sidewall roughness) than others. These sensitive modes are much more likely to disappear during propagation.

We start from a simple "U" shape structure, made of two semi-infinite straight waveguides connected by a semicircular waveguide [see the inset in Fig. 3-5(a)]. First we set R to be $10\,\mu m$. The self-transmission of the first six guided eigenmodes is shown in Fig. 3-5(a). One can see regular fluctuations in transmission like in Ref. 1 but with much weaker amplitude. Our calculation shows that the reflection is very small ($<10^{-4}$, not shown here). That agrees well with the UPML form of $\tilde{\varepsilon}$ and $\tilde{\mu}$ in Eqs. (3.8)–(3.9), which indicates little reflection if the bend is not very sharp.

Then we try a "L" structure, made of two semi-infinite straight waveguides connected by a quarter-circular waveguide with $R = 20\,\mu m$. The result is shown in Fig. 3-5(b). The amplitude of transmission fluctuation is even weaker, but the position of the transmission peaks and bottoms of the first four modes are about the same compared to Fig. 3-5(a). It is interesting that the first two E_x-polarized modes (the 1st and 4th modes) have almost the same period, and the first two E_x-polarized modes (the 2nd and 3rd modes) also do so.
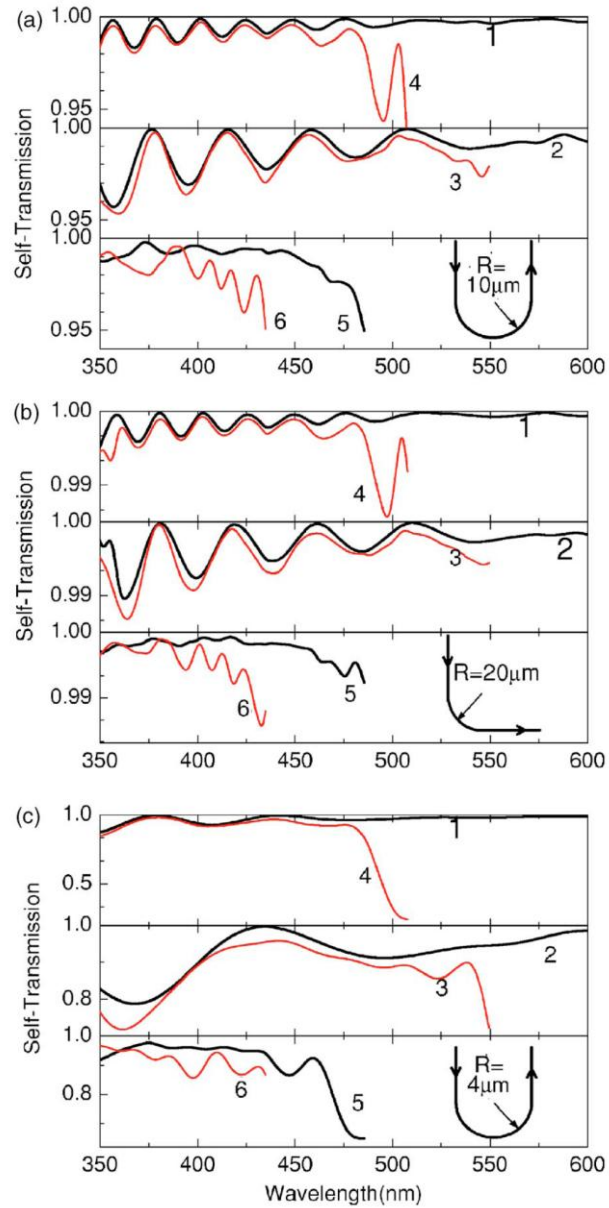
FIGURE 3-5. Self-transmission of the first six modes for: (a) a "U" structure of $R = 10 \ \mu m$, (b) an "L" structure of $R = 20 \ \mu m$, and (c) a "U" structure of $R = 4 \ \mu m$.

We tested structures with different curvatures and different span lengths. We found that: (i) the amplitude of transmission fluctuation decreases as R is increased and (ii) the period of transmission fluctuation is only related to the span length of the arc part and decreases as we

extend the arc part. The first rule is natural to understand. Smaller radius of curvature enlarges the perturbation to the system, causing the transmission to fluctuate more intensively (see Figure 3-5 (c), where R is set to be $4\,\mu m$). The second rule is like Fabry-Pérot (FP) effect at first view. However, it cannot be expained by FP effect since the reflection is so weak. Actually the mode conversion is responsible.

Let us begin from a simple model. Suppose there are two eigenmodes in the waveguide marked i and j for the straight part and i' and j' for the curved part. In the straight section, the two eigenmodes i and j propagates separately and there is no coupling between them. However, after they enter the curved part, they couple to each other and form two new eigenmodes i' and j'. If the arc part has length L , we can write down the self-transmission of mode i when the reflection is very small and can be neglected:

$$\left| t_{ii'} \exp(ik_i'L)t_{i'i} + t_{ij'} \exp(ik_j'L)t_{j'i} \right|^2 = \left| t_{ii'} \right|^4 + \left| t_{ij'} \right|^4 + 2\left| t_{ii'} \right|^2 \left| t_{ij'} \right|^2 \cos(\Delta k'L) \tag{3.10}$$

where $\Delta k' = k_j' - k_i'$; $t_{ii'}, t_{i'i}, t_{ij'}, t_{j'i}$ are the conversion coefficients from mode i to i', i' to i, i to j', j' to i, respectively, and $t_{ii'} = t_{i'i}^*, t_{ij'} = t_{j'i}^*$. Because $\Delta k'$ is not very sensitive to R, the period of transmission fluctuation is mainly related to the span length L of the curved section. The conversion between modes with the same polarization is much stronger than that between different polarization modes. So the first and fourth modes have similar self-transmission periods and the second and third modes also have similar periods. We calculate $\Delta k'$ as a function of wavelength between the first and fourth (the second and third) modes, from which we compute the period of transmission fluctuation. At $400\,nm$ the

calculated period is $22.4\,nm$ for the first and fourth modes, and $38.1\,nm$ for the second and third modes, which agrees well with the values of $23\,nm$ and $39\,nm$ in Figs. 3-5(a) and (b).

However, higher order modes are not highly polarized in either the x or the y direction, i.e. one of $|E_x|$ and $|E_y|$ is not much bigger than the other. The conversion rates between different polarized modes are not small. So their self-transmissions do not show fluctuations as regular as the first four modes [see the bottom plots of Figs. 3-5(a) and (b)].

Our numerical results suggest a possible explanation for the strong regular oscillation in the output spectrum observed by Law et al[1]. The oscillation period in Fig.1(c) in Ref. 1 is about $20\,nm$. From our previous calculation, $30\,\mu m$ span length of curved nanoribbon gives about $20\,nm$ oscillation period. However, the oscillation amplitude is around one half of the peak value of the intensity, which corresponds to below $4\,\mu m$ radius of curvature according to our previous calculation. The length of the curved section can not be as long as $30\,\mu m$ regarding the $4\,\mu m$ radius of curvature. So we expect there is a rippling section of nanoribbon [as shown in Fig. 3-6(a)], which has a small bending radius for the curved part.

We calculate the structure in Fig. 3-6(a) for different parameters, and one of the results is shown in Fig. 3-6(b). The parameters are $R = 3\,\mu m$, $L_1 = 1\,\mu m$, and $L_2 = 5\,\mu m$, and two periods of fluctuations [Figure 3-6(a) only shows one period]. The self-transmission diagram exhibits similar strong oscillations in the third, fourth, and fifth modes as in Ref. 1. Although the real structure is not like Fig. 3-6(a), since there is an air film between the rippling

nanoribbons and substrate, the calculation in Fig. 3-6(b) can be a rough estimation of the real structure and point out a very like possible origin of the strong regular intensity oscillations in Ref. 1.
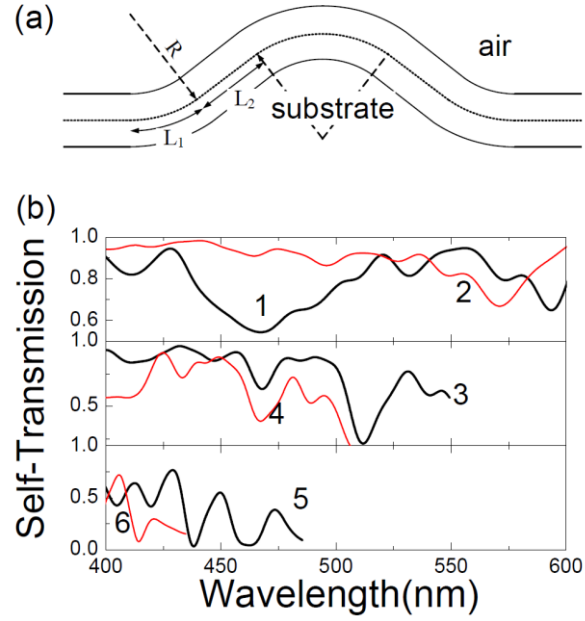

FIGURE 3-6. (a) Illustration of a waveguide containing a rippling section. (b) Self-transmission of the first six modes for the structure in (a) but of two periods of fluctuation, when $R = 3\ \mu m$, $L_1 = 1\ \mu m$, and $L_2 = 5\ \mu m$.

3.4   Summary

In summary, we have developed an improved TMM method in culvilinear coordinates to study bended nanoribbon waveguide. A curved section is equivalent to a straight one with effective $\tilde{\varepsilon}$ and $\tilde{\mu}$ as tensors and functions of transverse position. Tensors $\tilde{\varepsilon}$ and $\tilde{\mu}$ have the form of anisotropic PML but without absorption. Our method can be applied to any

shape of bended waveguide, which can be approximated by combination of many curved sections with different spans and curvatures.

The transmission spectra of straight-curved-straight waveguides are calculated and examined. We ended up by calculating a rippling section and pointed out that such a section in the nanoribbon waveguide is probably the origin of the strong regular intensity oscillations observed in Ref. 1.

References:

1. M. Law, D. J. Sirbuly, J. C. Johnson, J. Goldberger, R. J. Saykally, P. Yang, "Nanoribbon waveguides for subwavelength photonics integration", *Science* 305, 1269 (2004).

2. M. H. Huang, S. Mao, H. Feick, H. Q. Yan, Y. Y. Wu, H. Kind, E. Weber, R. Russo, P. D. Yang, "Room-Temperature Ultraviolet Nanowire Nanolasers", *Science* 292, 1897 (2001).

3. H. Kind, H. Yan, B. Messer, M. Law, P. Yang, "Nanowire Ultraviolet Photodetectors and Optical Switches", *Adv. Mater.* 14, 158 (2002).

4. Z. Y. Li and L. L. Lin, "Photonic band structures solved by a plane-wave-based transfer-matrix method", *Phys. Rev. E* 67, 046607 (2003).

5. Z. Y. Li and K. M. Ho, "Light propagation in semi-infinite photonic crystals and related waveguide structures", *Phys. Rev. B* 68, 155101 (2003).

6. M. Skorobogatiy, S. Jacobs, S. Johnson, Y. Fink, "Geometric variations in high index-contrast waveguides, coupled mode theory in curvilinear coordinates", *Opt. Express*, 10, 1227 (2002).

7. Z. S. Sacks, D. M. Kingsland, R. Lee, and J. F. Lee, "A perfectly matched anisotropic absorber for use as an absorbing boundary condition", *IEEE Trans. Antennas Propag.*

43, 1460 (1995).

8. Z. Y. Li and K. M. Ho, "Bloch mode reflection and lasing threshold in semiconductor nanowire laser arrays", *Phys. Rev. B* 71, 045315 (2005).

9. V. Van, P. P. Absil, J. V. Hryniewicz, and P. T. Ho, "Propagation loss in single-mode GaAs-AlGaAs microring resonators: Measurement and model", *J. Lightwave Technol.* 19, 1734 (2001).

10. Z. Ye, X. Hu, M. Li, K. Ho and P. Yang, "Propagation of guided modes in curved nanoribbon waveguides" *Appl. Phys. Lett.* 89, 241108 (2006).

Chapter 4. Go beyond planewave basis: localized optical orbital approach to photonic crystals

A new set of localized basis orbitals are introduced to locally represent electromagnetic field in photonic crystals. These orbitals are different from the optical Wannier functions. They are the optical parallelism of quasi-atomic orbitals in the context of electronic problems. We demonstrate the utility of these localized optical orbitals by recapturing eigenmodes in defected structures. Calculations for cavity modes and dispersion relations for waveguides agree well with the results from plane wave expansion calculations. This approach also offers interesting physical insight to understand the state of light in ideal photonic crystals as well as defected structures[1].

4.1   Introduction

One major aspect of all photonic crystal devices is that one or several highly localized defects are embedded in the perfect periodic photonic crystal background. In photonic crystal devices design, we usually need to simulate many different localized defect configurations (for example different shape, size or position) within the same perfect periodic photonic crystal structure. Therefore, a natural question to ask is: Can we treat the defects part and perfect periodic part separately first and then combines two parts together?

Before we answer this question, let's overview how traditional simulation tools works. Most traditional simulation tools such as planewave based transfer matrix method (TMM)[2] and finite difference time domain (FDTD)[3] will treat the photonic crystal devices (both the defects and the background) as a whole structure to calculate which means any change (even very slight change) of the defects will lead to a brand new calculation. For example, if 100 different cavity structures embedded in the woodpile structure are needed to simulate, TMM

and FDTD will need 100 times one cavity structure calculation time. And each one cavity structure calculation is not short for TMM and FDTD on three dimensional (3-D) cavity woodpile structures. A linear increase of calculation time will be expected for TMM and FDTD simulation as the number of cases studied increases.

One other thing need to emphasis is that both TMM and FDTD will increase simulation time as the calculation domain goes larger, and the defects size is relatively small compared to the whole device structure (usually less than 1/10 of the device). Or in other words, for each repeated different defect structure calculation, most calculation effort is devoted to the non-defect part which is a waste of time if we can separate the defect part and perfect part. This also leads to our natural question: Can we modify TMM or FDTD to realize the idea of separation? The answer is No. No modification is available for TMM and FDTD because both methods have to treat the structure as a whole.

Other methods can realize the idea of separation, such as localized Wannier functions (WFs)[4-8] and localized optical orbitals method (LOO) which will be presented in this chapter. The concept of these methods is to separate the photonic crystal devices at the very beginning: photonic crystal device = perfect photonic crystal + defects. First the perfect photonic crystal part can be calculated once for all. Then localized light orbitals are generated once for all variations of certain defects (for example variation of size, shape, location and refractive index). For any combination of those variations on defect, LOO can simulate much faster (detailed data later) than TMM or FDTD because only the variation part (only a fraction of whole domain) is re-calculated. Much better performance will be expected for LOO compared with TMM or FDTD especially when a lot of variations are studied, which is the inevitable task of industry design.

4.2   Localized optical orbitals v.s. optical Wannier funtions

Numerical methods using localized functions such as optical WFs and tight-binding approaches[9–11] have proven to be powerful tools to study the localized states in defected PCs. Optical Wannier functions, adopted from the electronic theory of solids[12–15], provide an alternative basis to plane waves to study the localized state of light in PCs. Much interest has been focused on WFs for its highly localized characteristic and usefulness for studying the defected systems. However, considerable steps of iteration are needed to get the maximally localized WFs[5]. In addition, a suitable set of trial functions to start the iteration is essential in this approach. To get these trial WFs, one has to guess the shapes and locations of them. Even with suitable trial WFs, one does not know what the final WFs will look like after iteration, since the iteration process is like a black box and the output WFs may be very different from the input trial functions. As a consequence, these uncertainties make the construction of WFs complex and not so direct.

In this chapter we suggest a different basis of highly localized functions as an alternative to WFs. The idea comes from the quasiatomic minimal basis orbitals (QUAMBOs) in the context of electronic theory of solids[16–18]. Like WFs, QUAMBOs are the linear combinations of Bloch orbitals. However, WFs are constructed through minimizing the transverse spread functional[4,5], yet QUAMBOs are obtained to let themselves be mostly like the free atomic orbitals. The QUAMBOs attained from this scheme contain the adaptation of the basis to the environments such as molecules or crystals, while keeping the essentially quasiatomic character in these environments[16]. The purpose of this chapter is to adapt the concept of QUAMBOs to optical systems. Ideal PCs or periodic alternate dielectric materials are like molecules while individual dielectric layers/columns/spheres that build up PCs are like atoms. The optical QUAMBOs should contain information of both "atoms" (individual dielectric blocks) and "molecules" (lattice of these blocks).

To construct these QUAMBO-like localized optical orbitals (LOOs), we project Bloch wave

solutions to optical states, which are analogous to free atomic orbitals, and orthogonize these projections to make them satisfy the general orthogonalization relation of WFs. Since LOOs and WFs share the same characteristic of localization and orthogonality, theoretically any WF-based scheme can be adapted to LOO method to study defected structures.

By comparison between the construction processes of these two bases, we see that LOOs are constructed through direct projection and orthogonalization, while WFs are constructed through iteration. The advantage of projection and orthogonalization lies in that they require much less computer time than iteration. Meanwhile, LOOs and the atomlike orbitals to be projected are very alike, and we can anticipate roughly what the LOOs will look like before they are constructed. But WFs and the trial functions to start iteration may be very different. We do not know what comes out when we put in trial functions. Another superiority of LOOs is its straightforward construction. We do not need to guess anything such as the shape of trial functions.

To illustrate our idea, LOOs are constructed to quantitatively describe the electromagnetic wave localization and propagation in one-dimensional (1-D) systems. We chose a 1-D system as our first example because this simplest structure offers a most straightforward description of LOO concept. Then this approach is extended to two-dimensional (2-D) case, where cavities and straight waveguides are studied. Numerical calculations by other methods[19–21] are also given as a comparison to testify our method. This work also suggests a possibility of using these optical QUAMBOs to study 3-D PCs.
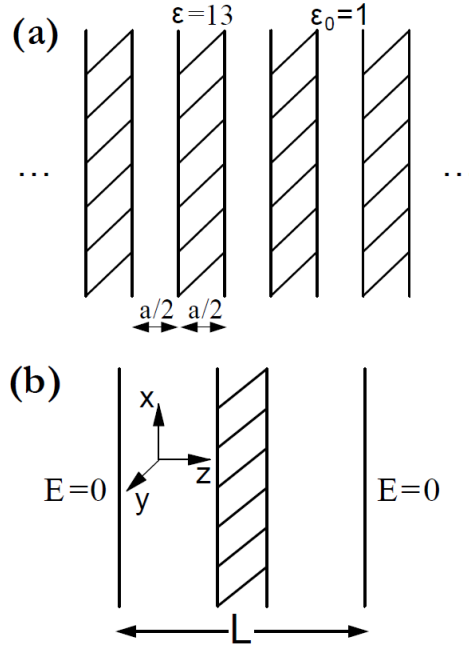
FIGURE 4-1: Structure of (a) a 1-D PC of dielectric layers in air, and (b) one dielectric layer with a perfect

conducting boundary.

4.3   Construction of localized optical orbitals in 1-D systems

Consider a 1-D PC shown in Fig. 4-1(a). It is a 1-D lattice of dielectric layers in air with dielectric constant $\varepsilon = 13$. The thickness of the dielectric layers is one half of the lattice constant a. The light that propagates in the z direction can be expressed by the electric field $E(\bar{z})$, which obeys the wave equation

$$\left[\frac{\partial^2}{\partial z^2} + \left(\frac{\omega}{c} \right)^2 \varepsilon_p(\bar{z}) \right] E(\bar{z}) = 0, \tag{4.1}$$

where we have assumed a time harmonic dependence, $E(\bar{z}, t) = E(\bar{z}) \exp(-i\omega t)$, of the

electric field with the frequency ω. $\varepsilon_p(\bar{z})$ is the dielectric index of the periodic structure

$\varepsilon_p(\bar{z}+\vec{R})=\varepsilon_p(\bar{z})$ and $\vec{R}$ is the lattice vector. Equation (4.1) has solutions to as the Bloch

functions, which satisfies the Bloch-Floquet theorem[22]

$$E_{n,\bar{k}}(\bar{z}+\vec{R})=e^{i\bar{k}\cdot\vec{R}}E_{n,\bar{k}}(\bar{z}), \qquad (4.2)$$

where n and $\bar{k}$ indicate the photonic band index and the wave vector.

To adapt the concept of QUAMBOs to this system, we first need to find solutions which are analogous to free atomic orbitals. However, the scattering nature of light does not allow such localized solutions unless a boundary is enforced to restrain photons from escaping. As Fig. 4-1(b) shows, we apply a perfect conducting boundary at both sides of a dielectric layer, which is like an "atom". We set the distance L between two ends to be $1.4a$. Note that the value of L cannot be too large compared to a, otherwise the atomlike optical orbitals are not well localized. Neither can L be smaller than a, to allow interaction between "atoms" (dielectric layers) to give a modulation of light. From our calculation, we find that the optimal value of L ranges from 1.2 to $1.5a$. In this range, the results are not sensitive to this boundary.

There are four solutions $E_m^{(0)}(\bar{z})$ $(m=1,2,...,N,N=4)$ in the normalized frequency range $\omega a/(2\pi c)=0.0\sim0.9$, as shown in Fig. 4-2(a). By projecting $E_m^{(0)}$ to $E_{n,\bar{k}}$, we get the projections[23,24]

$$\tilde{E}_m(\bar{z})=\sum_{n,\bar{k}}c_{m,n,\bar{k}}E_{n,\bar{k}}(\bar{z}), \qquad (4.3)$$

where coefficients $c_{m,n,\bar{k}}$ are defined as follows:

$$c_{m,n,\bar{k}} = \left\langle E_{n,\bar{k}} \mid \varepsilon_p \mid E_m^{(0)} \right\rangle = \int dz\, E_{n,\bar{k}}^*(\bar{z})\, \varepsilon_p(\bar{z})\, E_m^{(0)}(\bar{z}). \tag{4.4}$$

The integration runs over the entire space. Here we use Bloch waves $E_{n,\bar{k}}$ in the first four bands ($n = 1, 2, ..., N, N = 4$). We take 11 $\bar{k}$ points in the first Brillouin zone (BZ). Then we orthonormalize $\tilde{E}_m$ to get a basis $\tilde{E}_m'$ [25,26], which satisfy the relation $\left\langle \tilde{E}_m' \mid \varepsilon_p \mid \tilde{E}_{m'}' \right\rangle = \delta_{m,m'}$, and where $\tilde{E}_m'(\bar{z}) = \sum_{n,\bar{k}} c_{m,n,\bar{k}}' E_{n,\bar{k}}(\bar{z})$. We pick up the $\bar{k}$ component of $\tilde{E}_m'$ after the above orthogonalization

$$\tilde{E}_{m,\bar{k}}'(\bar{z}) = \sum_n c_{m,n,\bar{k}}' E_{n,\bar{k}}(\bar{z}), \tag{4.5}$$

and orthonormalize $\tilde{E}_{m,\bar{k}}'$ for each $\bar{k}$ to get a basis $\tilde{E}_{m,\bar{k}}''$, which satisfies $\left\langle \tilde{E}_{m,\bar{k}}'' \mid \varepsilon_p \mid \tilde{E}_{m',\bar{k}}'' \right\rangle = \delta_{mm'}$, and where $\tilde{E}_{m,\bar{k}}''(\bar{z}) = \sum_n c_{m,n,\bar{k}}'' E_{n,\bar{k}}(\bar{z})$. Summing up $\tilde{E}_{m,\bar{k}}''$ over $\bar{k}$ we can finally get a set of localized functions $\tilde{E}_m''(\bar{z}) = \sum_{\bar{k}} \tilde{E}_{m,\bar{k}}''(\bar{z})$, which can be satisfy the following orthogonality relation

$$\left\langle \tilde{E}_m''(\bar{z} - \bar{R}) \mid \varepsilon_p(\bar{z}) \mid \tilde{E}_{m'}''(\bar{z} - \bar{R}') \right\rangle = \delta_{mm'} \delta_{\bar{R},\bar{R}'}. \tag{4.6}$$

Following the above steps we construct an orthonormal basis $\tilde{E}_m''(\bar{z})$, i.e., LOOs. Note that here we follow the projection process in the works by Lu et al. [16,17] But QUAMBOs in these works are not an orthogonal set. Beyond projection, we also need an orthogonalization process to make LOOs be an orthonormal basis like WFs. One can easily see that LOOs

shares two major characteristics with WFs: the welllocalized property and the orthogonality, which is inherited from Bloch functions. Equation (4.6) has exactly the same form with the orthogonality equation in Refs. 4 and 5.
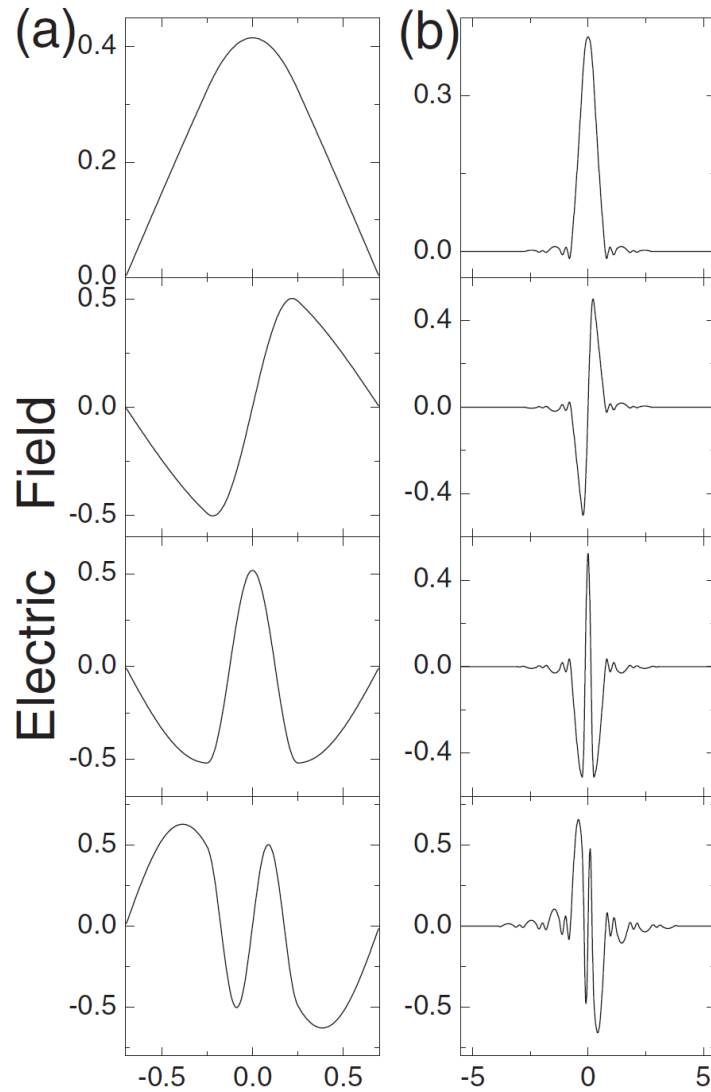

FIGURE 4-2. (a) The first four modes for one dielectric layer with boundary as shown in Fig. 4-1(b); (b) LOOs constructed from the four modes in (a) and Bloch wave solutions in the first four bands. The horizontal axis is the scale in the unit of lattice constant a.

In Fig. 4-2(b) we plot $\tilde{E}_m^{"}(\bar{z})$ $(m = 1, 2, ..., N, N = 4)$, which are obtained from the "free atom orbitals" shown in Fig. 4-2(a). We see that wiggling tails appear in $\tilde{E}_m^{"}(\bar{z})$ as a result of projection and orthogonalization. Instead of jumping to zero from finity at the boundary in original orbitals [see Fig. 4-2(a)], the magnetic field $H \sim \dfrac{\partial}{\partial z} E$ naturally undulates steadily to zero in Fig. 4-2(b). In some cases the wiggling tails extend to long distances and thus break the well-localized property of LOOs. Then we need to introduce virtual orbitals to reduce or get rid of these undesirable wiggling tails[27].

Since $\tilde{E}_m^{"}(\bar{z})$ owes the orthogonality relation to Eq. (4.6) just as WFs, we can directly transplant the method, which uses the same orthogonality relation of WFs to calculate the photonic band structure[4,5]. The electric field in Eq. (4.1) can be expanded in the basis of $\tilde{E}_m^{"}(\bar{z})$

$$E_{\bar{k}}(\bar{z}) = \sum_{m,\bar{R}} C_m e^{i\bar{k}\cdot\bar{R}} \tilde{E}_m^{"}(\bar{z} - \vec{R}), \tag{4.7}$$

where C_m are undetermined coefficients. By substituting Eq. (4.7) into Eq. (4.1) and applying the orthogonality of $\tilde{E}_m^{"}(\bar{z})$ [Eq. (4.6)], we obtain the following eigenvalue equation:

$$\sum_{m'} \left(\sum_{\bar{R}'} e^{i\bar{k}\cdot\bar{R}} A_{\bar{0}\bar{R}}^{mm'} \right) C_{m'} = \left(\frac{\omega}{c} \right)^2 C_m, \tag{4.8}$$

where

$$A_{\bar{R}\bar{R}'}^{mm'} = \left\langle \tilde{E}_m''(\bar{z} - \bar{R}) \left| -\frac{\partial^2}{\partial z^2} \right| \tilde{E}_{m'}''(\bar{z} - \bar{R}') \right\rangle$$

$$= \frac{a}{2\pi} \int_{BZ} d\vec{k} \, e^{i\vec{k}\cdot(\bar{R}-\bar{R}')} \sum_{n=1}^{N} c_{m,n,\vec{k}}''^{*} \left(\frac{\omega_{n,\vec{k}}}{c} \right)^2 c_{m',n,\vec{k}}''.$$

(4.9)

By solving the eigenvalue matrix in Eq. (4.8), we reproduce the photonic band structure in the LOO basis. The result is shown in Fig. 4-3. As Eq. (4.9) indicates, there are two ways to calculate the matrix $A_{\bar{R}\bar{R}'}^{mm'}$. One is to integrate over $\bar{z}$ in real space, the other is to integrate over $\vec{k}$. They both can yield exact reproduction of the photonic band structure. The band structure shown in Fig. 4-3 is computed from the integral in $\vec{k}$ space. Solid lines indicate the band structure calculated by plane-wave expansion (PWE) method, and dots by using LOO basis. It can be seen that our method agrees quite well with PWE in the first four bands.
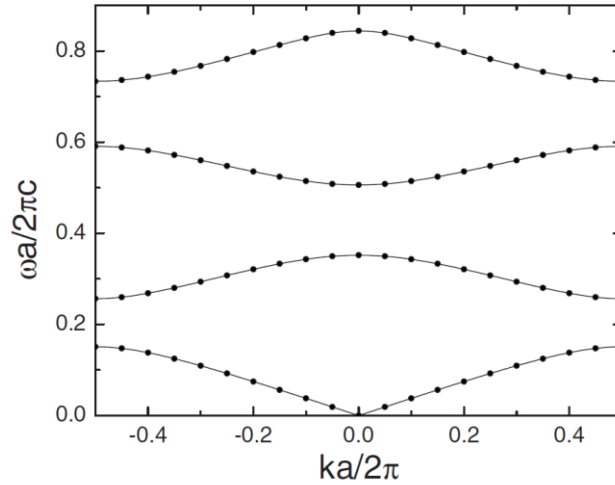

FIGURE 4-3. Band structure of 1-D PC in Fig. 4-1(a) calculated by PWE (solid line) method and reproduced by LOO (dots) method.

4.4   Defect structures in 1-D photonic crystals

In the presence of a defect $\delta\varepsilon(\bar{z})$ over the periodic permittivity function $\varepsilon_p(\bar{z})$, the electric field Maxwell wave equation Eq. (4.1) should be rewritten as

$$-\frac{\partial^2}{\partial z^2}E(\bar{z}) = \left(\frac{\omega}{c}\right)^2 \varepsilon(\bar{z})E(\bar{z}), \tag{4.10}$$

where $\varepsilon(\bar{z}) = \varepsilon_p(\bar{z}) + \delta\varepsilon(\bar{z})$. We expand the electric field in Eq. (4.10) as follows:

$$E(\bar{z}) = \sum_{m,\bar{R}} C_{m,\bar{R}} \tilde{E}_m^{"}(\bar{z}-\bar{R}), \tag{4.11}$$

where $C_{m,\bar{R}}$ are coefficients to be determined. By substituting Eq. (4.11) into Eq. (4.10) and applying the orthogonality of $\tilde{E}_m^{"}(\bar{z})$, we obtain the following tight-binding matrix equation:

$$\sum_{m',\bar{R}'} A_{\bar{R}\bar{R}'}^{mm'} C_{m',\bar{R}'} = \left(\frac{\omega}{c}\right)^2 \sum_{m',\bar{R}'} \{\delta_{mm'}\delta_{\bar{R}\bar{R}'} + D_{\bar{R}\bar{R}'}^{mm'}\}C_{m',\bar{R}'}, \tag{4.12}$$

where

$$D_{\bar{R}\bar{R}'}^{mm'} = \left\langle \tilde{E}_m^{"*}(\bar{z}-\bar{R}) \mid \delta\varepsilon(\bar{z}) \mid \tilde{E}_{m'}^{"}(\bar{z}-\bar{R}') \right\rangle, \tag{4.13}$$

and $A_{\bar{R}\bar{R}'}^{mm'}$ is defined as before in Eq. (4.9). The above is the scheme in Refs. 4 and 5 except that LOOs are used as basis instead of WFs.
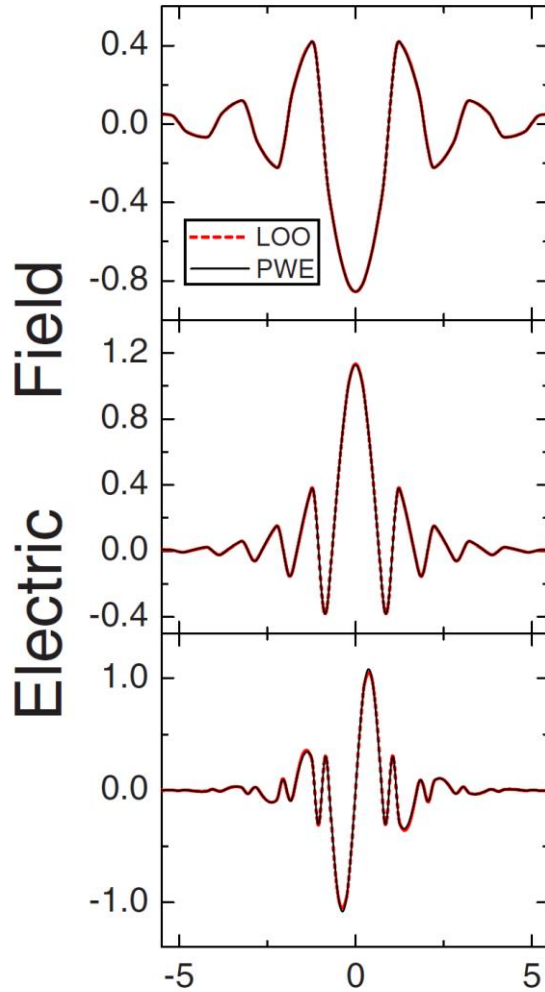
FIGURE 4-4. The first three cavity modes from PWE (solid/black) and LOO (dashed/red)

calculations. The horizontal axis is the scale in the unit of a.

As a numerical example, we study a structure with one dielectric layer missing. Figure 4-4 shows the first three eigenmode profiles computed from plane-wave expansion method[19] and our method. In this calculation, we use six LOOs that are constructed from 66 Bloch wave solutions in the first six bands. Exact agreement is achieved in the mode shape and we can hardly see any error. Normalized frequencies for these three cavity modes are 0.24056, 0.37649, 0.67364 / 0.23991, 0.37615, and 0.67186 given by LOO / PWE calculations, respectively. The maximum relative difference is 0.27%.

4.5   Localized optical orbitals in 2-D photonic crystals and defected structures

In sections 4.2 and 4.3, we illustrate the concept of LOOs by a 1-D example. In this example, each dielectric layer in air can be compared to an isolated atom. These atomlike layers are connected to form a crystal. The state of light that propagates in the crystal can be expanded in the quasiatomlike basis. The basis constructed in this way contains information of both the isolated atoms and lattice made of the atoms. After this 1-D example, it is expected to extend our LOO method to 2-D cases, where each dielectric pole can be regarded as an atom.
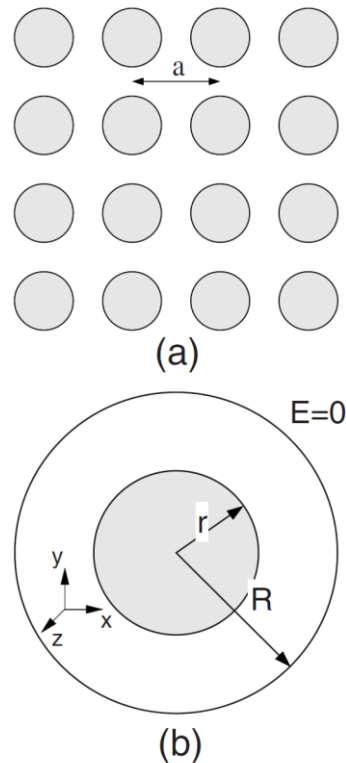

FIGURE 4-5. Structure for (a) a 2D PC with a square lattice of dielectric rods in air, and (b) one dielectric column with a cylindrical perfect conducting boundary.

Consider a square lattice of dielectric columns in air as shown in Fig. 4-5(a). The cylinder

has a dielectric constant 9.0 and a radius $r = 0.35a$, where a is the lattice constant. This structure has a 2-D photonic band gap from 0.251 to 0.29 for transverse magnetic (TM)-polarization and another gap from 0.425 to 0.493 in the normalized frequency $\omega a / (2\pi c)$.
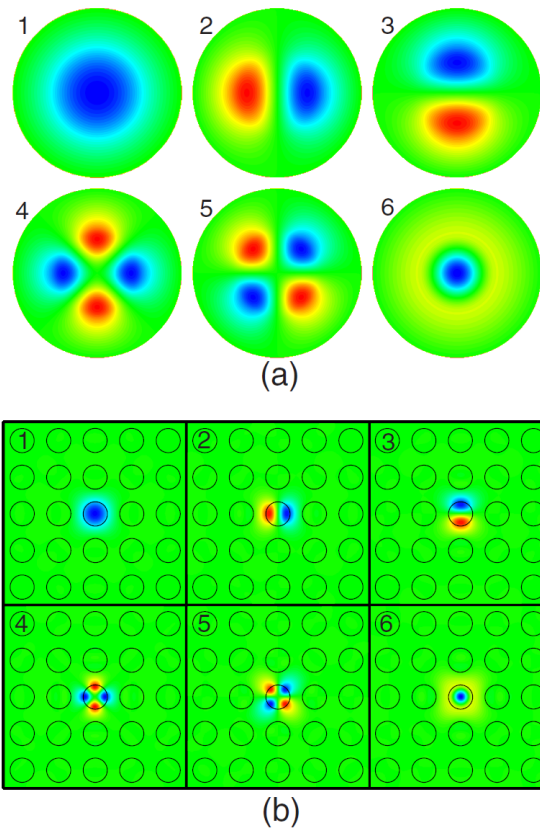

FIGURE 4-6. (a) The first six modes for one dielectric column with a cylindrical boundary as shown in Fig. 4-5(b); (b) LOOs constructed from the six modes in (a) and Bloch wave solutions in the first six bands.

To find solutions corresponding to free atomic orbitals, again a boundary is needed to restrain light from escaping. We apply a cylindrical perfect conducting boundary to the dielectric

cylinder as shown in Fig. 4-5(b). The radius of the boundary R is set to be $0.7a$. This value is chosen for the same reason as in 1-D case. For the structure in Fig. 4-5(b), there are six TM-polarized solutions E_z ($\vec{z}$ is along the direction of dielectric columns) in the normalized frequency range $\omega a/(2\pi c) = 0.0 \sim 1.0$, as shown in Fig. 4-6(a). All of these solutions are products of Bessel functions of first/second kind, and an angular function $e^{im\pi}$, where m is an integer. In finding these solutions, we need to consider the symmetry. The second and third solutions are twofolded, while the fourth and fifth fourfolded, and they all appear in pairs.

From these six solutions and Bloch eigenstates of PC in the first six bands, we construct six E_z LOOs using the same technique developed in 1-D case. We take 7×7 $\vec{k}$ points in the whole BZ, when constructing the LOOs. As indicated in Fig. 4-6(b), their localization properties as well as the symmetries of the underlying PC structure are clearly visible. We note that through this way of construction, all the LOOs are localized at dielectric rods. This property is different from that of optical WFs, where some of the WFs are localized at air regions[4,5].

In Fig. 4-7, we show the photonic band structure in black points reproduced by the E-field LOOs. Solid lines indicate the photonic band structure calculated with 441 plane waves by the PWE method. The solid lines (PWE) and the dots (LOO method) coincide. We use the same method in Refs. 4 and 5 in reproducing the band structure by LOOs.
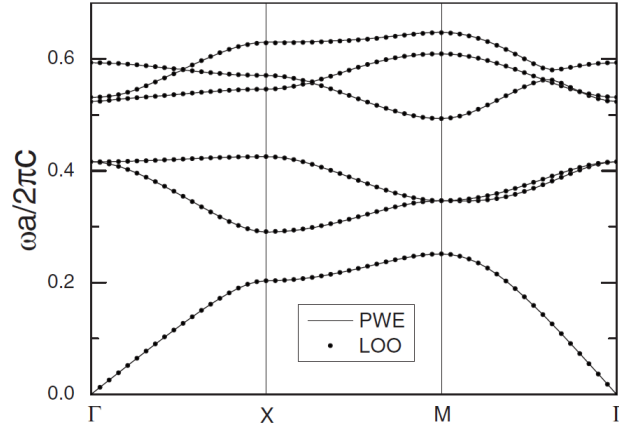
FIGURE 4-7. Band structure (TM polarized) of the 2-D PC in Fig. 4-5(a), calculated by PWE

(solid line) method and reproduced by LOO (dots) method.

We consider a cavity with one dielectric cylinder removed from the ideal PC. We apply the E-field LOO method to the calculation of the cavity mode. We take six LOOs in the calculation. As before, the scheme is the same as in Refs. 4 and 5, except that we use LOOs instead of optical WFs. The resonant frequency of the cavity mode in the second band gap is 0.48303 by LOO method versus 0.48017 in normalized frequency $\omega a / (2\pi c)$ by transfer matrix method (TMM) (see Refs. 2 and 21). The relative difference is 0.60%.

In Fig. 4-8(a), we plot the cavity mode profile computed by LOO method. Mode shape computed by TMM is also plotted as a comparison in Fig. 4-8(b). A 7×7 supercell and 105 plane waves are taken to do the TMM calculation. As we can see in Fig. 4-8, the mode shapes calculated by the two methods look alike but there is still visible difference. The difference around the edges of supercell can be explained by the interaction between supercells in TMM calculation and thus can be neglected. However, there is noticeable difference in the central and the third peaks that can only be explained by the inaccuracy of

LOO method. After testing, we ascribe this error to the inadequate LOOs. If we increase the number of LOOs, the difference is reduced and the whole mode shape is more like what is obtained by TMM.
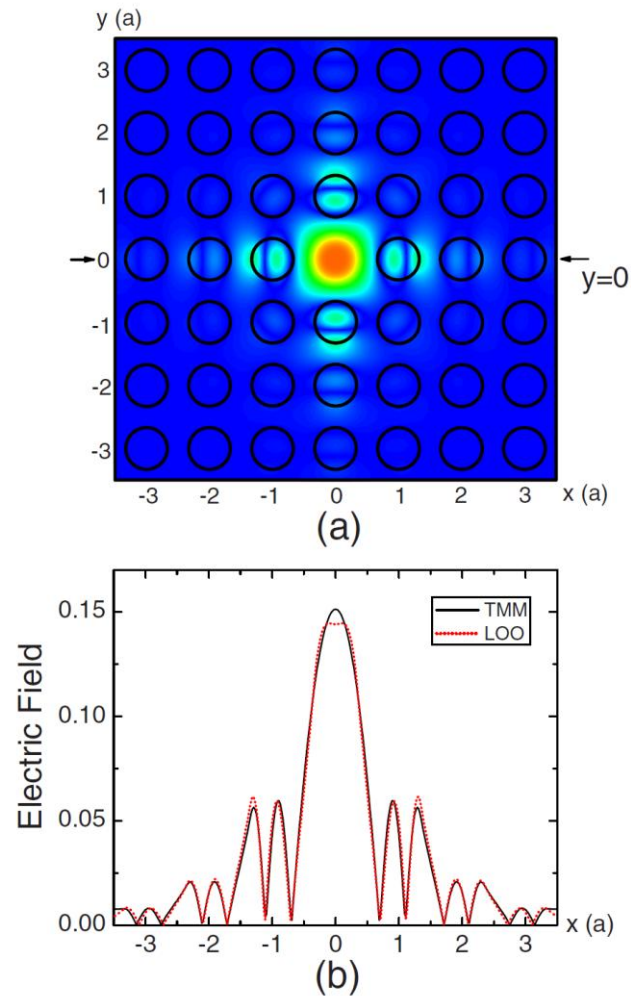

FIGURE 4-8. Cavity mode profile. (a) Electric field distribution (magnitude) calculated by LOO method; (b) magnitude of electric field at $y = 0$ calculated by TMM (solid/black) and LOO (dots/red) methods.

Next, we consider a waveguide consisting of one removed line of dielectric rods. We use the method in Refs. 4 and 5 to calculate the guided mode. Figure 4-9 shows the dispersion

relation of the guided mode in the first gap in the LOO method (dots) and in PWE (solid lines). As indicated in the figure, the solid lines and the dots coincide very well. We take six LOOs in LOO calculation, and a 7×1 supercell and 105 plane waves in PWE calculation.
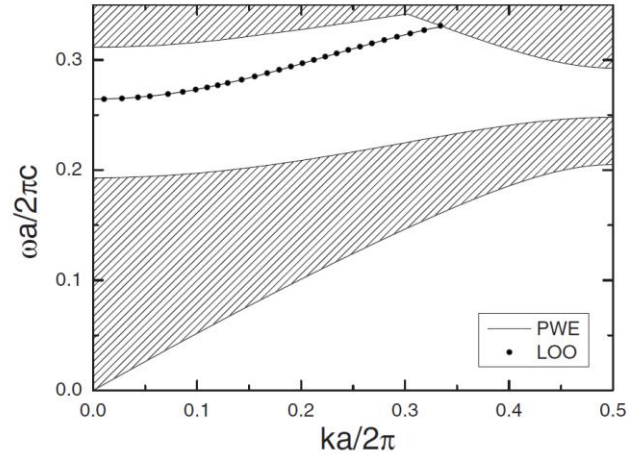

FIGURE 4-9. Dispersion relation of guided mode calculated by PWE (solid line) and LOO (dots) methods.

4.6   How much computation time can LOO method save?

— Disorder simulation comparison between LLO and TMM

To get a better understanding of how LOO deals with disorder, we perform a set of simulation on dielectric variation disorder on the cavity the Figure 4-8(a). This disorder is simulated by varying the dielectric constant of neighborhood cylinders around the cavity: H means increase the dielectric constant to 10, and L means decrease the dielectric constant to 8 for that particular cylinder (Figure 4-10). A total of 15 cases are studied by both TMM and LOO: TMM requires 15600 seconds, and LLO requires 1720 seconds. The results are summarized in Table 4.1.

The resonant frequencies for each case are compared and the scatter plot is shown in Fig.

4-11. Almost linear response to $y = x$ is observed in this particular simulation which indicates systematic consistency has been achieved between LOO and TMM.
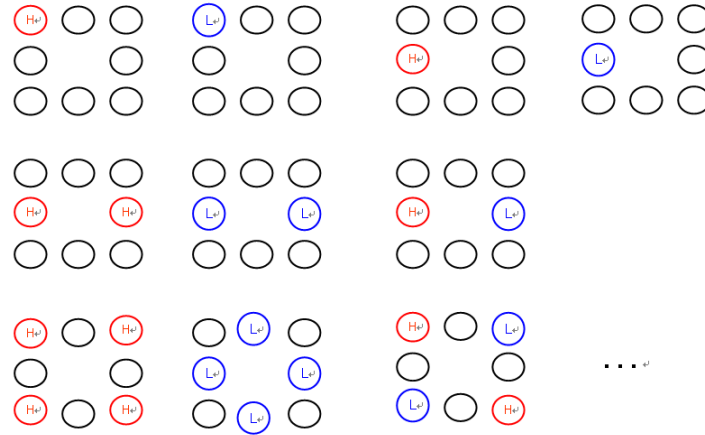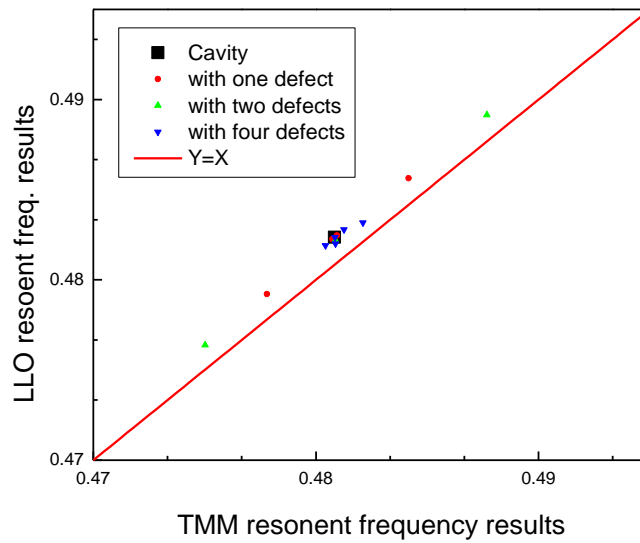

FIGURE 4-10. Types of disorders around the cavity

FIGURE 4-11. Scatter plot of cavity resonant frequencies (LOO v.s. TMM)

Table 4.1. Computation time of TMM and LOO for 15 case studies

Method	Computation time for each case (seconds)	Total computation time for 15 cases (seconds)
TMM	1040	$15 \times 1040 = 15600$
LOO	20	$1420* + 15 \times 20 = 1720$

* 1420 seconds are needed to construct LOOs, which needs to be done only ONCE.

4.7   Conclusions

In conclusion, we develop a QUAMBO-like, E-field LOO method to study localized states of defected PCs. We have demonstrated the applicability, precision, and efficiency of LOO method to 1-D and 2-D PCs with planar, point, and line defects. The structures that we took as examples both have analytical solutions corresponding to free atomic orbitals. However, for those structures that do not have analytical free-atomlike solutions such as lattice of arbitrary shaped poles, we need to use numerical methods such as FDTD[3] to find these solutions. This will add little to calculation burden, since it is over a region that is comparable to one unit cell.

Our method can be extended to the description of optical waves in 3-D PCs, by applying the same scheme of optical WFs in Ref. 5. The reason which allows us to do so is that the only difference between LOO and optical WF method lies in the way of construction of LOOs/WFs. Since the two bases share the same characteristic of localization and orthogonality, theoretically any WF-based scheme (e.g., see Refs. 4, 5, and 7) can be adapted to LOO method. Our future work includes study of propagation of electromagnetic waves in 3-D PCs by applying LOO method. Some numerical results in this chapter were published in Ref. 1.

References:

1. Z. Ye, X. Hu, M. Li, K. M. Ho, J. Cao and M. Miyawaki, "Localized optical orbital approach to study localized states of light in photonic crystals" *Phys. Rev. B* 80, 035111 (2009).

2. Z. Y. Li and L. L. Lin, "Photonic band structures solved by a plane-wave-based transfer-matrix method", *Phys. Rev. E* 67, 046607 (2003).

3. *Computational Electrodynamics: The Finite-Difference Time-Domain Method*, edited by A. Taflove (Artech House, Bouston, MA, 1995).

4. K. Busch, S. F. Mingaleev, A. Garcia-Martin, M. Schillinger, and D. Hermann, "The Wannier function approach to photonic crystal circuits", *J. Phys.: Condens. Matter* 15, R1233 (2003).

5. H. Takeda. A. Chutinan, and S. John, "Localized light orbitals: Basis states for three-dimensional photonic crystal microscale circuits", *Phys. Rev. B* 74, 195116 (2006).

6. J. P. Albert, C. Jouanin, D. Cassagne, and D. Bertho, "Generalized Wannier function method for photonic crystals", *Phys. Rev. B* 61, 4381 (2000).

7. Y. Jiao, S. Fan, and D. A. B. Miller, "Systematic photonic crystal device design: Global and local optimization and sensitivity analysis", *IEEE J. Quantum Electron.* 42, 266 (2006).

8. D. M. Whittaker and M. P. Croucher, "Maximally localized Wannier functions for photonic lattices", *Phys. Rev. B* 67, 085204 (2003).

9. A. Yariv, Y. Xu, R. K. Lee, and A. Scherer, "Coupled-resonator optical waveguide: a proposal and analysis", *Opt. Lett.* 24, 711 (1999).

10. M. Bayindir, B. Temelkuran, and E. Ozbay, "Tight-binding description of the coupled defect modes in three-dimensional photonic crystals", *Phys. Rev. Lett.* 84, 2140 (2000).

11. D. P. Fussell and M. M. Dignam, "Engineering the quality factors of coupled-cavity modes in photonic crystal slabs", *Appl. Phys. Lett.* 90, 183121 (2007).

12. G. H. Wannier, "The structure of electronic excitation levels in insulating crystals", *Phys. Rev.* 52, 191 (1937).

13. W. Kohn, "Construction of Wannier functions and applications to energy-bands", *Phys. Rev. B* 7, 4388 (1973).

14. N. Marzari and D. Vanderbilt, "Maximally localized generalized Wannier functions for composite energy bands", *Phys. Rev. B* 56, 12847 (1997).

15. I. Souza, N. Marzari, and D. Vanderbilt, "Maximally localized Wannier functions for entangled energy bands", *Phys. Rev. B* 65, 035109 (2002).

16. W. C. Lu, C. Z. Wang, T. L. Chan, K. Ruedenberg, and K. M. Ho, "Representation of electronic structures in crystals in terms of highly localized quasiatomic minimal basis orbitals", *Phys. Rev. B* 70, 041101(R) (2004).

17. W. C. Lu, C. Z. Wang, M. W. Schmidt, L. Bytautas, K. M. Ho, and K. Ruedenberg, "Molecule intrinsic minimal basis sets. I. Exact resolution of ab initio optimized molecular orbitals in terms of deformed atomic minimal-basis orbitals", *J. Chem. Phys.* 120, 2629 (2004).

18. T. L. Chan, Y. X. Yao, C. Z. Wang, W. C. Lu, J. Li, X. F. Qian, S. Yip, and K. M. Ho, "Highly localized quasiatomic minimal basis orbitals for Mo from ab initio calculations", *Phys. Rev. B* 76, 205119 (2007).

19. K. M. Ho, C. T. Chan, and C. M. Soukoulis, "Existence of a photonic gap in periodic dielectric structures", *Phys. Rev. Lett.* 65, 3152 (1990).

20. P. Lalanne, "Effective properties and band structures of lamellar subwavelength crystals: Plane-wave method revisited", *Phys. Rev. B* 58, 9801 (1998).

21. M. Li, Z. Y. Li, K. M. Ho, J. R. Cao, and M. Miyawaki, "High-efficiency calculations for three-dimensional photonic crystal cavities", *Opt. Lett.* 31, 262 (2006).

22. J. D. Joannopoulos, S. G. Johnson, J. N. Winn, and R. D. Meade, *Photonic Crystals:*

Molding the Flow of Light (Princeton University, Princeton, NJ, 1995).

23. For this 1-D structure, since the bands are separate from each other, actually the projection can be simplified as projecting $E_n^{(0)}$ to $E_{n,\bar{k}}$. That is, calculating a LOO only requires the states in one band. However, for the more general case of 2-D and 3-D structures, the bands are always entangled. So we need to project $E_m^{(0)}$ to $E_{n,\bar{k}}$ for all (m,n)s. Here we write down the general form of projection [Eq. (7.3)] to accommodate 2-D and 3-D structures.

24. In this projection, all bands are included. Yet our method is exact not only in the limit that all bands are included in the projection but also in cases that only some of bands are included, as far as a perfect crystal is considered.

25. We define a general linear transformation T for the basis Φ to go to a new basis Φ' : $\Phi' = \Phi T$. The basis Φ' will be orthonormal if $\langle \Phi' | \Phi' \rangle = \langle \Phi T | \Phi T \rangle = T^{\dagger} \langle \Phi | \Phi \rangle T = I$. Define a Hermitian matrix $M = \langle \Phi | \Phi \rangle$. The matrix $T = M^{-1/2} = V D^{-1/2} V$, where D is the diagonal matrix of eigenvalues of M and V is the full matrix whose columns are the corresponding eigenvectors, gives an orthonomal transformation. For more details on this symmetric orthogonalization, see Ref. 27.

26. V. Srivastava, "A unified view of the orthogonalization methods", *J. Phys. A* **33**, 6219 (2000).

27. To get virtual orbitals, we use the same method as in Ref. 16. In this paper all orbitals are real/occupied, which is a specific case of the method in Ref. 16 [there are no virtual Bloch orbitals φ_p in Eq. (1) in Ref. 16].

Chapter 5. Emission enhancement of organic light emitting diodes with microlens array: Numerical simulation

We theoretically investigate the enhancement in the emission of organic light emitting diodes (OLEDs) in the forward direction using a microlens array. We show that a microlens array significantly larger than the OLED pixel can extract a large part of the light guided in the glass substrate into the front direction. An enhancement as much as ~140% can be achieved. The content of this chapter is a part of an ongoing project in cooperation with experimentalists. Our role is to numerically simulate the OLEDs with or without microlens array. This chapter will focus on theoretical investigation and simulation only. A short description of fabrication method will be attached in the appendix after this chapter.

5.1   Introduction

Organic light emitting diodes, or OLEDs, are among the best candidates for the next generation light source. In an OLED, the emissive electroluminescent layer is a film of organic compounds which emit light in response to an electric current. Compared to other display technologies like liquid crystal displays (LCDs) or plasma displays, OLEDs have the advantage of light and thin, excellent color, high contrast ratio, and expected low cost in the future[1,2].

However, there is an inherent limitation to light extraction due to the difference between the refractive indices of the organic light-emitting materials and air. Only a small part of the emitted light from the active layers can escape into the air, The fraction of light which escapes in the forward direction is $\sim (1-\cos\theta_c)$,[3] where θ_c is the critical angle for the active layer. In OLEDs, the refractive index of the organic layer (the emitting material) is

~ 1.8 and the fraction of the extracted light is only ~ 17% . For inorganic LEDs, this number is ever lower. As a result, most light is guided in the active layers or the substrate. The majority of this trapped light is either reabsorbed or leaks out from the device edges.

Several approaches to enhance the light extraction have been developed[4-7]. Among them one promising approach is the use of microlens arrays[6,7]. However, the microlens array is often confined to an area directly under the OLED pixel. As a result, only a limited part of the light guided in substrate can escape through the microlens, and the outcoupling enhancement is constrained to ~ 50% to 80% .
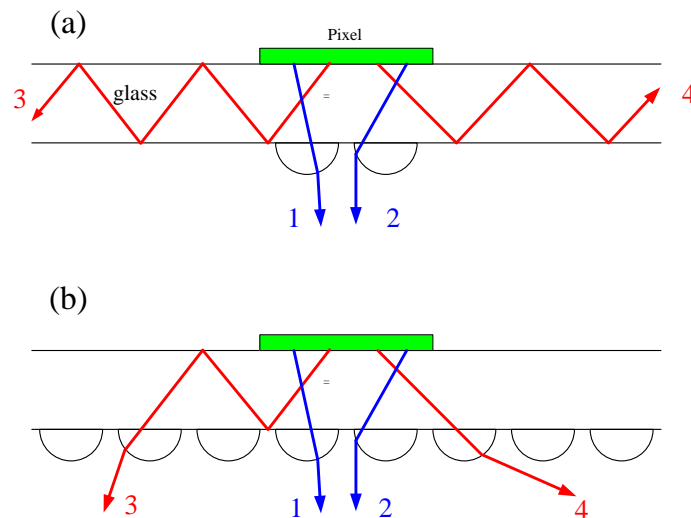

FIGURE 5-1. Schematic of an OLED with a microlens array confined to an area (a) only directly under the pixel, (b) much larger than the pixel.

To illustrate it, let's consider an OLED shown in Fig. 5-1. If the microlens array is only confined to an area directly under the pixel as shown in Fig. 5-1(a), some of light trapped in glass will not be outcoupled via microlens like beam 3 and 4. However, if we extend the area

covered by the microlens to a sufficient large scale [see Fig. 5-1(b)], a large part of the trapped light like beam 3 and 4 will be extracted via microlens.

Let's consider the extreme case of an infinite large area covered by microlens array and also an infinite large metal cathode. A beam trapped in the substrate would either be coupled out through a microlens or bounce back with a changed or unchanged incident angle when it hit the glass/microlens or glass/air interface. If it bounces back, it will also bounce back at the metal cathode and reach the glass/microlens or glass/air interface again. Then it would still have a chance to be coupled out through a microlens at the second time. In a sum, this beam can always "find" a microlens to help it escape after several bounces in between the cathode and glass. In this extreme case, all the light trapped in glass can be coupled out through the microlens array, if we neglect absorption in materials and assume 100% reflection at the metal cathode.

In this work we propose a microlens array design for OLEDs with the patterned microlens array significantly larger than the pixels. We numerically investigate the effect of microlens array on the extraction of the trapped light in glass by a statistic ray tracing method. We also study in detail how big the microlens-covered area should be compared to the pixel to extract most of the trapped light.

5.2   Statistic ray tracing method

The numerical method we are going to use in this chapter is similar to a traditional non-sequential tray tracing method. The term "non-sequential" means that there is no pre-defined path for any ray. A ray is launched and hits whatever object is in its path, and it may then reflect or refract. In commercial software like ZEMAX[8] designed for optical engineers, when a ray hits the surface of an object, the fraction of energy transmitted and

reflected at the interface is computed. Then the ray is split into two: a reflected and a transmitted ray, with the corresponding fraction of energy. Non-sequential ray-tracing is a far more general technology than sequential ray-tracing. However, it is also far slower since at each intersection a ray is split into two child rays.

To avoid the slow tracing speed, we are going to use a statistic ray-tracing method. Instead of splitting rays, at each intersection we let the ray randomly "choose" to reflect or refract with the probability equal to the calculated reflectance or transmittance. For each initial ray, there is one but only one ray from the beginning to the end. However, the ray undergoes a path that is randomly selected instead of predefined. This method is a compromise between sequential and non-sequential ray-tracing. We want it to achieve what the latter does, while we want a tracing speed comparable to the former.

In the following we explain the statistic ray-tracing step by step:

1. Generate a ray from a random position (x_0, y_0, z_0) in pixel area, with random direction (θ_0, φ_0) and an initial intensity of $A_0 = 1$. The polarization is also randomly selected to be TE or TM.

2. From (x_0, y_0, z_0) and (θ_0, φ_0), calculate the ray path and then the intersection (x_1, y_1, z_1) where the ray hits whatever object is in its path. If the ray was propagating in an absorptive medium, calculate the exponential decay and update the intensity A_0 accordingly.

3. Decide the plane of incidence, the incident angle α_i. Then calculate the angle of

transmission α_t from Snell's law. The reflectance R and transmittance T can be obtained from Fresnel's equations. The formula to calculate α_t, R and T is listed in Eq. (5.1),

$$\alpha_r = \alpha_i,$$

$$\alpha_t = \sin^{-1}\left(\frac{n_i \sin \alpha_i}{n_t}\right),$$

$$r_{TE} = \frac{n_i \cos \alpha_i - n_t \cos \alpha_t}{n_i \cos \alpha_i + n_t \cos \alpha_t},$$

$$r_{TM} = \frac{n_t \cos \alpha_i - n_i \cos \alpha_t}{n_i \cos \alpha_t + n_t \cos \alpha_i},$$

$$t_{TE} = \frac{2n_i \cos \alpha_i}{n_i \cos \alpha_i + n_t \cos \alpha_t},$$

$$t_{TM} = \frac{2n_i \cos \alpha_i}{n_i \cos \alpha_t + n_t \cos \alpha_i},$$

$$R = |r|^2,$$

$$T = 1 - R,$$

(5.1)

where n_i and n_t are the refractive indices of the medium where the light is propagating from and the medium where the light is propagating to, respectively.

4. Randomly generate a number x in the range of $(0,1)$. If $x < R$, let the ray be reflected. Otherwise let the ray be transmitted. Update (x_0, y_0, z_0) and (θ_0, φ_0) accordingly. Return to step 2, and repeat steps 2-4 until beam escapes to the air, or totally absorbed by the material.

5. Record the intensity of the escaped beam. Return to step 1 to generate another ray, and

repeat steps 1-5 until enough rays (usually $>10,000$) are generated.

5.3   Light extraction from a flat OLED (no microlens)

The green OLED structure that we are going to model is shown in Fig. 5-2. The thickness of glass, ITO, organic layers and aluminum cathode is labeled. The light sources (origin of beams) are marked in yellow dots and set to be 1 nm above the interface of NPD and Alq3.
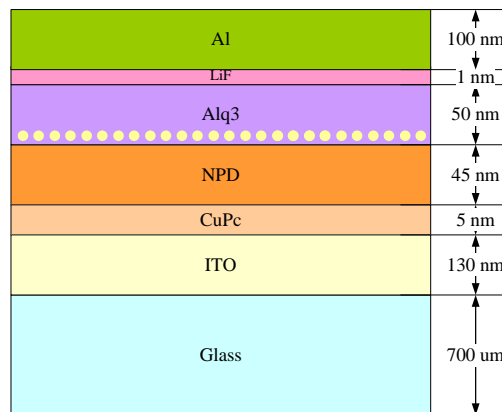

FIGURE 5-2. Schematic of OLED with sources (yellow dots) embedded 1 nm above

the interface of NPD and Alq3.

In our ray tracing simulation, the absorption loss in materials and the reflection loss at the metal cathode are both considered. The simulation gives an extraction of 15.3% which is a little smaller than 17% by taking solid angles smaller than the critical angle without any absorption. In this simulation, the refractive indices of materials at $525\,nm$ are used. We plot a ray tracing diagram for 50 rays in Fig. 5-3 (in real simulation the extraction is obtained by tracing $10,000$ rays), to give a view of how ray tracing works. Each source is marked by red dot. In the plot, we can only see the glass substrate. Other layers such as ITO,

organic layers, aluminum are too thin compared to glass to be recognized in the figure. As we can see, a lot of rays are trapped in the glass, and only a small part of them escape to the air. In ray tracing program, we confine the sources to a pixel area $\sim 3 \times 3\, mm^2$. Actually the calculated extraction will not depend on the size of pixel as well as the pixel is small enough compared to the whole OLED structure.
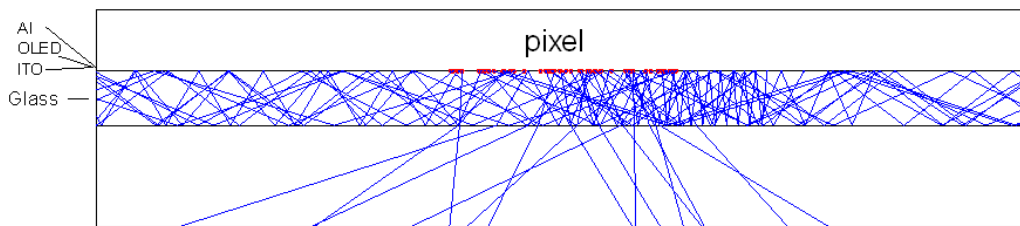
FIGURE 5-3. Ray tracing diagram for a flat OLED.

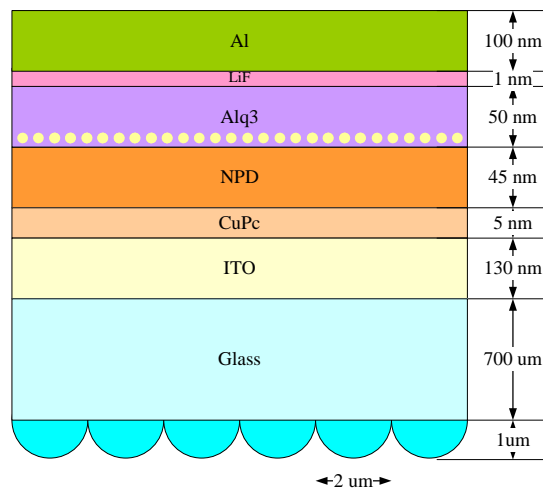## 5.4 Light extraction from an OLED with microlens array

FIGURE 5-4. Schematic of an OLED covered with a microlens array.

5.4.1   Infinite large microlens array.

A microlens-covered OLED structure is shown in Fig. 5-4. The radius of microlens is set to

be $1 \mu m$. The pitch is $2 \mu m$, which means there is no spacing between adjacent microlens.

We again assume a pixel area of $\sim 3 \times 3\, mm^2$. Then we assume an infinite large area of

microlens array. Ray tracing simulation indicates that this configuration would yield a

39.3% extraction, i.e. $\sim 150\%$ outcoupling enhancement at $525\, nm$.
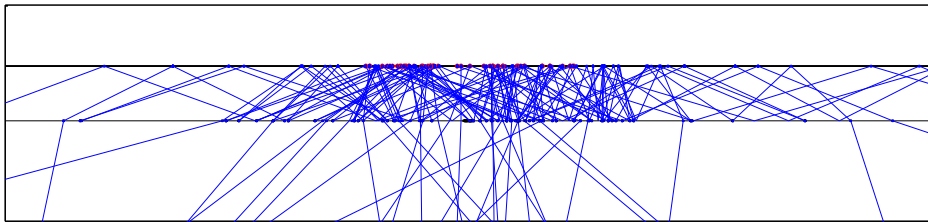

FIGURE 5-5. Ray tracing diagram for an OLED covered with a microlens array.

We plot a ray tracing diagram for 50 rays in Fig. 5-5. By comparing Fig. 5-5 with Fig. 5-3, it can be seen that more rays are extracted when glass is covered with microlens array. It is interesting to notice that some rays escape via microlens that are located not directly under the pixel or even far away from the pixel. As a result, the light trapped in glass becomes less and less as it propagates along the glass away from the pixel since some light escapes through microlens on the way. However, for a flat OLED with no microlens array, most extracted light is confined to an area directly under the pixel. This finding suggests that a microlens array significantly larger than the pixel size is preferred to extract the guided light trapped in glass.

5.4.2   A finite area of microlens array.

From the above ray tracing simulation, we know that a microlens array can help the outcoupling of the light trapped in glass. We also know that the larger area covered by microlens, the more the trapped light escape. A natural question is: how big an area should the microlens array cover to extract most of the trapped light?

To answer this question, we gradually increase the area covered by microlens from $3 \times 3\ mm^2$ to $25 \times 25\ mm^2$ in ray tracing simulation. The dependence of out-coupling enhancement on the size of microlens is plotted in Fig. 5-6. As shown in the plot, the extraction is enhanced $\sim 30\%$ if the microlens only covers the pixel. The enhancement can be increased to $\sim 80\%$ if the microlens array is $5 \times 5\ mm^2$ and $\sim 130\%$ with $15 \times 15\ mm^2$. After that, the enhancement will not increase much even if we increase the size of microlens array. As reported in the last section, the maximum enhancement that can be achieved is $\sim 150\%$ with an infinite large microlens array.
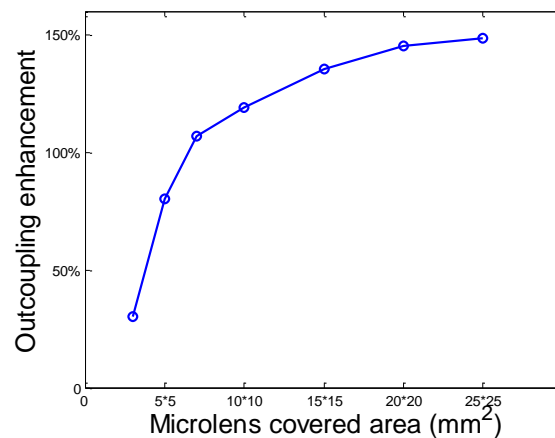

FIGURE 5-6. Dependence of out-coupling enhancement on the size of microlens.

5.4.3   Dependence on thickness of glass substrate.

When microlens array only covers a fixed area, the enhancement of light extraction is dependent on the thickness of glass substrate. We expect the light bounce forth and back between the microlens and the upper surface of OLED for more times with a thin glass than with a thick one. For example, let's check Fig. 5-7. The beam in Fig. 5-7(a) bounces on microlens for twice before it goes out of microlens range. However, if we double the thickness of glass, it bounces only once on microlens. Each time it reaches a microlens, it has a chance to escape. So the probability of the beam to escape in the configuration in Fig. 5-7(a) is larger than in (b).
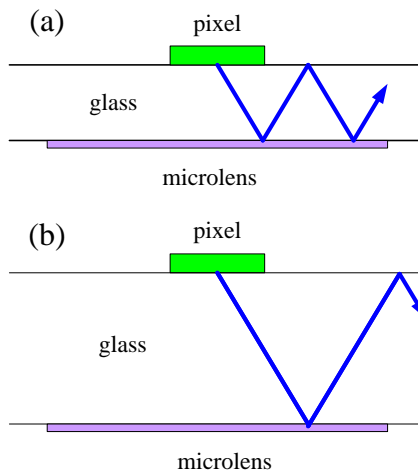

FIGURE 5-7. An OLED embossed with fixed area of microlens array and

(a) a thin glass substrate, (b) a thick glass substrate.

We simulate an OLED with fixed pixel size $3 \times 3 \, mm^2$ and fixed microlens area $6 \times 6 \, mm^2$, but with different thickness of glass substrate. The ray tracing results are summarized in Fig. 5-8, in which we plot dependence of the out-coupling enhancement on thickness of glass. As

expected, the out-coupling enhancement goes down as the ITO-coated glass substrate goes thicker (Fig. 5-8).
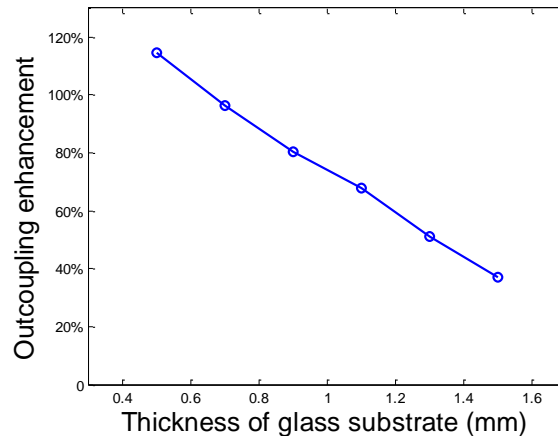

FIGURE 5-8. Dependence of out-coupling enhancement on thickness of glass substrate.

5.4.4 Dependence on integrating sphere apertures.

In section 5.3.2 and 5.3.3, we have discussed the role of microlens array area and glass thickness on extraction of trapped light. At the same time, attention should also be drawn to another important parameter in experiments: the aperture of integrating sphere for measuring the extraction efficiency. The question is, if other parameters (such as the pixel size, the microlens area and glass thickness) are fixed, how does the measured light extraction change if we use integrating spheres with different apertures?

We simulate an OLED with fixed pixel size $3 \times 3 \, mm^2$, fixed microlens area $15 \times 15 \, mm^2$, and glass substrate with fixed thickness of $1.1 \, mm$. However, we only count the out-coupling beams in a confined aperture. In Fig. 5-9, we plot the out-coupling enhancement

v.s. integrating sphere aperture diameter d. From this plot, we can see that the integrating sphere needs to be big enough ($d \geq 10\,mm$) to collect most of the extracted light. If we use an integrating sphere of which the size is comparable to the pixel, the measured extraction of light should be dramatically underestimated.
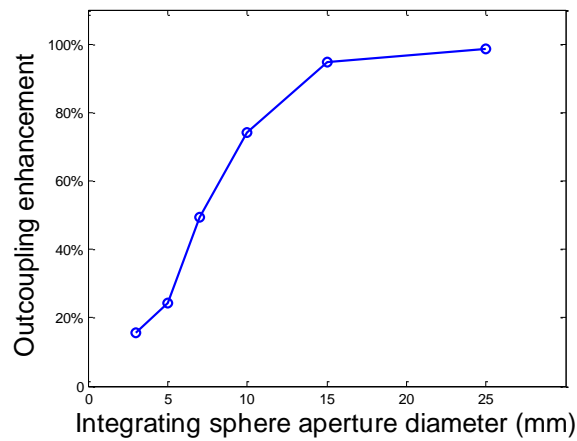

FIGURE 5-9. Extraction efficiency enhancement v.s. integrating sphere aperture diameter.

5.4.5   Profiles of extracted light at the surface of glass

If we record the position and intensity of each beam when it escapes to the air from glass or microlens, we can obtain the field intensity distribution at the top surface of the glass substrate with or without microlens array. In Fig. 5-10, we plot the field intensity distribution of the exit light for 4 cases: (a) a flat glass substrate which is $0.7\,mm$ thick, (b) a $0.7\,mm$ thick glass substrate embossed with an infinite microlens array, (c) a $1.1\,mm$ thick glass substrate embossed with an infinite microlens array, and (d) a $0.7\,mm$ thick glass substrate embossed with a $3 \times 3\,mm^2$ microlens array. The pixel is $3 \times 3\,mm^2$ in all cases as before.

(a) Glass=0.7mm. Flat   (b) Glass=0.7mm. Inf microlens

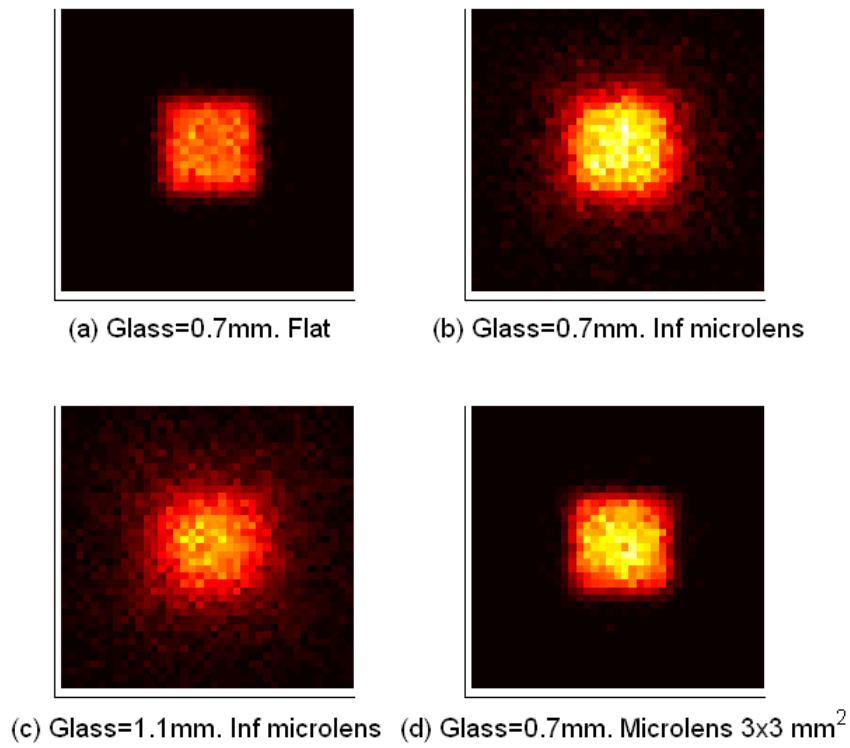(c) Glass=1.1mm. Inf microlens   (d) Glass=0.7mm. Microlens 3x3 mm^2

FIGURE 5-10. Field intensity distribution of exit light.

From Fig. 5-10, we see that the microlens array does enhance the light extraction [compare Fig. 5-10(b)-(d) to Fig. 5-10(a)]. When the microlens array covers about the same area as the pixel, the exit light is enhanced [Fig. 5-10(d)]. However, if a much larger microlens array is used, much more glass-guided light can be extracted [Fig. 5-10(b)]. At the same time, we recognize an image blurring. As glass substrate goes thicker, this blurring is even remarkable [Fig. 5-10(c)]. A red hue can be clearly noticed even at the edge of the black square area.

An OLED device can be desired for both display and lighting. Displays often require a high image resolution. As we have seen, imprinting a microlens array on substrate causes an image blurring, while extracting more light. From this point of view, there is a trade-off for microlens enhanced OLED display. However, for pure lighting purpose, there is not such a

trade-off. We can use a microlens array that is significantly larger than the OLED pixel to extract most of that waveguided light into the front direction.

5.4.6   Multiple pixels

We present the last numerical example of ray-tracing method. We consider a case of multiple pixels covered by a large microlens array. It is interesting to check what the out-coupled light look like. The glass substrate is $0.7\,mm$ thick, and there are 9 $2 \times 2\,mm^2$ pixels. The spacing between neighbor pixels is $2\,mm$. The substrate is embossed with a $20 \times 20\,mm^2$ microlens array.

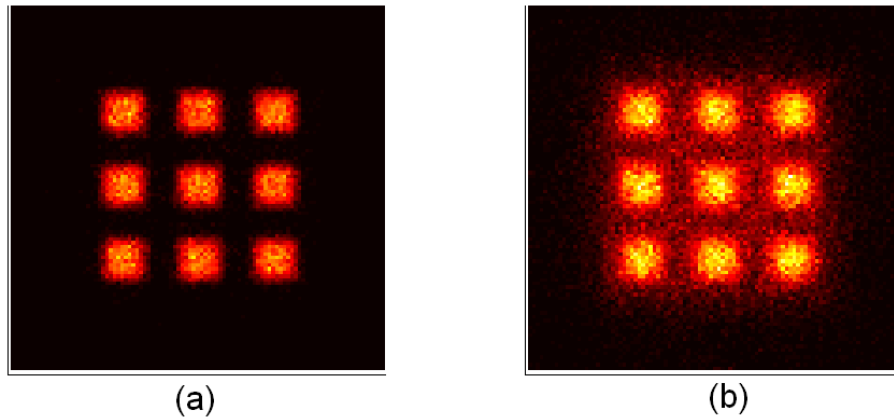FIGURE 5-11. Intensity of out-coupled light for 9 2*2 mm2 pixels with (a) a flat glass substrate, and (b) a glass substrate imprinted with a 20*20 mm2 microlens array.

We plot the exit light intensity in Fig. 5-11. Compared to the case of no microlens array, it can be seen apparently that more light exit. Not only does more light exit under pixels, but also considerable light exit in regions which are not directly under pixels [Fig. 5-11(b)]. As a result, the total area (the big square) is lightened.

5.5   Simulation and experiment

In section 5.3, we theoretically investigate the enhancement in the emission of OLEDs in the forward direction using a microlens array. The simulation is done by a statistic ray-tracing method. In this section, we are going to simulate the exact device in experiments, and compare the simulation results with the experimental measurements.

In laboratory, the microlens arrays are fabricated by crossed laser beams interference patterning and soft lithography imprinting. Some details of fabrication process are listed in the appendix after this chapter. The $2\,\mu m$-pitch square microlens array is embossed on the blank side of a $1.1\,mm$ thick ITO-coated glass. The patterned microlens array is of $15 \times 15\,mm^2$, significantly larger than the $3 \times 3\,mm^2$ OLED pixels. The SEM image of the 2-D patterns of photoresist [Fig. 5-12(a) in Appendix] suggests that the microlens is not an ideal semi-sphere. Instead it is more like a semi-ellipsoid with $1.2\,\mu m$ height and $1.6\,\mu m$ diameter.

We simulate the OLED device with parameters same as in experiments. The simulation results and experimental measurements are summarized in Table 5.1. We also include the simulation results for different values of the microlens array area and glass thickness in Table 5.1. The simulations show that, if the glass thickness decreases from 1.1 to $0.7\,mm$, and microlens area increases from 15×15 to $25 \times 25\,mm^2$, the calculated efficiency enhancement increases from 97% to 140%.

Table 5-1. (a)–(c) calculated and (d) experimental extraction efficiency enhancements with various microlens array areas, glass thickness, and integrating sphere apertures.

Integrating sphere aperture diameter d (mm)	5	10	25
(a) 15x15 mm^2 microlens array, 1.1 mm thick glass (calc.)	21%	73%	97%
(b) 25x25 mm^2 microlens array, 1.1 mm thick glass (calc.)	23%	75%	121%
(c) 25x25 mm^2 microlens array, 0.7 mm thick glass (calc.)	48%	96%	140%
(d) 15x15 mm^2 microlens array, 1.1 mm thick glass (exp.)	18%	54%	92%

5.6   Discussions and summary

In this chapter we use a statistic ray-tracing method to simulate an OLED device. A uniform microlens array is embossed on the blank glass side of an ITO-coated glass, to enhance light extraction. Although the pitch of the microlens array is only $2\,\mu m$, not significantly larger than the wavelength of $525\,nm$, a previous work[9] by Y. Sun and S. R. Forrest shows that a 3-D ray tracing method is able to simulate this microlens structure accurately. A 3-D finite difference time domain method (FDTD) can also be used for simulation, but it is much more time consuming than ray tracing. We do not use transfer matrix method (TMM) since TMM assumes a periodic boundary condition, which is not applicable for our device.

We investigate several factors that have impact on the measured enhancement of light extraction. These factors are the thickness of ITO-coated glass, the microlens array area, and integrating sphere aperture. We show the calculated optical field intensity of the out-coupling light from OLED. The calculated enhancements are compared to experimental measurements and they agree well.
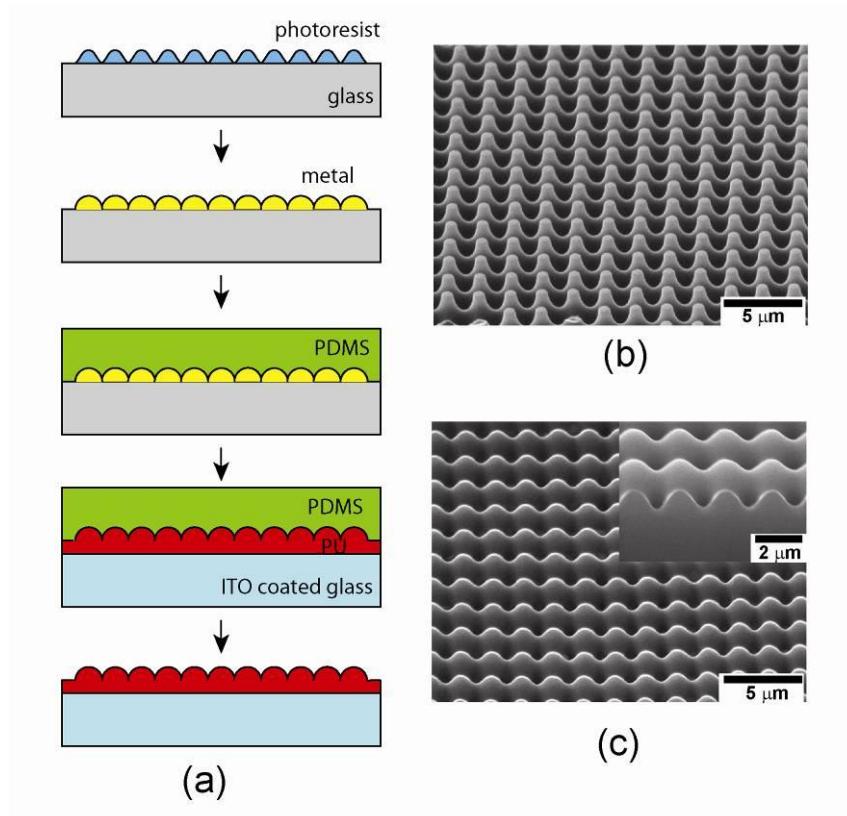
Appendix: Microlens and OLED fabrication

Figure 5-12. (a) SEM image of the 2D patterns of photoresist, (b) Schematic of microlens fabrica-tion on glass. A master template is covered with PDMS. The PDMS is removed from the master and filled with PU and then pressed against another glass substrate. The PDMS is lifted off and the PU microlens array remains on the glass substrate. (c) the resulting PU microlens array.

The microlens array was fabricated using soft photolithography. A master stamp was first fabricated using a photoresist. Two-beam laser holography was used for patterning the photoresist. A single exposure creates a 1-D pattern, and a 2-D pattern is achieved by a second exposure after rotating the sample by 90°. After the master stamp was ready, polydimethylsiloxane (PDMS) was poured onto the master stamp, to generate a temporary

mold with the desired pattern of a spherical array. Then the microlens pattern is imprinted on an ITO-coated glass substrate by two-polymer microtransfer molding[10].

Figure 5-12(a) shows the SEM image of the photoresist pattern after developing. Figure 5-12(b) shows the fabrication process of the microlenses on the glass surface and Figure 5-12(c) is an SEM image of the microlens array. This array covers only a portion of the ITO/glass.

OLED pixels were fabricated on the ITO side of the glass. The ITO was patterned and etched to form anode stripes. OLED fabrication on the ITO side of the glass is detailed elsewhere[11,12]. Measurements were performed by placing the device on the opening of an integrating sphere with 5, 10, 25 mm diameter opening.

Figure 5-13(a) shows two energized green tris (quinolinolate) Al (Alq3)-based OLED pixels lit at the same current density. The left pixel is under a microlens array. Note the much larger size of the microlens array in comparison to the OLED pixels. As seen, the left pixel appears much brighter, but the light around them is diffuse. The pixel on the right appears much sharper with a defined square shape. Figure 5-13(b) shows the EL spectra of the OLEDs, taken with only one pixel energized and with different aperture diameter d_a of the integrating sphere. It can be seen that the EL intensity from the OLED pixel under the microlens array increases with increasing d_a, whereas it is unaffected by d_a for the reference pixels. As d_a increases, more of the light extracted by the microlenses from outside the pixel area is collected, resulting in increased EL intensity. When $d_a = 25\,mm$, it collects essentially all the light extracted by the microlenses and the enhancement is $\sim 100\%$. Check Ref. 12 for more details about experimental fabrication and measurements.
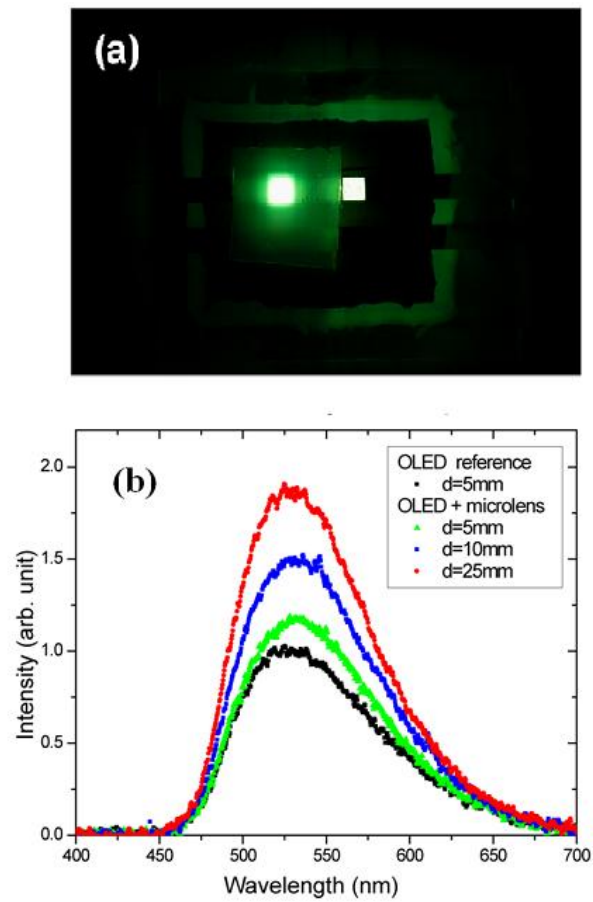
FIGURE 5-13. (a) Image of OLED with green emitting Alq3. The left side pixel is under a microlens array and the right one is reference pixel. (b) EL spectra of OLED with a PU microlens array measured with different apertures of an integrating sphere.

References:

1. G. Gustafsson, Y. Cao, G. M. Treacy, F. Klavetter, N. Colaneri, and A. J. Heeger, "Flexible light-emitting diodes made from soluble conducting polymers", *Nature* 357, 477 (1992).

2. D. A. Pardo, G. E. Jabbour, and N. Peyghambarian, "Applications of screen printing in the fabrication of organic light-emitting devices", *Adv. Mater.* 12, 1249 (2000).

3. N. C. Greenham, R. H. Friend, and D. C. Bradley, "Angular dependence of the emission from a conjugated polymer light-emitting diode: Implications for efficiency calculations", *Adv. Mater.* 6, 491 (1994).

4. Y. Sun and S. R. Forrest, "Enhanced light out-coupling of organic light-emitting devices using embedded low-index grids", *Nature Photonics* 2, 483 (2008).

5. J.-Q. Xi, M. F. Schubert, J. K. Kim, E. F. Schubert, M. Chen, S.-Y. Lin, W. Liu, and J. A. Smart, "Optical thin-film materials with low refractive index for broadband elimination of Fresnel reflection", *Nature Photonics* 1, 176 (2007).

6. S. Moller and S. R. Forrest, "Improved light out-coupling in organic light emitting diodes employing ordered microlens arrays", *J. Appl. Phys.* 91, 3324 (2002).

7. J. Lim, S. S. Ho, D. Y. Kim, S. H. Cho, I. T. Kim, S. H. Ham, H. Takezoe, E. H. Choi, G. S. Cho, Y. H. Seo, S. O. Kang, and B. Park, "Enhanced out-coupling factor of microcavity organic light-emitting devices with irregular microlens array", *Optics Express* 14, 6564 (2006).

8. For information about ZEMAX check their official website www.zemax.com.

9. Y. Sun and S. R. Forrest, "Organic light emitting devices with enhanced outcoupling via microlenses fabricated by imprint lithography", *J. Appl. Phys.* 100, 073106 (2006).

10. J. H. Lee, C. H. Kim, Y. S. Kim, K.M. Ho, K. P. Constant, W. Leung, C. H. Oh, "Two-polymer microtransfer molding for highly layered microstructures", *Advanced*

Materials 17, 2481 (2005).

11. L. Zou, V. Savvate'ev, J. Booher, C. H. Kim, J. Shinar, "Combinatorial fabrication and studies of intense efficient ultraviolet-violet organic light-emitting device arrays", *Appl. Phys. Lett. 79*, 2282 (2001).

12. J. M. Park, Z. Gan, R. Liu, W. Y. Leung, Z. Ye, K. Constant, J. Shinar, R. Shinar, and K. M. Ho, "Soft lithography microlens fabrication for enhanced organic light emitting diode light extraction", to be submitted.

Chapter 6. Design of Nanoscale Metallic Structures as Transparent Electrodes for Organic Photovoltaic Cells

We theoretically investigate the optical absorption in organic photovoltaic cells in which a metallic grating replaces indium tin oxide (ITO) as transparent electrode. Numerical simulations show that the grating produces broadband optical absorption enhancement. By tuning the structure parameters, the overall absorption in the organic layers can be largely enhanced.

6.1 History of solar technologies

The earliest development of solar technologies started in the 1860s, when people expect that coal would soon become scarce. However in the early 20th century, development of solar technologies stagnated in the face of the increasing availability and utility of coal and petroleum. It is not until the recent decades that renewed attention was brought to developing solar technologies by energy crisis. Solar powered electrical generation includes heat engines and photovoltaics.

A solar cell, or photovoltaic cell, is a solid state device that converts the energy of sunlight directly into electricity by the photovoltaic effect. There are currently three different types of solar cells in production in today's market place. They are the monocrystalline, polycrystalline and amorphous. Other materials presently used include cadmium telluride, copper indium selenide / sulfide, organic dyes, and organic polymers[1]. In this chapter, we are going to study organic photovoltaic cells, or OPV cells.

OPV cells are a relatively novel technology. These cells can be processed from solution, hence the possibility of a simple roll-to-roll printing process, which allows inexpensive, large

scale production. They are different from inorganic semiconductor solar cells, which use a PN junction to separate the electrons and holes. The active region of an organic solar cell consists of two materials, one acting as an electron donor while the other as an acceptor. When a photon is absorbed, an electron-hole pair is created, and then this pair is relaxed remaining bound known as an exciton. The electron and the hole are separated when the exciton diffuses to the donor-acceptor interface.

6.2   A replacement for ITO electrode

In an OPV cell, an indium tin oxide (ITO) front electrode is usually used (also in inorganic devices and some electric lighting devices like LEDs). Indium is a scarce resource, which has made the long-term availability and cost unreliable. Another drawback of ITO electrode is its brittle nature[2]. We expect a new design a OPV cell transparent electrode to have (1) high sheet conductivity; (2) high transparency in visible range; (3) low cost; (4) flexible and good adhesion.

In this chapter, we propose a nanoscale metallic structure as a promising replacement of ITO electrode. This novel technique is based on the two polymer micro-transfer molding (2-P µTM, see Ref. 3) to fabricate one dimensional (1-D) high or low aspect ratio nanoscale metallic structure. Glancing angle metal deposition and physical argon ion milling (etching) techniques were also employed in processing. Some details of fabrication are listed in the appendix at the end of this chapter. Experimental measurements show that this metallic structure has high sheet conductivity (R<10Ω/sq) and high transparency in visible range (T>80%). It is easy to fabricate and low cost. It should be a good replacement for ITO electrode in every aspect.
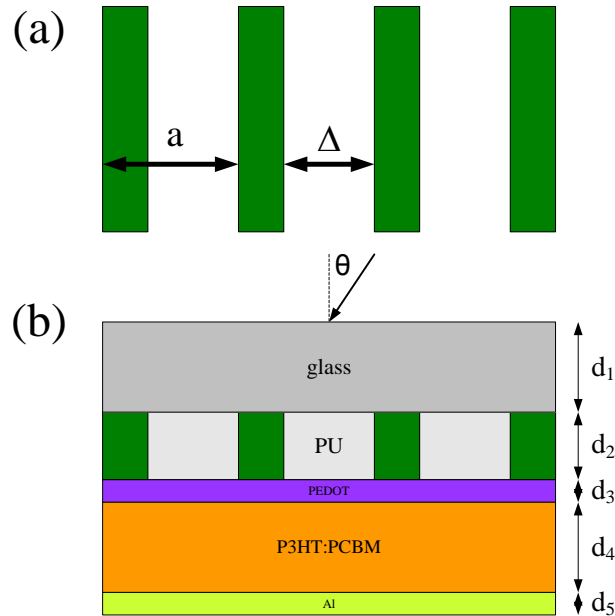
FIGURE 6-1. (a) Top view of a 1-D metal grating with period a and slit size Δ. (b) Side view of a P3HT:PCBM based OPV cell, with the metal grating replacing ITO as the electrode.

Beyond the conductivity and transparency, we also want to optimize the system to get a strong resonance field in the underneath OPV cell to largely enhance the absorption of photons. Before us, several designs have been proposed using plasmon resonance to enhance optical absorption. These works include using random metal nanohole films[4], depositing metal nanoparticles on a thin metal layer[5], growing ITO–Ag–ITO multilayer electrodes[6] and etc. In this chapter we propose a new structure shown in Figure 1, and we show that this metal grating structure produces broadband optical absorption enhancement. With optimizing grating parameters, the absorption can be enhanced by about 140% in the active region of poly(3-hexylthiophene) and [6,6]-phenyl C61-butyric acid methylester (P3HT:PCBM[10]) blend compared to an OPV cell with a 100 nm ITO.

6.3   Numerical modeling and design

A schematic of the high or low aspect ratio nanoscale metallic structure we propose is presented in Fig. 6-1. An OPV cell based on P3HT:PCBM blend as the active layer of thickness d_4, with a thin conducting film of thickness d_3 of poly (3,4-ethylenedioxythiophene) doped with poly(styrenesulfonate) (PEDOT:PSS, Clevios P VP Al 4083), sandwiched between a metal grating of thickness d_2 and an aluminum electrode of thickness d_5, is placed against a glass substrate of thickness d_1 [see Fig. 6-1(b)]. The 1-D metal grating has period a and the width of polyurethane (PU) block that filled in between silver walls is Δ. Define filling ratio of metal: $f = (a - \Delta)/a$. We are going to optimize these parameters to enhance the optical absorption in P3HT:PCBM layer for the wavelength range of $480\,nm \sim 620\,nm$.

The numerical method we take to model the optical properties of the system is plane-wave-based transfer matrix method (TMM)[7-9]. TMM is chosen because of the following reasons:

(1) Using TMM saves a lot of compute time. Basically TMM transfers a 3-D layer by layer structure to a 2-D problem. Thus the compute time is largely reduced. (2) TMM works great for metallic structure. Usually many more plane waves are needed to avoid convergence problem for a system that contains metal. For a 3-D system, the number of plane waves that are needed is often beyond the memory, or the computing process becomes extremely slow. However, since TMM transfer a 3-D problem to a 2-D one, many less plane waves are needed without raising convergence problem. (3) TMM is a frequency domain method and reflection / transmission / absorption spectra can be calculated quickly and directly. Since the whole system is to be optimized over a large wavelength range, spectra calculation is essential for this design.

6.3.1   Simplification of model

In this chapter, only linear absorption is considered in numerical simulation, and the following simplification is applied to the construction of OPV cell shown in Fig. 6-1.

(1) In the following spectra calculation, the PEDOT:PSS film is neglected ($d_3 = 0$, as shown in Fig. 6-2) unless otherwise specified since it is thin ($30 \sim 50 \, nm$) compared to other layers. Later in this chapter the PEDOT:PSS will be included, and we will show that this layer has little effect in the overall design.
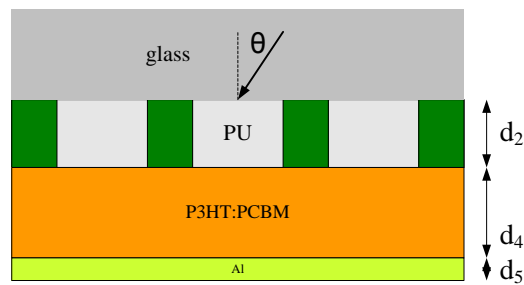

FIGURE 6-2. Schematic of a simplified OPV cell, with PEDOT:PSS removed and

glass to be infinite thick.

(2) The thickness of glass substrate is set to be infinite ($d_1 = +\infty$). That is, the whole structure is deposited on a semi-infinite thick glass substrate, and light is incident from the glass (see Fig. 6-2). The purpose of doing this is to remove the interference pattern in spectra due to interference of light reflected at the upper and lower surfaces of glass substrate. To illustrate this, we consider the absorption spectrum plotted (blue line) in Fig. 6-3 when glass substrate is $700 \, \mu m$ thick. Other parameters: $a = 500 \, nm$, $f = 0.06$, $d_2 = 500 \, nm$,

$d_4 = 150\ nm$, $d_5 = 800\ nm$, silver grating, the incident light is S-polarized (TE), and normal incidence ($\theta = 0°$) is considered, and 41 plane waves are used. There is a dramatic fluctuation in spectrum due to interference. To remove the fluctuation, we need to remove the air-glass interface. The absorption spectrum is plotted in red thick line in Fig. 6-3 when the glass substrate is infinite thick. The absorption is calculated as the ratio of energy being absorbed in P3HT:PCBM to the energy of incident light. This smoothed spectrum without interference pattern does characterize the real absorption in the active layer.
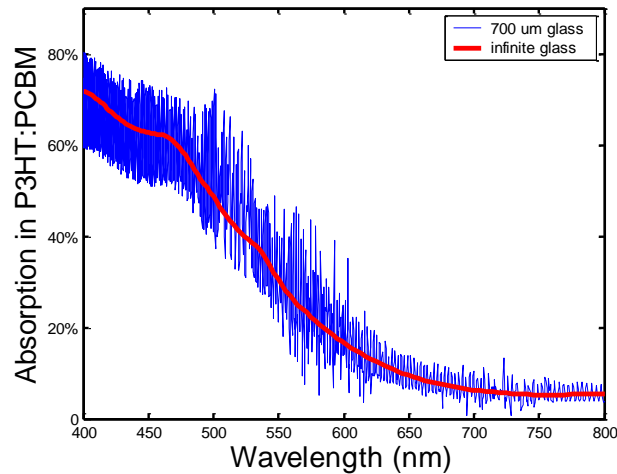

FIGURE 6-3. Absorption spectrum in P3HT:PCBM when glass is 700 um thick (blue) and infinite thick (red).

6.3.2   Metal grating: gold, silver, or aluminum?

There are several candidates to be used in the metal grating like gold, silver, and aluminum. It is to be decided which metal should be taken in the OPV cells. To examine the effect of different metal grating on the optical absorption, we plot the absorption spectrum for the

three metal gratings in Fig. 6-4. The parameters: $a = 360\,nm$, $f = 0.12$, $d_2 = 300\,nm$, $d_4 = 160\,nm$, $d_5 = 800\,nm$, and normal incidence is considered.
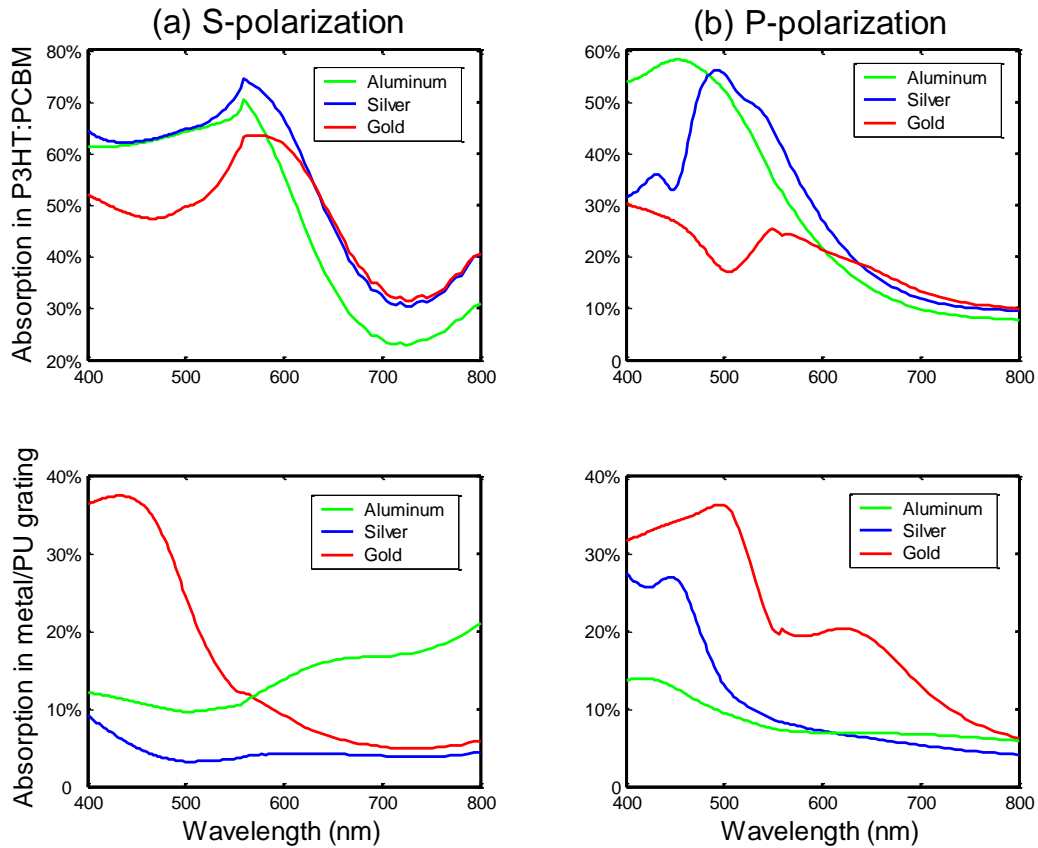

FIGURE 6-4. Absorption in P3HT:PCBM and metal/PU grating for Aluminum (green), silver (blue), and gold (green) based constructions.

It can be seen that silver grating has an overall lowest absorption, while bringing a strongest absorption in the P3HT:PCBM layer for the interested wavelength range $480 \sim 620\,nm$. Gold is highly absorptive for short wavelengths. Although aluminum is less absorptive than silver for P-polarized (TM) light, its overall performance is worse than silver, i.e., it brings

less absorption in the active layer than silver (high optical absorption in P3HT:PCBM is preferred to enhance the current produced by absorption of photons). In the following we will lock in silver in all calculations.

6.3.3 Absorption spectrum

In above sections, we have simplified the model and chosen silver grating as a replacement of ITO electrode. Next optical design is to be performed to maximize the optical field intensities in the organic layer to amplify the current produced by absorbed photons.

An enhanced optical field in the OPV cell is usually accompanied with a peak in the absorption spectrum. So first we look for these peaks by adjusting the system parameters a, d_2, d_4 and Δ. We set $d_1 = +\infty$ to remove the air-glass interface, and $d_3 = 0$ to exclude the thin PEDOT:PSS film. We set the thickness of aluminum d_5 to be thick enough to absorb all the incoming light, with $d_5 = 800 \, nm$ (in experiments usually $d_5 \sim 100 \, nm$).

Secondly we move the peak(s) to the interested wavelength range $480 \sim 620 \, nm$ by carefully adjusting those parameters. This is not easy since we want the peaks appear in the right wavelength range for both two polarizations. By adjusting period a we can usually change the position of a peak in spectrum for S-polarized light. But if for one polarization a peak appears $480 \sim 620 \, nm$, while for the other polarization a peak appears out of range, and you want to adjust parameters to get the second peak into the interested range, what possibly happens is that the first peak will move too, often out of the interested range.
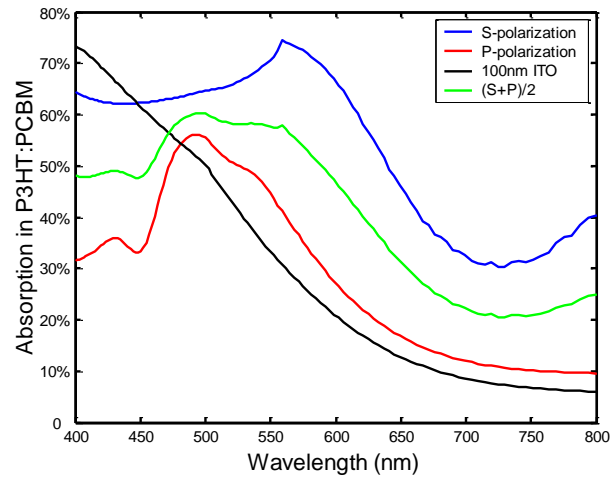
FIGURE 6-5. Absorption spectra in P3HT:PCBM for S-polarization (blue), P-polarization (red),

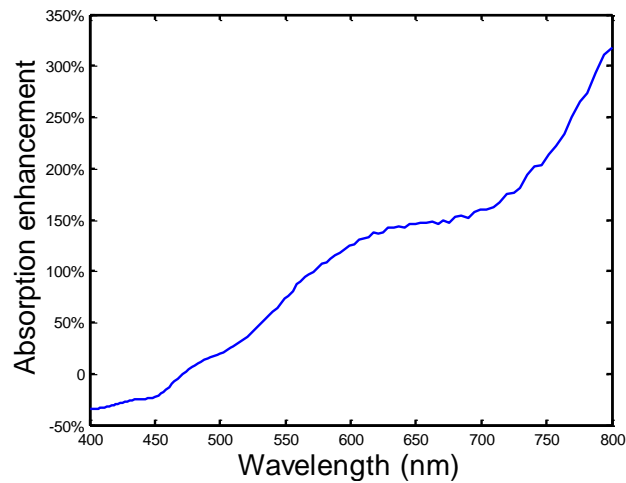average of the two (green), and 100 nm ITO (black).

FIGURE 6-6. Enhancement of optical absorption in P3HT:PCBM.

As far as we try, a peak for S-polarization appears around $559 \, nm$ (blue line in Fig. 6-5),

and another one for P-polarization around $493 \, nm$ (red line). Averaging two polarizations,

these two peaks give a plateau from $470\,nm$ to $570\,nm$ (green line). The parameters $a = 360\,nm$, $f = 0.12$, $d_2 = 300\,nm$, $d_4 = 160\,nm$, $d_5 = 800\,nm$, and normal incidence is considered. As a comparison, the absorption spectrum is also plotted when a 100 nm thick ITO glass acts as the electrode with other parameters same. The enhancement of optical absorption in P3HT:PCBM, defined as $\dfrac{absorption\ with\ grating}{absorption\ with\ ITO} - 1$, is plotted in Fig. 6-6. In the interested wavelength range of $480 \sim 620\,nm$, the enhancement monotonically increases from 7% to 137%.

6.3.4 Electric field distribution

When only the linear absorption is considered, the absorption is proportional to the light intensity in that each layer[11]: $Absorption_{P3HT:PCBM} \propto \int_{P3HT:PCBM} \left| \bar{E} \right|^2 d\bar{r}$. The field pattern is interesting to explore, to tell how the optical field in the organic layer is enhanced and what mechanism is responsible for this enhancement.

The electric field distribution at the resonant peaks in Fig. 6-5 is plotted in Fig. 6-7 (a) for S-polarization at $559\,nm$, and in (b) for P-polarization at $493\,nm$. From Fig. 6-7 (a), it can be seen that the strongest field is in the middle of the active layer, which is preferred, since higher optical absorption in the middle of the active layer will produce stronger electric current. However, for P-polarization, a surface wave is excited. The optical field is dramatically enhanced at the interface of PU/silver grating and P3HT:PCBM [Fig. 6-7(b)]. In Fig. 6-7(b), the field profile is plotted using the same color map as in Fig. 6-7(a) (to allow the two profiles plotted with the same scale). Actually the peak of field in Fig. 6-7(b) is much stronger than in that in Fig. 6-7(a) by a factor of 10 (see Fig. 6-7(c) and (d) for a real
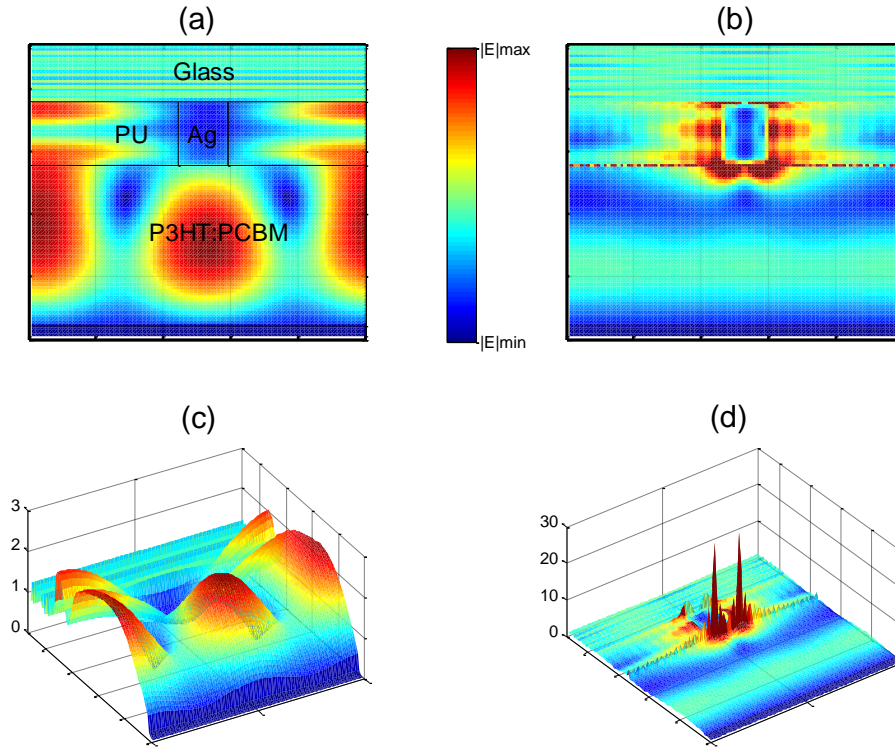
comparison).

FIGURE 6-7. Electric field distribution for (a) (c) S-polarization at 559 nm;

(b) (d) P-polarization at 493 nm.

6.3.5 Mechanism of field enhancement in P3HT:PCBM

6.3.5.1 S-polarization

By carefully examining the electric field distribution shown in Fig. 6-7(a), we notes that the silver grating produces a field pattern in the underneath P3HT:PCBM similar to a cavity resonant mode. Any adjacent two silver walls act as a pair of mirrors. They reflect light and

produce resonant fields in PU between them and also in the underneath P3HT:PCBM layer. So it is expected that the peak in the spectrum due to cavity resonance should be sensitive to the period a. As a verification, the absorption spectra are plotted for different a's in Fig. 6-8(a) with other parameters fixed. When a is shortened to $320\,nm$, the peak in the spectrum is weakened and red-shifted. When a is elongated to $400\,nm$, the resonant peak is disappeared.
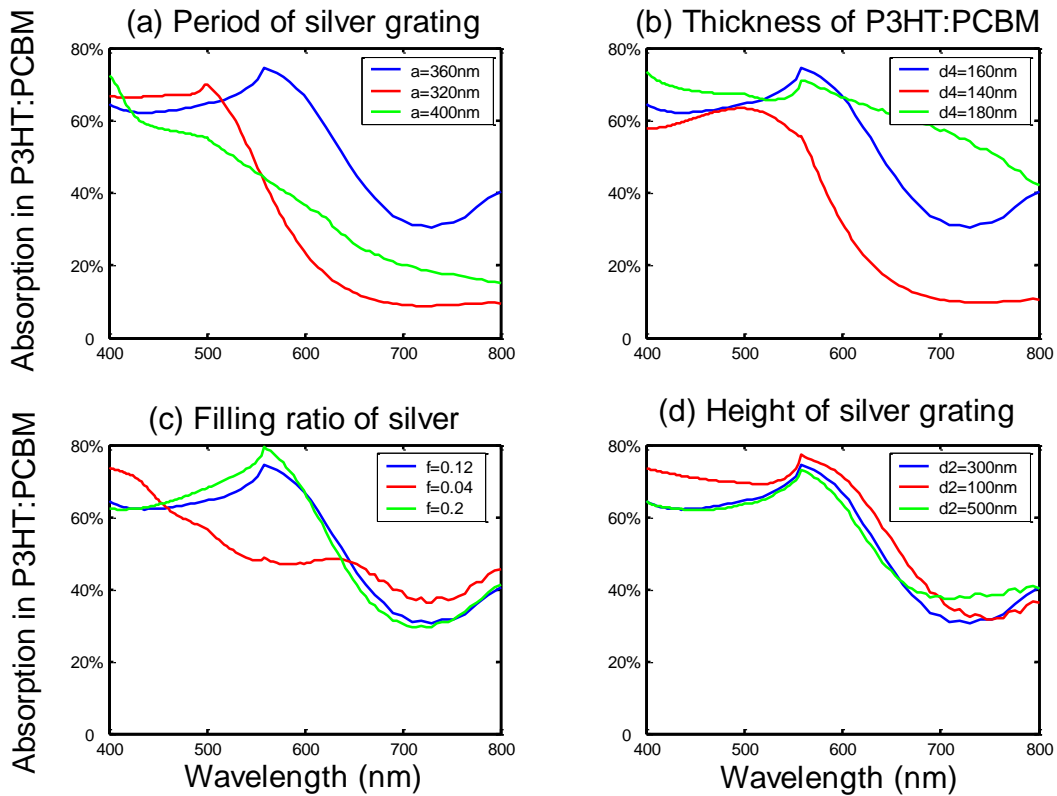

FIGURE 6-8. Effect of parameters on the absorption spectra for S-polarized light with varied (a) period, (b) thickness of P3HT:PCBM, (c) filling ratio of silver grating, and (d) height of silver grating.

The absorption spectra for different thickness of P3HT:PCBM are plotted in Fig. 6-8(b) with other parameters fixed. Since the peak in the spectrum is produced by a resonance in

P3HT:PCBM as a cavity, it should also be sensitive to the thickness of the cavity. The plot in Fig. 6-8(b) illustrates this. Although the position of the peak keeps fixed at $559\,nm$, which is decided by a, the strength of the resonance is strongly determined by the thickness of the organic layer.

Then we check the influences of the thickness of silver walls (described by filling ratio f) and the height of silver grating (d_2). Since the resonance is produced by the reflection from adjacent silver walls, it is expected that thicker silver walls will induce stronger resonance, which is confirmed by Fig. 6-8(c). We also note that when silver wall is not thick enough, the resonant field cannot be excited [see red line in Fig. 6-8(c), $f = 0.04$, the thickness of silver is $14\,nm$, and the skin depth of silver at visible range is around $13\,nm$].

The effect of height of silver grating is plotted in Fig. 6-8(d). The resonance is not sensitive to the height of silver grating (d_2). A thinner d_2 gives a more transparent electrode, and more absorption in the active layer. However, d_2 cannot be too small to allow high sheet conductivity of silver/PU grating. So in experiments, we often set d_2 to be $\geq 300\,nm$.

6.3.5.2 P-polarization

For P-polarized light, the silver grating excites a surface plasmonic wave as shown in Fig. 6-7(b) and (d). Enhancement of transmission through subwavelength holes in thin metal films has been widely studied[4,12]. The basic mechanism is (1) an incident photon couples to a surface plasmon (SP) on one side of a nanohole film, (2) the SP propagates within the hold to the other side of the film, (3) the SP is converted back to a photon and radiated into the

far-field.

However, our silver/PU grating structure is different from those nanohole films. In our structure, metal has a very small filling ratio, in contrast to the nanohole films. It is a kind of "inverted" structure. However, it shares some characteristic of SP studied in Ref. 4, 12. The SP mode is only found for P-polarization (with magnetic field H parallel to the grating).
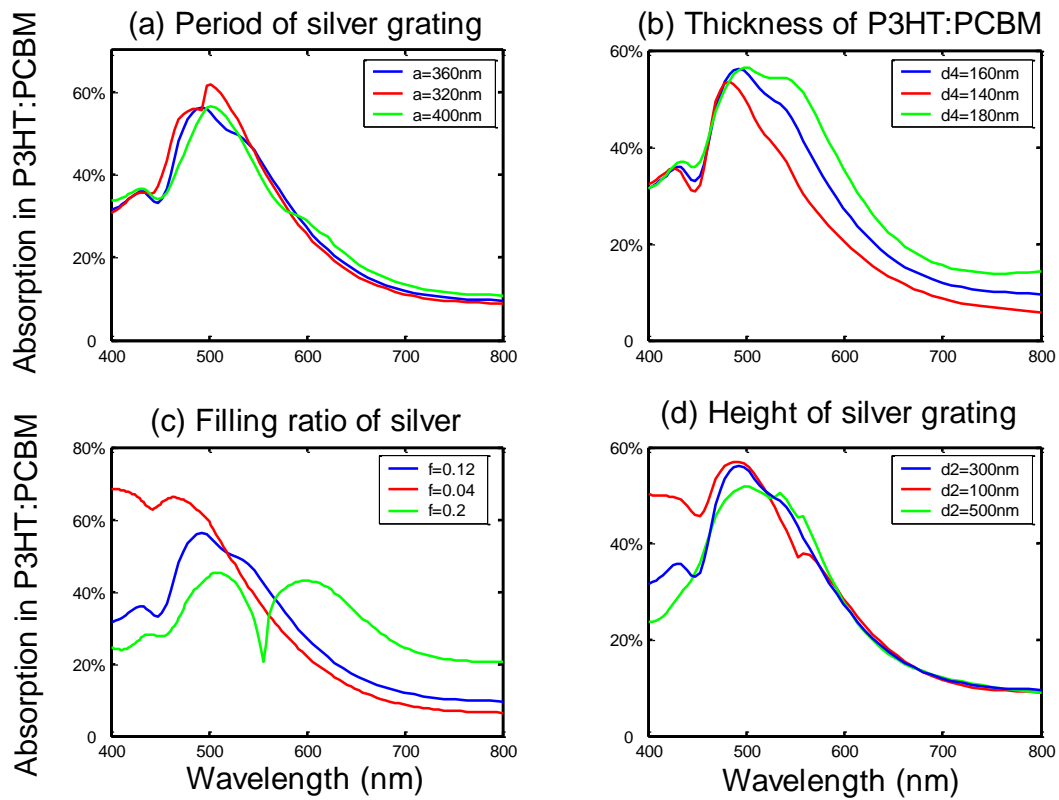

FIGURE 6-9. Effect of parameters on the absorption spectra for P-polarized light with varied (a) period, (b) thickness of P3HT:PCBM, (c) filling ratio of silver grating, and (d) height of silver grating.

The absorption spectra in Fig. 6-9 describe some characteristic of the SP mode. First, since SP is excited along the surface of the metal, the SP mode is not sensitive to the period a,

which is confirmed by the spectra in Fig. 6-9(a). This property for P-polarization is very different from S-polarization. Remember in previous discussion, the peak for S-polarization is due to cavity resonance, so it is very sensitive to a.

Next, we investigate the effect of P3HT:PCBM of different thickness. The EM field is mostly enhanced at the interface of metal/PU grating and P3HT:PCBM, where the SP is converted back to a photon and radiated into the far-field. So we expect that changing the thickness of the organic layer would not largely change the spectrum pattern (since a big part of absorption is at the grating/organic interface). However, the thicker the organic layer is, the more it should absorb the far-field radiation by SP-photon [see Fig. 6-9(b)].

The thickness of silver walls seems to have a big influence on the absorption pattern [Fig. 6-9(c)]. A possible reason is that the two SPs at the left and right surface of the metal interfere with each other when the silver wall is thin. So the distance between the two surfaces is important on deciding the absorption pattern.

The absorption spectrum is not sensitive to the height of silver/PU grating [Fig. 9(d)], except at short wavelengths. For short wavelengths, a taller silver/PU grating absorbs more incoming light so reduces the light that is transmitted to and absorbed in the organic layer. The same trends is also seen in Fig. 6-9(c) when the filling ratio gets bigger at short wavelengths.

6.3.6   Oblique incidence

All of above simulations are based on normal incidence of light, since we can always turn a solar cell to face the sun with a tracing system. However, the effect of oblique incidence is also interesting to inspect. The absorption spectra for oblique incidence of light are plotted in

solid lines in Fig. 6-10. The spectra are the average of S-polarization and P-polarization. The geometric parameters are the same as before. The absorption spectra of a structure with 100 nm thick ITO are also plotted as a comparison. Remember in our model, the light comes in from a semi-infinite thick glass. The corresponding incident angles in air are calculated by Snell's law and listed in the legend.
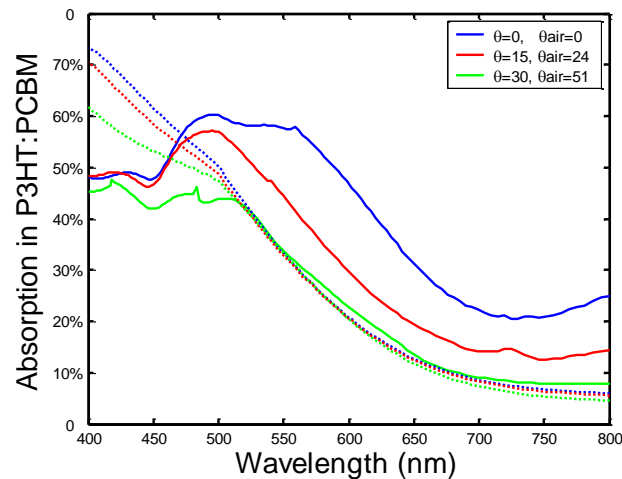

FIGURE 6-10. Absorption spectra for oblique incidence. Solid lines: silver/PU grating.

Dotted lines: 100 nm thick ITO.

From Fig. 6-10, it can be seen that at normal incidence ($\theta = 0$), the silver/PU grating outperforms ITO in the interested wavelength range $480 \sim 620\, nm$. However, as the incident angle becomes more oblique, the performance of silver grating is closer to that of ITO. It makes sense since as light is obliquely incident, the silver walls tend to shelter the incoming light, so the light that is transmitted through silver grating and absorbed by the active layer becomes less.

6.3.7   Effect of a thin PEDOT:PSS film

In the beginning, we simplified our model by neglecting the PEDOT:PSS film, since it is thin compared to other layers. Now we add this PEDOT:PSS layer in our model. The thickness of it is set to be $40\,nm$. We repeat the spectra calculation described in Sec. 6.4.3, with silver/PU grating and ITO respectively, and calculate the enhancement of absorption in the active layer. The enhancement is plotted in red line in Fig. 6-11. As a comparison, the enhancement in previous calculation with NO PEDOT:PSS film is also plotted in blue line. From Fig. 6-11, including PEDOT:PSS in simulation will weaken the enhancement a little, not much (around $10\% \sim 20\%$ less in the interested wavelength range $480 \sim 620\,nm$). This weakening is probably due to the SP mode excited for P-polarization. Since the absorption is mostly enhanced at the surface of silver, when a PEDOT:PSS film is added between silver grating and P3HT:PCBM, that highly-absorption range lies most in PEDOT:PSS, not P3HT:PCBM.
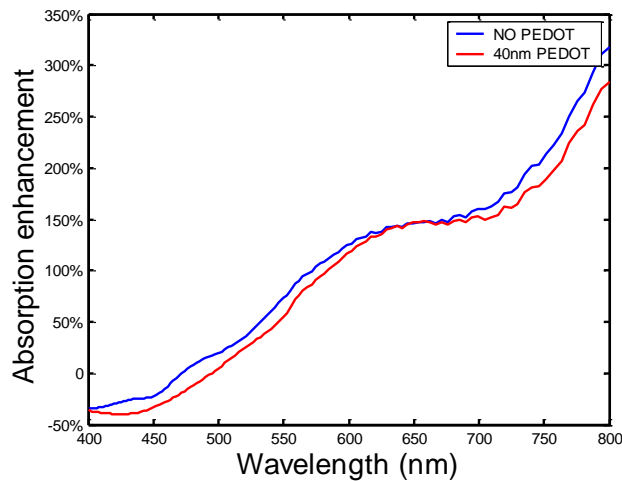

FIGURE 6-11. Enhancement of optical absorption in P3HT:PCBM compared to 100 nm ITO.

Blue: No PEDOT:PSS. Red: 40 nm thick PEDOT:PSS is considered.

6.4   Discussions

In lab, the metal/PU grating that can be fabricated now has the period $a \sim 1.2um$[13]. It can excite resonance modes only at inferred range, which can not be used in solar cell application. To excite resonance in the visible range that can be used to enhance the absorption of sun light in OPV cells, a needs to be largely reduced. In the present stage, the design described in this chapter is based on theoretical calculation. I am going to cooperate with my fellow experimentalists to carry out the design. To let calculation compatible with experiments, we also need to update the data for materials like ITO, P3HT:PCBM and PEDOT:PSS. In this chapter, we used the data from literature. However, the refractive index and extinction coefficients of these materials are not fixed. For example, ITO glasses from various commercial companies have different extinction coefficients. The extinction coefficients of P3HT:PCBM and PEDOT:PSS are also highly dependent on how they are prepared. To make theoretical results compatible with experimental ones, we need to measure the refractive index and extinction coefficients ourselves, and use these "real" data in our modeling.

6.5   Summary

In this chapter we propose a metal/PU grating structure that replaces ITO electrode. The optical absorption in the organic layer is largely improved via the enhancement of the electromagnetic field. We show that both cavity resonance mode and surface plasma mode are responsible for the field enhancement in the active layer. The mechanism that underlies the field enhancement is analyzed in details. The influence of each geometric parameter on the absorption spectra is carefully inspected and explained.

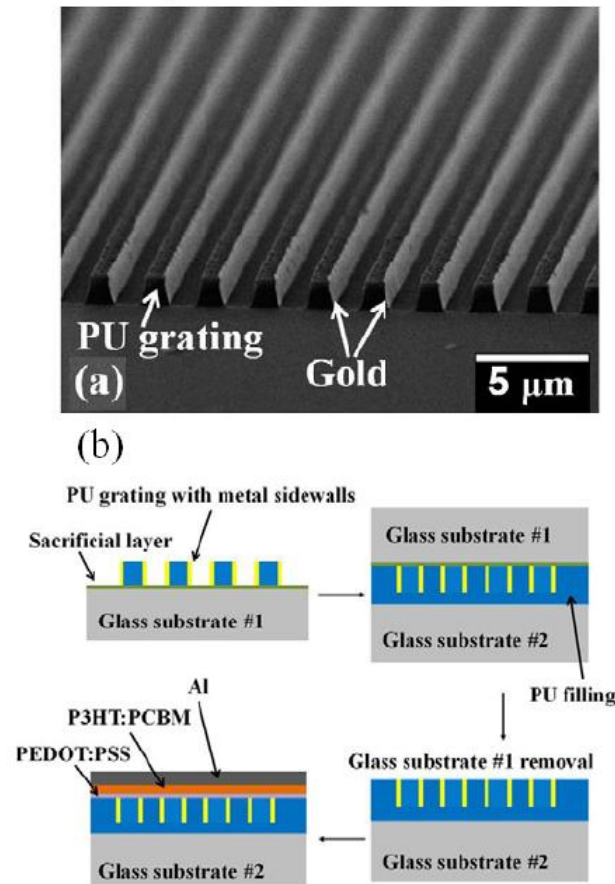# Appendix: Fabrication of a metal grating electrode based OPV cell

Figure 6-12. (a) SEM image of one-layer PU grating with 2.5 μm periodicity and 40 nm gold sidewalls.

(b) Schematics for metal grating based OPV cell fabrication.

In our lab my colleagues fabricate the metal grating electrode based OPV cells in a multi-stage process. First, a PU grating structure with a periodicity of $2.5\ \mu m$ is imprinted on glass substrate by two-polymer microtransfer molding[3]. Next, metal sidewalls are thermally evaporated onto the sample via two oblique angle depositions. The sample is tilted $45°$ so one sidewall and top of the PU bars are coated (PU bars block the metal from being

deposited on the bottom of the trench). Then this step is repeated and the other sidewall is coated. In the end, argon ion milling, a physical etching technique is employed to physically remove the metal on top of PU bars. The scanning electron microscope (SEM) image of gold coated PU grating structure is shown in Fig. 6-12(a).

The above paragraph describes the fabrication of metal grating electrode. To realize an OPV cells on our metal grating electrode platform, they need to fill the open trenches with PU to provide a flat surface for organic layer deposition. A small droplet of PU prepolymer is placed on the sample to fill in the trenches, and also acts as a glue to attach a second glass substrate onto the sample. After the PU filling is cured, the sample is submerged in distilled water to dissolve the sacrificial layer, and the first glass substrate is detached. Then the OPV cell can be deposited on this structure through general process described in literature. Check Ref. 13 for more details on the fabrication process.

References:

1. Mark Z. Jacobson, "Review of Solutions to Global Warming, Air Pollution, and Energy Security", *Energy & Environmental Science* 2, 148 (2009)
2. Z. Chen, B. Cotterell, W. Wang, E. Guenther, S.-J. Chua, "A mechanical assessment of flexible opto-electronic devices", *Thin Solid Films* 394, 202 (2001).
3. J. H. Lee, C.H. Kim, Y.S. Kim, K.M. Ho, K. P. Constant, W. Leung, C. H. Oh, "Two-polymer microtransfer molding for highly layered microstructures", *Advanced Materials* 17, 2481 (2005).
4. T. H. Reilly III et al., "Surface-plasmon enhanced transparent electrodes in organic photovoltaics", *Appl. Phys. Lett.* 92, 243304 (2008); T. H. Reilly III et al., "Controlling the optical properties of plasmonic disordered nanohole silver films",

ACS NANO 4, 615 (2010)

5. S. Pillai, K. R. Catchpole, T. Trupke, and M. A. Green, "Surface plasmon enhanced silicon solar cells", *J. Appl. Phys.* 101, 093105 (2007)

6. J. A. Jeong and H. K. Kim, "Low resistance and highly transparent ITO-Ag-ITO multilayer electrode using surface Plasmon resonance of Ag layer for bulk-heterojunction organic solar cells", *Soler Energy Materials and Solar Cells* 93, 1801 (2009)

7. Z. Li and L. Lin, "Photonic band structures solved by a plane-wave-based transfer matrix method", *Phys. Rev. E* 67, 046607 (2003)

8. Z. Y. Li and K. M. Ho, "Light propagation in semi-infinite photonic crystals and related waveguide structures", *Phys. Rev. B* 68, 155101 (2003)

9. M. Li, Z. Li, K. Ho, J. Cao and M. Miyawaki, "High-efficiency calculations for three-dimensional photonic crystal cavities", *Opt. Lett.* 31, 262 (2006)

10. M. Reyes, K. Kim, and D. L. Carroll, "High-efficiency photovoltaic devices based on annealed poly(3-hexylthiophene) and 1-(3-methoxycarbonyl)-propyl-1-phenyl-(6,6) C_{61} blends", *Appl. Phys. Lett.* 87, 083506 (2005).

11. H. Hoppe, N. Arnold, N. S. Sariciftci, D. Meissner, "Modeling the optical absorption within conjugated polymer/fullerene-based buld-heterojunction organic solar cells", *Solar Energy Materials & Solar Cells* 80, 105 (2003).

12. L. Martin-Moreno, F. J. Garcia-Vidal, H. J. Lezec, K. M. Pellerin, T. Thio, J. B. Pendry, and T. W. Ebbesen, "Theory of extraordinary optical transmission through subwavelength hold arrays", *Phys. Rev. Lett.* 86, 1114 (2001).

13. P. Kuang, J. M. Park, W. Leung, R. C. Mahadevapuram, K. S. Nalwa, T. G. Kim, S. Chaudhary, K. M. Ho, and K. Constant, "A new architecture for transparent electrodes: Relieving the trade-off between electrical conductivity and optical transmittance", *Advanced Materials*, accepted.

Chapter 7. Emission of organic light emitting diodes with metallic gratings

In chapter 5, we investigated the enhancement in the emission of OLEDs in the forward direction using a microlens array. In chapter 6, we studied the optical absorption in OPV cells in which a metallic grating replaces ITO as transparent electrode, and showed that the grating produces broadband optical absorption enhancement. In this chapter, we will focus on an interesting question: Will the emission of an OLED be enhanced when a metallic grating similar to the one in chapter 6 replaces ITO?

7.1   Numerical method

Since the OLED with metallic grating is basically a periodic structure, the plane-wave based transfer (scattering) matrix method (TMM) can be used for numerical modeling. However, the TMM algorithm we presented in chapter 2 is only applicable for passive devices. To deal with active devices like OLEDs, a new TMM algorithm needs to be developed[1,2]. This section addresses the problem of calculating the emission from an oscillating point dipole placed inside the device. We start from the most general form of Maxwell's equations [Eq. (2.1)],

$$
\begin{aligned}
\nabla \times \vec{E} &= -\frac{1}{c}\frac{\partial \vec{B}}{\partial t}, \\
\nabla \times \vec{H} &= \frac{1}{c}\frac{\partial \vec{D}}{\partial t} + \frac{4\pi}{c}\vec{J}, \\
\nabla \cdot \vec{D} &= 4\pi\rho, \\
\nabla \cdot \vec{B} &= 0.
\end{aligned} \tag{7.1}
$$

7.1.1   Description of a point dipole source

We treat the source to be an oscillating point dipole, with harmonic time dependence, at position $(\vec{\rho}_0, z_0)$, $\vec{\rho}_0 = (x_0, y_0)$. We do not consider Purcell effect[3], so the amplitude of the dipole is independent on the local fields. The spatial dependent of the current $\vec{J}$ is,

$$\vec{J} = \frac{c}{4\pi} \vec{J}_0 \delta(\vec{\rho} - \vec{\rho}_0) \delta(z - z_0)$$

$$= \frac{c}{4\pi} \sum_{\vec{k}_0, ij} \vec{J}_{ij}^{\vec{k}_0} e^{i(k_{ij,x}x + k_{ij,y}y)} \delta(z - z_0), \qquad (7.2)$$

$$where \ \vec{J}_{ij}^{\vec{k}_0} = \vec{J}_0 e^{-i(k_{ij,x}x_0 + k_{ij,y}y_0)}.$$

The Bragg wave vector $k_{ij} = (k_{ij,x}, k_{ij,y}) = (k_{0x}, k_{0y}) + i\vec{b}_1 + j\vec{b}_2$, as defined in chapter 2. $\vec{b}_1$ and $\vec{b}_2$ are the reciprocal lattice constants. In the presence of $\vec{J}$, Maxwell's equations can be written in terms of differential equations relating to the transverse components of fields,

$$\frac{\partial}{\partial z} E_x = \frac{1}{-ik_0} \frac{\partial}{\partial x} \left[\frac{1}{\varepsilon(\vec{r})} \left(\frac{\partial H_y}{\partial x} - \frac{\partial H_x}{\partial y} - \frac{4\pi}{c} J_z \right) \right] + ik_0 H_y,$$

$$\frac{\partial}{\partial z} E_y = \frac{1}{-ik_0} \frac{\partial}{\partial y} \left[\frac{1}{\varepsilon(\vec{r})} \left(\frac{\partial H_y}{\partial x} - \frac{\partial H_x}{\partial y} - \frac{4\pi}{c} J_z \right) \right] - ik_0 H_x,$$

$$\frac{\partial}{\partial z} H_x = \frac{1}{ik_0} \frac{\partial}{\partial x} \left(\frac{\partial E_y}{\partial x} - \frac{\partial E_x}{\partial y} \right) - ik_0 \varepsilon(\vec{r}) E_y + \frac{4\pi}{c} J_y, \qquad (7.3)$$

$$\frac{\partial}{\partial z} H_y = \frac{1}{ik_0} \frac{\partial}{\partial y} \left(\frac{\partial E_y}{\partial x} - \frac{\partial E_x}{\partial y} \right) + ik_0 \varepsilon(\vec{r}) E_x - \frac{4\pi}{c} J_x.$$

Note that $\vec{J} = 0$ anywhere $z \neq z_0$, so Eq. (2.3) holds, and we can use the normal TMM algorithm presented in chapter 2. However, at $z = z_0$ we have to take Eq. (7.3) instead of Eq. (2.3) to accommodate the point dipole source. We integrate both sides of Eq. (7.3) from z_0^-

to z_0^+, and get,

$$
\begin{aligned}
E_x \Big|_{z_0^-}^{z_0^+} &= \frac{1}{-ik_0} \frac{\partial}{\partial x} \left[\frac{1}{\varepsilon(\vec{r})} \left(-\int_{z_0^-}^{z_0^+} dz \frac{4\pi}{c} J_z \right) \right], \\
E_y \Big|_{z_0^-}^{z_0^+} &= \frac{1}{-ik_0} \frac{\partial}{\partial y} \left[\frac{1}{\varepsilon(\vec{r})} \left(-\int_{z_0^-}^{z_0^+} dz \frac{4\pi}{c} J_z \right) \right], \\
H_x \Big|_{z_0^-}^{z_0^+} &= \int_{z_0^-}^{z_0^+} dz \frac{4\pi}{c} J_y, \\
H_y \Big|_{z_0^-}^{z_0^+} &= -\int_{z_0^-}^{z_0^+} dz \frac{4\pi}{c} J_x.
\end{aligned}
\tag{7.4}
$$

Substituting Eq. (7.2) into Eq. (7.4), and applying Fourier expansion presented in chapter 2.2, Eq. (7.4) yields,

$$
\begin{aligned}
E_{ij,x} \Big|_{z_0^-}^{z_0^+} &= \frac{k_{ij,x}}{k_0} \sum_{mn} \varepsilon_{i-m,j-n}^{-1} J_{mn,z}^{\bar{k}_0}, \\
E_{ij,y} \Big|_{z_0^-}^{z_0^+} &= \frac{k_{ij,y}}{k_0} \sum_{mn} \varepsilon_{i-m,j-n}^{-1} J_{mn,z}^{\bar{k}_0}, \\
H_{ij,x} \Big|_{z_0^-}^{z_0^+} &= J_{ij,y}^{\bar{k}_0}, \\
H_{ij,y} \Big|_{z_0^-}^{z_0^+} &= -J_{ij,x}^{\bar{k}_0}.
\end{aligned}
\tag{7.5}
$$

Equation (7.5) shows that an oscillating point dipole at (x_0, y_0, z_0) would bring discontinuities for the transverse electromagnetic fields E_x, E_y, H_x, H_y at $z = z_0$. So we need to incorporate the discontinuities in the boundary condition at $z = z_0$. However, for regions $z \neq z_0$, we still apply continuities of the transverse electromagnetic fields as boundary condition to connect different layers, as we did in chapter 2.

7.1.2 Calculation of emission
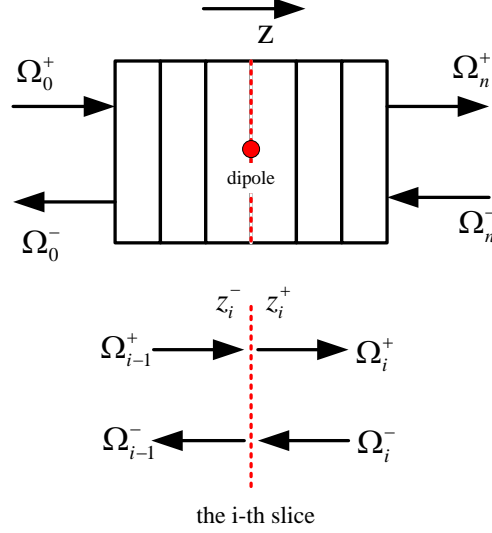
FIGURE 7-1. Schematic view of an active device with a point dipole located at $z = z_i$.

We consider an active device shown in Fig. 7-1 with a point dipole located at the i-th layer ($z = z_i$). From Eq. (7.5) we have,

$$
\begin{pmatrix} E(z_i^+) \\ H(z_i^+) \end{pmatrix} - \begin{pmatrix} E(z_i^-) \\ H(z_i^-) \end{pmatrix} = \begin{pmatrix} P_z \\ P_\parallel \end{pmatrix},
$$

$$
where \; P_z = \left(\frac{k_{ij,x}}{k_0} \sum_{mn} \varepsilon_{i-m,j-n}^{-1} J_{mn,z}^{\bar{k}_0}, \frac{k_{ij,y}}{k_0} \sum_{mn} \varepsilon_{i-m,j-n}^{-1} J_{mn,z}^{\bar{k}_0} \right)^T, \tag{7.6}
$$

$$
P_\parallel = \left(J_{ij,y}^{\bar{k}_0}, -J_{ij,x}^{\bar{k}_0} \right)^T.
$$

In the i-th layer, the electric and magnetic fields can be expressed as [Eq. (2.17)],

$$\begin{pmatrix} E(z) \\ H(z) \end{pmatrix} = \begin{pmatrix} S_i & S_i \\ T_i & -T_i \end{pmatrix} \begin{pmatrix} E_i^+ \\ E_i^- \end{pmatrix},$$

(7.7)

From Eq. (7.6) and (7,7), we have Eq. (7.8). Suppose the scattering matrix to connect the 1st, 2nd,..., and the i -th layer is S^1, and the one to connect the $i+1$ -th, $i+2$ -th, ..., and n -th layer is S^2. Then the relation in $E_i^{\pm}$, $E_0^{\pm}$, and $E_n^{\pm}$ can be expressed in Eq. (7.9) and (7.10).

$$\begin{pmatrix} S_{i+1} & S_{i+1} \\ T_{i+1} & -T_{i+1} \end{pmatrix} \begin{pmatrix} E_{i+1}^+ \\ E_{i+1}^- \end{pmatrix} - \begin{pmatrix} S_i & S_i \\ T_i & -T_i \end{pmatrix} \begin{pmatrix} E_i^+ \\ E_i^- \end{pmatrix} = \begin{pmatrix} P_z \\ P_{\parallel} \end{pmatrix}.$$

(7.8)

$$\begin{pmatrix} E_i^+ \\ E_0^- \end{pmatrix} = \begin{pmatrix} S_{11}^1 & S_{12}^1 \\ S_{21}^1 & S_{22}^1 \end{pmatrix} \begin{pmatrix} E_0^+ \\ E_i^- \end{pmatrix}$$

(7.9)

$$\begin{pmatrix} E_n^+ \\ E_{i+1}^- \end{pmatrix} = \begin{pmatrix} S_{11}^2 & S_{12}^2 \\ S_{21}^2 & S_{22}^2 \end{pmatrix} \begin{pmatrix} E_{i+1}^+ \\ E_n^- \end{pmatrix}$$

(7.10)

Since there is no incident energy, $E_0^+ = 0$ and $E_n^- = 0$. There are 6 unknowns $E_0^-, E_i^{\pm}, E_{i+1}^{\pm}, E_n^+$ in 6 equations (7.8-10). Solving these equations we obtain E_0^- and E_n^+, which represents the emitting field from the device to the negative and positive side, respectively.

$$E_i^- = \left(I - S_{21}^2 S_{12}^1\right)^{-1} \left[\left(S_{21}^2 M_{11} - M_{21}\right) P_z + \left(S_{21}^2 M_{12} - M_{22}\right) P_{\parallel}\right]$$

(7.11a)

$$E_{i+1}^+ = \left(I - S_{12}^1 S_{21}^2\right)^{-1} \left[\left(M_{11} - S_{12}^1 M_{21}\right) P_z + \left(M_{12} - S_{12}^1 M_{22}\right) P_{\parallel}\right]$$

(7.11b)

$$E_i^+ = S_{12}^1 E_i^-, \quad E_0^- = S_{22}^1 E_i^- \tag{7.11c}$$

$$E_n^+ = S_{11}^2 E_{i+1}^+, \quad E_{i+1}^- = S_{21}^2 E_{i+1}^+ \tag{7.11d}$$

$$M \triangleq \begin{pmatrix} \frac{1}{2} S_i^{-1} & \frac{1}{2} T_i^{-1} \\ \frac{1}{2} S_i^{-1} & -\frac{1}{2} T_i^{-1} \end{pmatrix} = \begin{pmatrix} \frac{1}{2} S_{i+1}^{-1} & \frac{1}{2} T_{i+1}^{-1} \\ \frac{1}{2} S_{i+1}^{-1} & -\frac{1}{2} T_{i+1}^{-1} \end{pmatrix} \tag{7.11e}$$

7.2   Emission from OLEDs with metallic gratings

In chapter 3, we present an OLED device with microlens array to enhance the light emission. In chapter 4, we use a metallic grating to replace ITO as transparent electrode to enhance the absorption for OPV cells. It is natural to think: can the metallic grating be transplanted to an OLED to enhance the emission, just like it enhances the absorption in OPV cells?
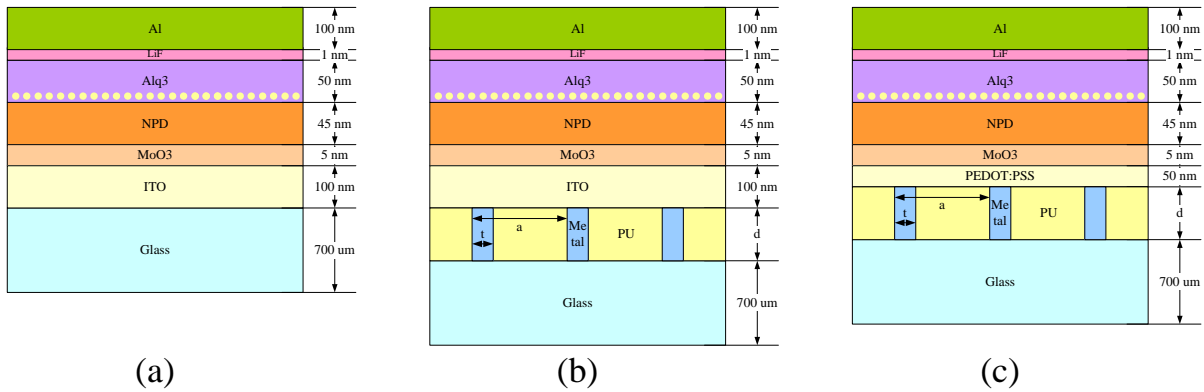

FIGURE 7-2. Schematic view of (a) a regular OLED, (b) an OLED with a metal/PU grating,

(c) an OLED with a metal/PU grating, and PEDOT:PSS in the place of ITO.

We propose a design of OLEDs with metal grating as shown in Fig. 7-2. Shown in Fig. 7-2(a) is a regular OLED with green emitting Alq3 and 100 nm ITO. The emission of this device

will be calculated as a reference. Shown in Figure 7-2(b) is an OLED with a metal/PU grating that is fabricated on glass substrate. We cannot let the grating completely replace ITO like we do in chapter 3, since ITO is needed to keep an effective contact and inject current to OLED. Shown in Figure 7-2(c) is an OLED with a metal/PU grating and a thin PEDOT:PSS film to take the place of ITO. Let d stand for the height of metal/PU grating, a for the periodicity and t for the thickness of metal walls. These are the parameters that can be optimized for an enhanced emission, while the thickness of other parameters is fixed, as shown in the figure.

7.2.1　Emission from OLEDs with metallic gratings and ITO

As the first example, an OLED with silver grating and 100 nm ITO film is studied. The parameters: $a = 1.25 \, \mu m, t = 70 \, nm, d = 300 \, nm$. In our lab metal gratings with similar parameters have been fabricated and studied. In simulation, we assume infinite thick glass substrate to eliminate possible interference pattern in emission spectrum. So the calculated emission is the emission to glass but NOT to air. As investigated in chapter 3, microlens arrays can be applied to enhance the extraction from glass to air. In this chapter, we will focus the effect of the metal grating on the extraction from organic layers to glass only.

We plot the enhancement of emission relative to a regular OLED with 100 nm ITO in Fig. 7-3 (a) for an OLED with a metal/PU grating [as shown in Fig. 7-2(b)], and (b) for an OLED with a metal/PU grating, and PEDOT:PSS in the place of ITO [as shown in Fig. 7-2(c)]. We test 3 metals: gold (blue line with square marks), silver (red circle) and aluminum (green triangle). Although the green light ranges from 490 to 560 nm, we extend the wavelength range to 400~800 nm to have a big picture of the emission spectrum.
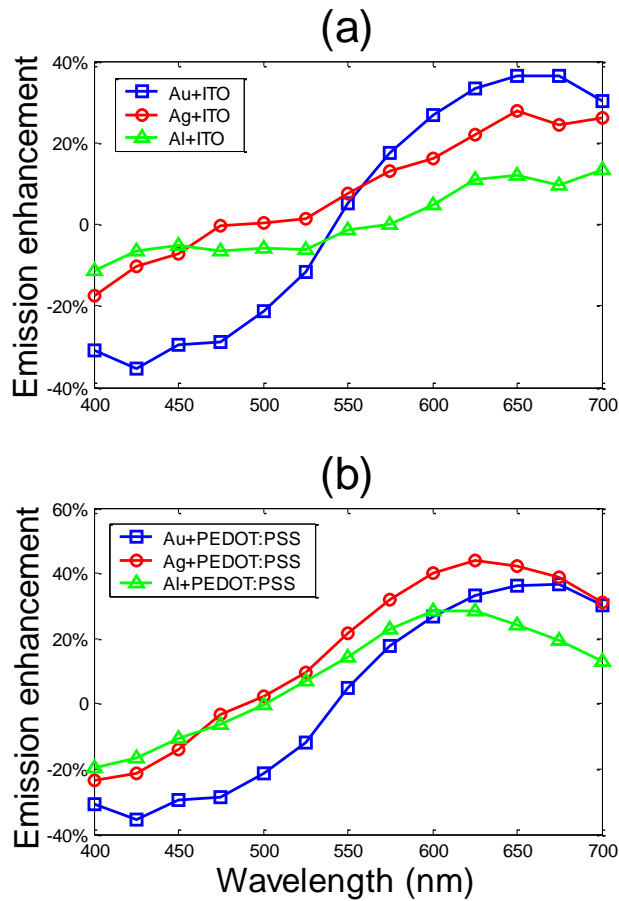
FIGURE 7-3. Emission enhancement relative to a regular OLED with 100 nm ITO for an OLED with (a) a metal/PU grating and ITO (b) a metal/PU grating and PEDOT:PSS.

As indicated in Fig. 7-3, silver grating seems to have a best overall performance. However, the emission has the largest enhancement ~40% at ~625 nm, while the Alq3 based OLED has an emission spectrum which peaks at ~525 nm. No significant enhancement is observed at that wavelength. At short wavelengths <500 nm, there is a reduction in emission for metal grating based OLED.

7.2.2   Effects of grating parameters

There are 3 grating parameters: the period or pitch a, the thickness of metal wall t, and the height of grating d. In the last section, the emission spectrum is calculated with a specific combination of a, t, d. In this section, it is to be investigated how each parameter effect the light emission. So we will aim the wavelength at $525\,nm$ (the emission peak of the green Alq3 based OLED) and only consider silver grating, change one parameter while keeping other two fixed, and observe how the emission changes. In addition, in this section we only consider OLEDs with silver/PU grating + 50 nm PEDOT:PSS as shown in Fig. 7-2(c).

7.2.2.1 Effect of period a

The emission is computed in dependence on a. The height of silver grating is set to be $d = 300\,nm$. Instead of fixing the thickness t of silver walls, we fix the ratio $t/a = 0.056$. The reason is that with the filling ratio of silver t/a fixed, the effect of silver thickness t relative to a is eliminated, and the pure dependence of emission on a can be studied.
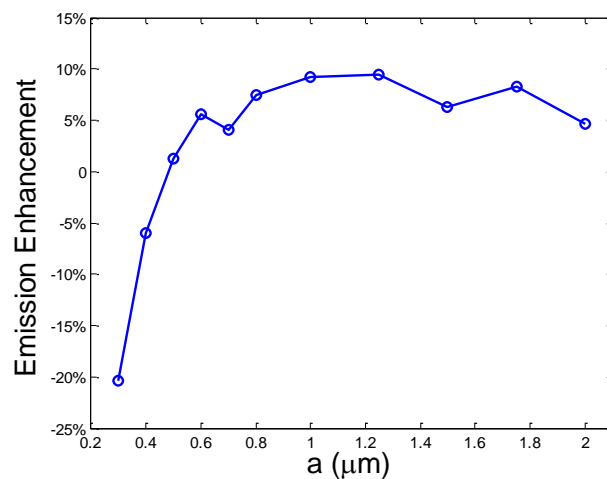

FIGURE 7-4. Dependence of emission enhancement on the period a.

The dependence on a of emission enhancement relative to a 100 nm ITO coated OLED is plotted in Fig. 7-4. The emission is suppressed for small a. The possible reason is, as a is small, the PU channel between two silver walls is too narrow to allow light go through. As a is big enough, the emission does not show substantial dependence on a. The largest emission enhancement is ~10%. No significant enhancement is observed.

7.2.2.2 Effect of thickness t of silver walls

We calculate the emission in dependence on t with period a and height d fixed: $a = 1 \, \mu m, d = 300 \, nm$. The dependence of emission enhancement on t is plotted in Fig. 7-5. As seen in the figure, the emission is not sensitive on t. Although there is enhancement compared to OLED without silver grating, the enhancement is not significant ($<10\%$).
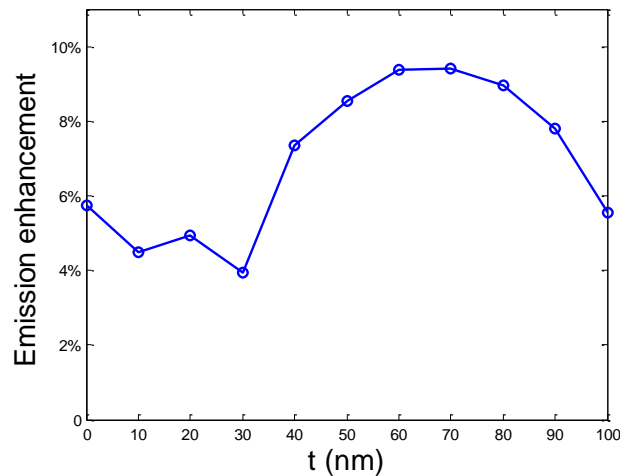

FIGURE 7-5. Dependence of emission enhancement on the silver thickness t.

7.2.2.3 Effect of height d of silver grating

We calculate the emission in dependence on height d of silver grating with period a and

thickness t fixed: $a = 1\,\mu m, t = 60\,nm$. The dependence of emission enhancement on d is plotted in Fig. 7-6. As seen, as d increases from 0 to $0.1\,\mu m$, the enhancement reaches the maximum 15%, because of the scattering by the grating. Then as d keeps on increasing, the enhancement decreases, since higher aspect ratio silver grating will absorb more light.
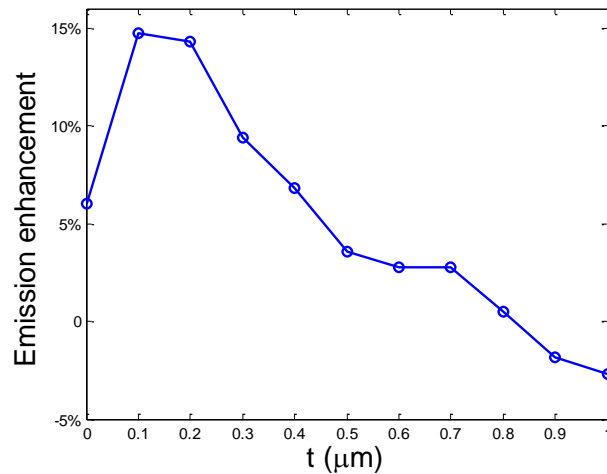

FIGURE 7-6. Dependence of emission enhancement on the silver grating height d.

After investigation of a, t, d's effect on OLED emission, we find there is no indication of significant emission enhancement at $525\,nm$. Since the emission does not seem to be sensitive to anyone of a, t, d, we expect that it is hard to find resonant modes like the ones in chapter 4 to enhance the emission. The reason is, unlike chapter 4 where only normal incidence is concerned, here we need to count the emission from the dipole source along all directions. It is easy to find a resonant mode for a specific direction, however, it is hard to find a resonant mode for all directions.

7.3   Summary

In the first part of this chapter, TMM extension to light emitting system is represented in details. The presence of an oscillating point dipole (x_0, y_0, z_0) gives rise to discontinuities for the transverse electromagnetic fields at $z = z_0$. A series of layers are connected by either continuous (for $z \neq z_0$) or discontinuous (for $z = z_0$) boundary conditions.

Then we used TMM to investigate the emission of green OLEDs with metallic gratings. A ~40% enhancement was found at ~625 nm. However, only ~10% enhancement was found at emission peak 525 nm. The emission is not sensitive to the geometric parameters of metal grating at 525 nm. In future we are going to work on other wavelengths, to see if the emission can be enhanced via surface plasma mode.

References:

1. D. M. Whittaker and I. S. Culshaw, "Scatter-matrix treatment of patterned multilayer photonic structures", *Phys. Rev. B* 60, 2610 (1999).

2. H. Rigneault, F. Lemarchand, and A. Sentenac, "Dipole radiation into grating structures", *J. Opt. Soc. Am. A* 17, 1048 (2000).

3. E. M. Purcell, "Spontaneous emission probabilities at radio frequencies", *Phys. Rev.* 69, 681 (1946).

Chapter 8. An example of sequential ray tracing:
solar concentrator design

In this chapter, a sequential ray tracing method is applied to design a solar concentrator. Although the preliminary results were not good and the project was not completed, we decided to put it in the thesis, as a record of what we have done and also as an example of sequential ray tracing method. In future we may have a reaccess to this topic and we hope the design can be improved and completed at that time.

8.1   Introduction

There are several designs of broad wavelength solar concentrators, like the ones using parabolic trough[1], dish stirling, Fresnel reflectors[2]. These systems use lenses or mirrors to focus a large area of sunlight onto a small area. They require direct sunlight, and they must use a tracking system to keep the devices face the sun. A drawback of these devices is that the efficiency would be low if there is no direct sunlight, like in cloudy days.

To overcome this drawback, it is of interest to know if it is possible to design an all-angle concentrator to collect sunlight even if it is scattered to all directions. We proposed the design as shown in Fig. 8-1. The design was inspired by the idea of a fluorescent solar concentrator[3], where fluorophore absorbs the incident sunlight and re-emits photons which are trapped by total internal reflection and directed towards the PV cells. In our proposed design, we want the concentrator collect the incident sunlight from all directions and guide the light to the edge, where PV cells are placed.
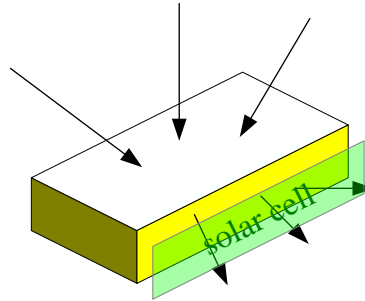
FIGURE 8-1. Schematic view of a solar concentrator.

To realize such a design, we tried a 2-D layout as shown in Fig. 8-2. There are numerous curved funnels to guide the incident light into the device. Then the light is directed in a tapered waveguide on the bottom towards the edge [the shaded area in Fig. 8-2(b)]. A 2nd stage concentrator can be put there to further concentrate the light, like the one in Ref. 1. However, in this chapter we only focused on the 1st stage concentrator. We assumed the walls of funnels and waveguide are made of perfect mirrors to completely reflect light.
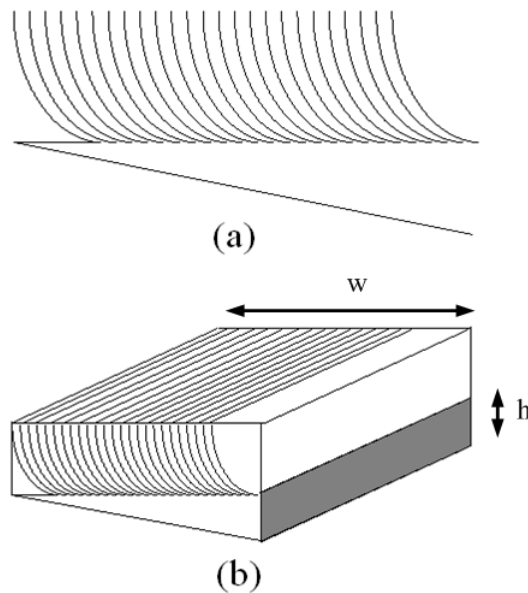

FIGURE 8-2. Construction of a 2-D solar concentrator. (a) side view, (b) 3-D view.

8.2   Sequential ray tracing

In chapter 5 we applied a non-sequential ray tracing method to model OLEDs with microlens arrays. Here we would use a sequential ray tracing approach to simulate the solar concentrator in Fig. 8-2. The word "sequential" means that light travels from surface to surface in a defined order. We used sequential ray tracing since all surfaces are assumed to be perfect reflectors. Once the initial position and direction of a beam are set, the beam undergoes a path that is predefined.
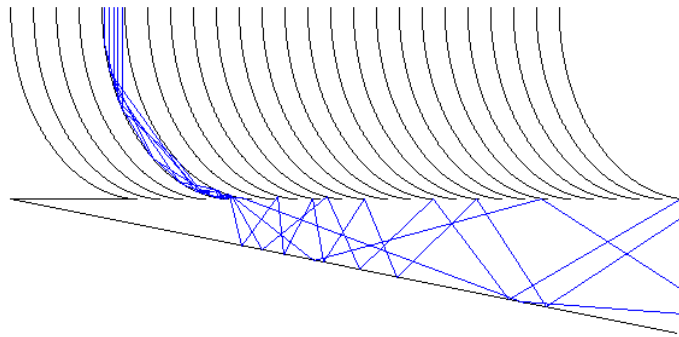

FIGURE 8-3. Diagram of sequential ray tracing.

A diagram of sequential ray tracing method is plotted in Fig. 8-3. Only 5 rays with normal incidence to a funnel are tracked in the figure. In actual simulations, numerous rays from all directions are tracked and numbers of rays that reach the edge are recorded. Then we can calculate the percentage of rays that reach the edge for a specific incident angle.

8.3   Simulation results

In the simulation, we set the initial position of every ray to be at the top of the concentrator (as shown in Fig. 8-3). That is, all rays are already in the concentrator. We do not include the

possible loss when light pass through the interface of air and concentrator. The focus is how well the concentrator performs in leading the light to the edge after light comes in from the air.

We modeled several shapes of mirrors, such as cylindrical, elliptical and parabolic. In Fig. 8-4 we showed the percentage of light that reaches the edge and is to be collected, as a dependence of the incident angle θ. This is for an elliptical mirror based concentrator. The concentration ratio $w/h = 5$, where w, h are the width and height of the concentrator respectively [Fig. 8-2(b)]. For normal incidence $\theta = 0^o$, 90% of light would be collected. However, for $|\theta| > 20^o$ no light would be collected.
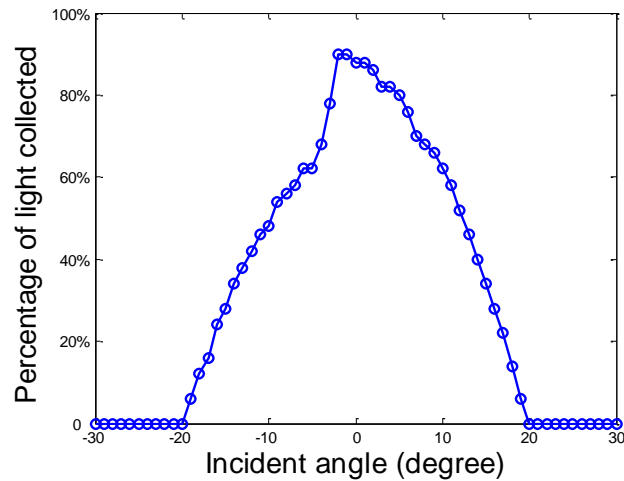

FIGURE 8-4. The percentage of light collected vs the incident angle.

We define the concentration factor as $\eta_1 = \dfrac{collected\ energy}{incident\ energy} \times \dfrac{w}{h}$. Given a specific angular distribution of incident sunlight, η_1 can be calculated via a 3-D integration over solid angles.

We consider an extreme case, where sunlight is completely scattered, and a uniform distribution of incident angle is assumed. In this case $\eta_1 = 1.44$. This means that if we put solar cells at the edge of concentrator, they collect 44% more sunlight than when they are placed horizontally without concentrator.

At first glance, 44% is not a big improvement. However, a 2nd stage concentrator can be placed at the edge of the 1st concentrator to further concentrate light. The function of the 1st concentrator is not only concentrating light, but also orienting light. The exit light is confined to a zone with half angle $\Theta = \dfrac{1}{2}\tan^{-1}\left(\dfrac{h}{w}\right)$. It is $\sim 5.7^o$ for the configuration being studied. Assumed that no loss occur in the 2nd stage concentrator, the energy conservation principle leads to the conclusion that the concentration factor $\eta_2 = \dfrac{1}{\sin\Theta} \sim 10.1$. Several designs, such as compound parabolic concentrators[4] (CPCs) can approach this theoretical limit. If we combine the 2 concentrators, the overall concentration factor would be $\eta = \eta_1 \cdot \eta_2 \sim 14.6$.

8.4 Discussions

In previous simulations, we assumed that all reflectors in the concentrator are perfect ones, i.e. 100% reflectance. However, the reflectance can not be 100% practically. We recalculated η_1 provided 95% and 90% reflectance on average. The results are summarized in Table 8-1. As seen η_1 is dramatically reduced even if the reflectance is cut down from 100% to 90%. The reason is that each ray undergoes multiple reflections in the concentrator before it finally reaches the edge. For example, if a ray experiences 10 reflections given the average reflectance of each one is 90%, its energy would be only $(90\%)^{10} = 35\%$ of its initial

energy.

Table 8-1. The dependence of η_1 on average reflectance of mirrors

Average reflectance of mirrors	100%	95%	90%
η_1	1.44	0.68	0.39

Another factor that should be taken into account is the length of the 2nd stage concentrator. If we want to choose, for example, CPCs as the 2nd concentrator, it should be very long to achieve the theoretical limit. Usually a trade-off must be made to shorten the CPC. In this case η_2 would be less than its theoretical limit.

References:

1. M. Brunotte, A. Goetzberger, U. Blieske, "Two-stage concentrator permitting concentration factors up to 300X with one-axis tracking", *Solar Energy* 56, 285 (1996).
2. D. R. Mills, "Advances in solar thermal electricity technology", *Solar Energy* 76, 19 (2004).
3. W. H. Weber, J. Lambe, "Luminescent greenhouse collector for solar radiation", *Appl. Opt.* 15, 2299 (1976).
4. P. Gleckman, J. O'Gallagher, R. Winston, "Concentration of sunlight to solar-surface levels using non-imaging optics", *Nature* 339, 198 (1989).